



UiT

THE ARCTIC
UNIVERSITY
OF NORWAY

Department of Geosciences

Microstructural changes during melt-assisted modification of quartzofeldspatic rocks

An example from the Eger Complex, North-Western Bohemian Massif

—
Kristine Hafne

Master's thesis in geology – GEO-3900

May 2017



UiT The Arctic University of Norway

Faculty of Science and Technology

Department of Geosciences

GEO-3900

Master thesis in Hard Rock Geology

Microstructural changes during melt-assisted modification of
quartzofeldspatic rocks

Submitted by : Kristine Hafne

First supervisor : Prof. Jiří Konopásek

Co-supervisors : Prof. Petr Jeřábek

Prof. Renée Heilbronner

Prof. Holger Stünitz

Abstract

The Eger Complex is situated in the Saxothuringian domain at the western margin of Bohemian Massif (Czech Republic). Migmatitic orthogneisses associated with granofelses and high-pressure felsic granulites make up the majority of the complex, which is interpreted as an upper crystalline nappe exhumed from underneath the fore-arc Teplá-Barrandian domain during the Variscan orogeny. Studies conducted in the Eger Complex suggested rapid exhumation and cooling after a static heating event from temperatures of $\sim 760^\circ$ estimated for the granofelses to $\sim 850^\circ\text{C}$ estimated for the granulites at isobaric conditions of ~ 16 kbar. The heating event led to substantial modification of microstructure in the granitoid rocks of the Eger Complex and the processes responsible for these changes are the focus of investigation in this work. There is a progressive change from a banded orthogneiss consisting of monomineralic layers of recrystallized K-feldspar, plagioclase and quartz to a macroscopically equigranular microstructure observed in the granulite. Such microstructural change is studied in four samples representing the two end-member microstructures and two intermediate microstructural stages represented by a migmatitic orthogneiss and a granoblastic granofels. Microstructural changes leading to the granulitization have been quantified and described through manual digitization and subsequent statistical analysis of rock microstructures coupled with analysis of crystallographic preferred orientations and both macroscopic and microscopic observations. Grain size analysis of K-feldspar, plagioclase and quartz suggests that the largest change in microstructure occurs at the beginning of anatexis when the strength of the aggregate distribution and the crystallographic preferred orientations are significantly reduced. This change is attributed to melt crystallization. Statistical evaluation of the transition from the migmatitic orthogneiss towards the granofels suggests considerable ripening of the microstructure. In the granulite, the temperature-increase from upper amphibolite to granulite facies resulted in increased melting and subsequent crystallization leading to an almost complete homogenization of the microstructure. Previously estimated melt proportions of $\sim 0-8.5\%$ are considered insufficient to completely rework the originally strongly anisotropic fabric and a model of cyclic melt infiltration is proposed as the most likely mechanism for the destruction of the original rock fabric.

Table of Contents

1	Introduction and aim of thesis	1
1.1	Location of study area	2
1.2	Abbreviations	4
1.3	Geological setting	5
1.3.1	The Saxothuringian domain.....	5
1.3.2	The Teplá-Barrandian domain	6
1.3.3	Central Erzgebirge	6
1.3.4	Eger Complex.....	7
1.4	Previous work in the Eger Complex.....	8
1.5	Sample introduction	9
2	Methods of work	11
2.1	Microscopic area selection.....	11
2.2	Scanning electron microscopy (SEM) imaging	11
2.2.1	Theory behind SEM-imaging	11
2.2.2	SEM-imaging of the studied samples	13
2.3	Redrawing Rock microstructure	14
2.4	Statistical analysis using MATLAB™ and PolyLX toolbox	16
2.5	Crystallographic analysis by electron backscatter diffraction (EBSD)	18
2.5.1	Theory behind EBSD	18
2.5.2	EBSD analysis conditions	19
3	Results	20
3.1	Sample description	20
3.1.1	Type I : Orthogneiss.....	20
3.1.2	Type II : Migmatitic orthogneiss	23
3.1.3	Type III : Granofels.....	26
3.1.4	Type IV : Granulite	28
3.2	Quantitative microstructural analysis	31
3.2.1	Grain maps	31
3.2.2	Grain size	34
3.2.3	Contact frequency	45
3.3	Results of EBSD analysis	48

3.3.1	Biotite	48
3.3.2	Quartz	50
3.3.3	K-feldspar	51
3.3.4	Plagioclase	52
4	Discussion	53
4.1	Interpretation of qualitative observations	53
4.1.1	Solid state deformation	53
4.1.2	Evidence of melting	54
4.1.3	Static recrystallization	54
4.2	Interpretation of quantitative statistical results	55
4.2.1	Interpretation of grain size	55
4.2.2	Interpretation of spatial distribution of phases	57
4.2.3	Interpretation of EBSD-results	59
4.3	Interpretation of chemical changes in minerals	60
4.4	Origin of evolutionary sequence	60
4.5	Evolutionary model	63
5	Conclusions	64
6	Acknowledgements	65
	Works cited	66
	Appendix A	70
	Appendix B	75

List of Tables

Table 3.1-1 Results of microprobe analysis of minerals for type III granofels and type IV granulite ...	30
Table 3.2-1 Table showing the number of digitized grains.....	32
Table 3.2-2 EAD measurements of K-feldspar, plagioclase and quartz	35

List of Figures

Figure 1.1-1 Macroscopic appearance of the Eger Complex metagranatoids.....	2
Figure 1.1-2 Tectonic map of the Bohemian Massif	3
Figure 1.1-3 Simplified geological map of a part of the Erzgebirge	3
Figure 2.1-1 BSE electron-sample interaction.....	12
Figure 2.2-1 QGIS digitizing layer-arrangement.....	15
Figure 2.3-1 Equal diameter as a grain size measurement	17
Figure 3.1-1 Hand sample EC8Y, type I orthogneiss	21
Figure 3.1-2 Details of BSE and photomicrographs for type I orthogneiss.....	23
Figure 3.1-3 Hand sample EZ 22P, type II migmatitic orthogneiss.	24
Figure 3.1-4 Details of BSE and photomicrograph for type II migmatitic orthogneiss.	25
Figure 3.1-5 Hand sample EZ 22R, type III granofels.	26
Figure 3.1-6 Details of-BSE image and photomicrograph for type III granofels.	27
Figure 3.1-7 Hand sample EZ 22S, type IV granulite	28
Figure 3.1-8 Details of BSE-image and photomicrograph for type IV granulite.....	30
Figure 3.2-1 Digitized grain maps.....	33
Figure 3.2-2 Grouped boxplot.....	37
Figure 3.2-3 Grain size distribution for Kfs, plg and qtz	39
Figure 3.2-4 Grain size maps for quartz within the four microstructural types	44
Figure 3.2-5 Model of spatial distribution of phases.	45
Figure 3.2-6 Grain boundary contact frequencies	47
Figure 3.3-1 Biotite CPO data	49
Figure 3.3-2 Quartz CPO data.....	50
Figure 3.3-3 K-feldspar CPO data	51
Figure 3.3-4 Albite CPO data	52

1 Introduction and aim of thesis

Melt formation, its migration and subsequent crystallization in the lower crust has a major effect on rock macro- and microstructures. In extreme cases the melting-related process can lead to complete disintegration of previously developed anisotropy in favour of microstructurally homogenous rocks even at low proportions of partial melting. Disruption and disintegration of such anisotropy have substantial consequences for the mechanical and seismic properties of the lower crust ([Lee et al. \(2017\)](#) and references therein).

The Eger Complex in the western Bohemian Massif represents an exhumed segment of deep seated crustal rocks comprised of high-pressure felsic orthogneisses and granulites along with intermediate rock types exhibiting various microstructures. Continuous transitions from strongly anisotropic orthogneisses through migmatitic orthogneisses to granoblastic granofelses and granulites can be observed on both outcrop and hand specimen scale (Figure 3.1-1). [Konopásek et al. \(2014\)](#) demonstrated that the microstructural changes took place in the presence of small volumes (<10 %) of melt that crystallized K-feldspar, plagioclase and quartz. Considering that there is a complete destruction of the banded fabric, the question is if the modelled melt proportion is sufficient to drive such a drastic change in the microstructure or if there were other processes operating. The sequence of samples collected within the Eger Complex provides a record of an evolutionary path from strongly anisotropic to apparently homogenous microstructure. The rocks of the Eger Complex show signs of partial melting and the study of the sampled sequence could provide important insight into how melting-related processes contribute to the disintegration of previously developed rock fabrics.

In this thesis, a microstructural sequence of four samples from an initially strongly banded orthogneiss, through a migmatitic orthogneiss, a granofels to a macroscopically equigranular granulite was investigated with the aim to document and statistically quantify the microstructural changes. The protolith, a Lower Ordovician granite deformed under high-temperature conditions, is characterized by alternating monomineralic layers of recrystallized K-feldspar, plagioclase, quartz and thin bands of mica which is progressively transformed into a granulite with a homogenous microstructure.

The major phases within the rock volume, K-feldspar, plagioclase and quartz were studied in detail through their microstructural and textural characteristics including grain size, spatial distribution and crystallographic preferred orientation. Based on the results of the mentioned analyses an

evolutionary model is proposed and the possible mechanisms that could account for the origin of the studied sequence of microstructures are discussed.



Figure 1.1-1 Macroscopic appearance of the Eger Complex metagranatoids after [Konopásek et al. \(2014\)](#). The hand specimen exhibits a continuous transition from strongly banded orthogneisses (right side) with alternating layers of quartz, feldspars and mica through a diffusely banded gneiss towards a granoblastic granofels (left side). The compositional banding is cross cut by shear-band containing crystallized melt

1.1 Location of study area

The area of interest in this thesis, the Eger Complex, is a small crystalline complex at the western margin of the Bohemian Massif. The complex emerges as an erosional window in Mesozoic and Cenozoic volcano-sedimentary units in the Eger river valley situated in the lower limits of the Erzgebirge Mountains in northwestern Czech Republic (Figure 1.1-1 and Figure 1.1-2). The samples analysed in this thesis were collected from two locations of exposed crystalline rocks along the Eger River, the first one being Zámecký park in Klasterec nad Ohri (N 50.3841376 E 13.1768775) and the other one being Krvava skála in Kadan (N 50.3731064 E 13.2762747E). Both localities are easily accessible by road as they are both within their respective city limits and the distance between the two localities comes to just over seven kilometres.

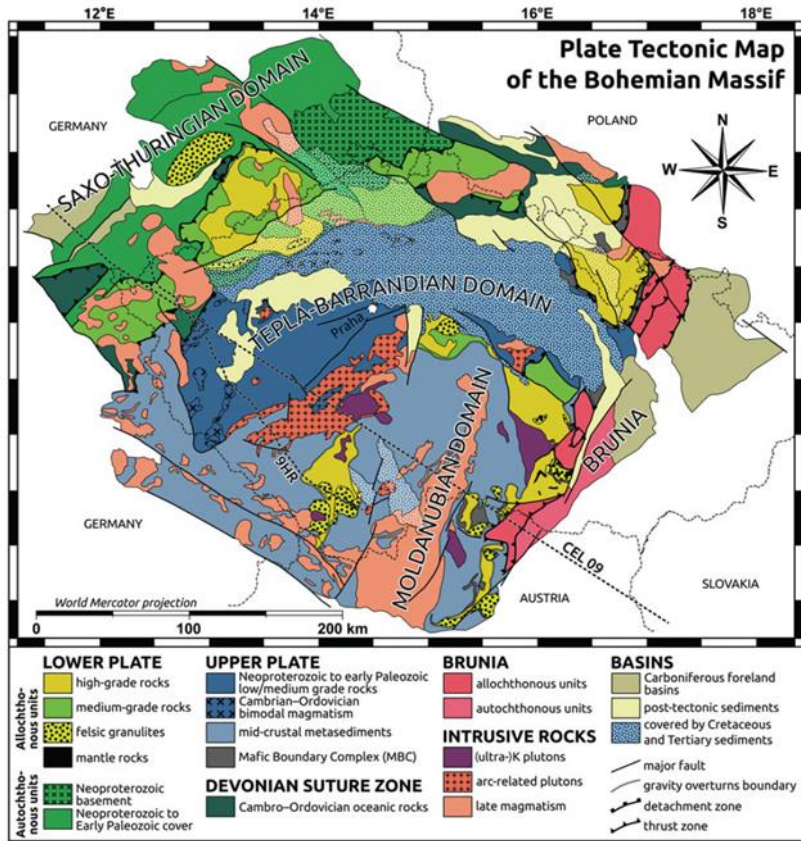


Figure 1.1-1 Tectonic map of the Bohemian Massif after Schulmann et al. (2014) illustrating how the massif is divided in four principal domains, Saxothuringian domain, Teplá-Barrandian domain, Moldanubian domain and the Brunia domain. The Saxothuringian and parts of the Moldanubian domain belong to the lower plate and the rest belongs to the upper plate of the Variscan Orogen in Central Europe.

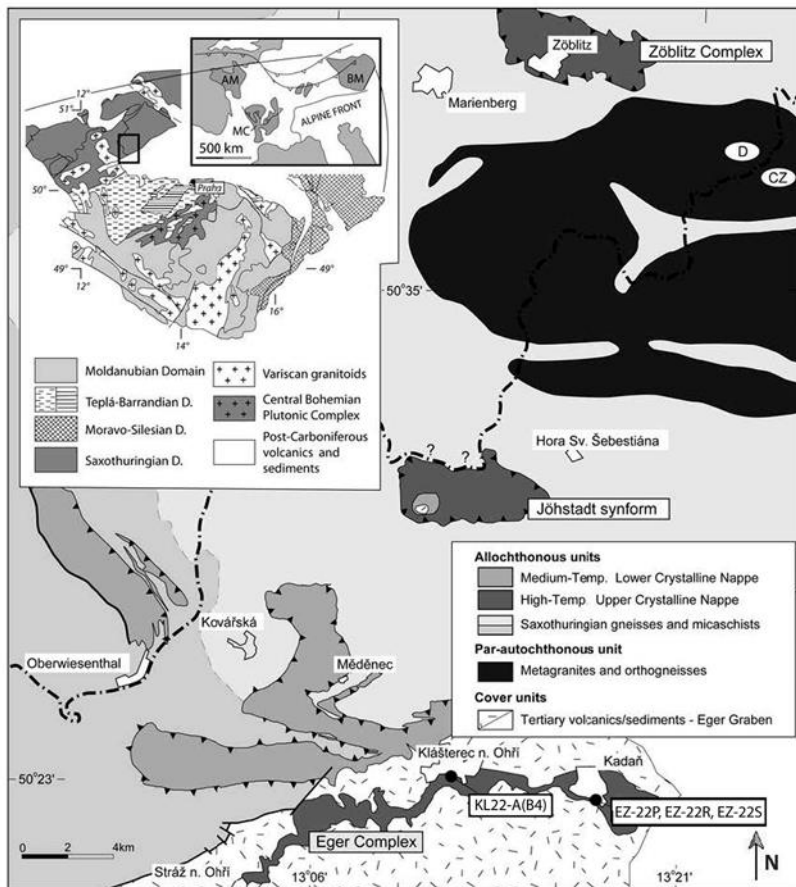


Figure 1.1-2 Simplified geological map of a part of the Erzgebirge that includes the Eger Complex after Konopasek and Schulmann (2005). Sample locations are shown by black dots. The upper left inset shows the geometry of massifs within the European Variscides (BM, Bohemian Massif; MC, French Massif Central; AM, Armorican Massif). Also in the upper left corner, a simplified map of the Bohemian Massif, where a black rectangle marks the location of the main part of the figure.

1.2 Abbreviations

Minerals

Ap	apatite
Bt	biotite
Grt	garnet
Ilm	ilmenite
Kfs	K-feldspar
Ky	kyanite
Plg	plagioclase
Mu	muscovite
Opq	opaque
Qtz	quartz
Ru	rutile

Other

λ	wave-length
BSE	backscattered electrons
CL	Cathodoluminescence
CPO	crystallographic preferred orientation
EAD	equal area diameter
EBS	electron backscatter diffraction
EDX/EDS	energy dispersive X-ray spectroscopy
kV	Kilovolt
Ma	million years ago
MUD	multiple of uniform distribution
Myr	million years
UHP	ultra-high pressure
UHT	ultra-high temperature
VPSE	variable pressure secondary electron
XPL	cross polarized light

1.3 Geological setting

The Bohemian Massif is one of the largest exposures of pre-Permian rocks in Western Europe and it records a complex evolutionary history involving both the Cadomian orogeny in the Neoproterozoic and the extensive Variscan orogeny in the late Paleozoic ([Matte et al., 1990](#)). Based on differences in structure and geological evolution, the massif can be divided into four litho-tectonic domains. From West to East these domains are the Saxothuringian domain, the Teplá-Barrandian domain, the Moldanubian domain and the Brunia domain (**Figure 1.1-1** and **Figure 1.1-2**), together these four tectonic domains represent a complete section through a typical collisional orogeny ([Schulmann et al., 2009](#)). As the Variscan orogeny commenced in Early Devonian, the Saxothuringian domain acted as a northwestern colliding block, and now it shows abundant evidence for subduction-related metamorphism. The Teplá-Barrandian domain is representative for a fore-arc region of the overriding plate. The Moldanubian domain itself represents a back-arc domain showing evidence for crustal thinning, severe deformation and high metamorphic grade ([Schulmann et al., 2009](#)). The contact zone between the Moldanubian and Teplá-Barrandian domains is characterized by calc-alkaline intrusions and has been interpreted as a magmatic arc. Lastly, the Brunia domain acted as a rigid back-stop in the east, showing only few signs of crustal reworking.

1.3.1 The Saxothuringian domain

The Saxothuringian domain represents the northeastern boundary of the Bohemian Massif and is characterized by Cambrian to Carboniferous volcano-sedimentary rocks with greenschist or lower metamorphic grade with areas reaching amphibolite facies within deeply eroded parts of the zone. The Saxothuringian domain exhibits variable early Carboniferous (Variscan) overprint and the volcano-sedimentary sequences are cut by late- to post-collisional granites ([O'Brien and Carswell, 1993](#), [Franke, 2000](#), [Kroner, 2007](#)). The Cadomian basement-sequences developed along an active margin on the northern periphery of the Gondwana continent between 570 Ma and 540 Ma ([Nance and Murphy, 1994](#), [Linnemann et al., 2004](#)). The evolution that followed has been linked to the rifting of the Saxothuringian domains from the Gondwana margin, an event which was accompanied by intrusions of acidic volcanic- and plutonic rocks and development of thick sedimentary sequences ([Linnemann et al., 2000](#)). Late Ordovician to Devonian deep-sea sediments suggest the establishment of a passive margin and the opening of an oceanic domain termed the Saxothuringian Ocean. Plate motions changed in the Early Devonian, leading to the closure of the Saxothuringian ocean through subduction (400-355 Ma) ([Schulmann et al., 2009](#)). In early Carboniferous, the subduction culminated in a collisional orogeny where the Saxothuringian domain was thrust under the

overriding Teplá-Barrandian plate (at ca. 340 Ma). The underthrusting resulted in deformation and metamorphism with increasing intensity toward the contact with the Teplá-Barrandian domain to the southeast. In the eastern parts of the Saxothuringian domain, the underthrusting led to eclogitization of both oceanic and continental crust ([Konopasek and Schulmann, 2005](#)). In the central part of the exposed eastern Saxothuringian domain, the early subduction along with continental underthrusting is responsible for high pressure metamorphism reaching the stability field of diamond ([Kotkova et al., 2011](#)). The high-pressure rocks reached their upper crustal position through a major period of exhumation in the Early Carboniferous within the subduction channel along the Saxothuringian-Teplá-Barrandian suture.

Today, the rock-assemblage exhumed from the subduction zone is represented by high-pressure metasediments and orthogneisses with numerous exposures of mafic eclogites. One of these units, interpreted as a segment of the lower continental crust originating in (or exhumed from) the deep fore-arc region is the high-pressure/high-temperature Eger Complex, which is the subject study in this thesis.

1.3.2 The Teplá-Barrandian domain

The Teplá-Barrandian domain constitutes the fore-arc domain of the Bohemian Massif and is the best preserved fragment of Cadomian basement in central Europe ([Franke, 2000](#)). The domain represents a supracrustal complex that comprises deformed Neoproterozoic basement and Late Cambrian to Devonian volcanic and sedimentary rocks ([Franke, 2000](#), [Schulmann et al., 2009](#)). The Teplá-Barrandian domain has only a weak Variscan overprint, and was not subjected to Carboniferous high-temperature/low -pressure metamorphism as the adjacent Saxothuringian and Moldanubian domains.

1.3.3 Central Erzgebirge

The Erzgebirge (meaning the Ore Mountains) is a high-grade metamorphic complex situated on the border between Germany and the Czech Republic. In geological terms, the Erzgebirge forms part of the Saxothuringian domain where it constitutes a large NE-SW trending antiform built up of nappes originating from exhumation from the root of the overthickened Teplá-Barrandian crust during the Variscan collisional event ([Mingram et al., 2004](#), [Konopásek et al., 2014](#)). At its core, the Erzgebirge consist of a nappe or nappes of medium to ultra-high pressure para- and orthogneisses and mica schists with eclogite and peridotite lenses, surrounded and partly overlain by phyllites and intruded by late- to post- collisional granites. ([Mingram, 1998](#), [Roetzler et al., 1998](#), [Mingram et al., 2004](#),

[Perchuk, 2008](#)). To the NE the Erzgebirge is bounded by the long lived strike-slip Elbe fault zone whereas the SE limit is defined by the Cenozoic Eger graben, characterized by Cenozoic sedimentary infill and basaltic flows ([Štemprok and Blecha, 2015](#)).

In the central part of the Erzgebirge, three tectonometamorphic units can be recognized through their surface exposure (Figure 1.1-2). (1) The large orthogneiss body of the Sv.Katerina – Reitzenhein structure and overlying metasediments are together regarded as the lowermost parautochthonous tectonic unit ([Mlčoch and Konopásek, 2010](#)). (2) The parautochthonous domain is partly overlain by an allochthonous Lower Crystalline Nappe comprised of medium temperature orthogneisses with associated eclogites. The Lower Crystalline Nappe within Central Erzgebirge is mainly exposed in synforms and antiforms, including Oberweisenthal synform, Medenec synform and antiform as well as the Klinovec structure. (3) In a number of places the metasediments of the parautochthonous unit are covered by an allochthonous Upper Crystalline Nappe of high-temperature migmatitic orthogneisses associated with granulitic gneisses and high-pressure granulites. The Upper Crystalline nappe is exposed in the Jöhstadt synform, the Zobnitz complex and the Eger crystalline complex. (For detailed overview of the tectonometamorphic units within the Central Erzgebirge see [Konopasek and Schulmann \(2005\)](#) and references therein).

1.3.4 Eger Complex

The Eger Complex is a high-grade crystalline complex exposed in an erosive window from Cenozoic volcanics at the foot of the Erzgebirge mountains ([Konopásek et al., 2014](#)). The complex forms the uppermost thrust sheet of a more extensive crustal nappe stack (Upper Crystalline Nappe) which is interpreted as having been exhumed from underneath the Teplá-Barrandian domain ([Konopasek and Schulmann, 2005](#)). The majority of the Eger Complex is built up of orthogneisses and felsic granulites. Field observations suggest that the felsic granulites form isolated outcrops surrounded by orthogneisses and granofelses with upper amphibolite-facies mineral assemblages ([Konopásek et al., 2014](#)). Transitions from strongly banded orthogneiss to granofels lacking any apparent macroscopic foliation can be observed both on outcrop scale and in hand specimens (Figure 1.1-1).

Thermodynamic modelling suggests that the peak metamorphic conditions were ~700°C and 9 kbar for partially molten orthogneisses, ~760°C and ~16 kbar for the granofelses and ~850°C and ~16 kbar for the granulites. Additionally, thermodynamic modelling indicates that the rocks equilibrated in the presence a small fraction of melt amounting to ~4 wt % in the orthogneisses and ~5.5 to 8.5 wt% in the granulites ([Závada et al., 2007](#), [Konopásek et al., 2014](#)). Studies of the orthogneisses and granulites within the Eger Complex, suggest that that peak metamorphism occurred at c. 340 Ma and

that the static heating of the complex led to a partial granulitization of the which terminated due to rapid exhumation and cooling ([Kotková et al., 1996](#), [Zulauf et al., 2002](#), [Konopásek et al., 2014](#)).

1.4 Previous work in the Eger Complex

The Eger Complex has been a target of several studies the last thirty years and the most important findings of these studies are summarized within this chapter.

[Kotková et al. \(1996\)](#) analysed zircons and rutile from a granulite within the Eger Complex along with two granulite samples from deep boreholes in the Central Bohemian Uplands, SE of the exposed Eger complex. As a result of the analysis, a mean $^{207}\text{Pb}/^{206}\text{Pb}$ age of 342 ± 5 Ma was adopted to reflect the timing of peak HP metamorphism. The authors also used the slightly lower $^{207}\text{Pb}/^{206}\text{Pb}$ age of rutile, attributed to a much lower closing temperature for the U-Pb isotopic system compared to zircon, as well as the data previously published [Kotková \(1993\)](#) to support the conclusions of [Kotková \(1992\)](#) and [Kotková \(1993\)](#) that the peak metamorphism of the Eger granulites was followed by relatively rapid uplift. The $^{207}\text{Pb}/^{206}\text{Pb}$ ages were in excellent agreement with zircon ages for granulites in Saxony and southern Bohemia, implying an extensive regional granulite metamorphism at 340 Ma ([Kotková et al., 1996](#)).

[Zulauf et al. \(2002\)](#) carried out detailed structural and kinematic investigations along with U-Pb dating of monazite and ^{40}Ar - ^{39}Ar dating of micas in orthogneisses and granulites of the Eger Complex. The results of their structural investigations suggested that dislocation creep and volume diffusion operated simultaneously during deformation of the Eger Complex rocks. They estimated a rapid cooling ($50 \pm 25/-17$ °C Myr $^{-1}$) and exhumation rate (1.2-2.5 mm Myr $^{-1}$) based on U-Pb ages of monazite (342 ± 1 Ma) representing the peak age of metamorphism and ^{40}Ar - ^{39}Ar dating of muscovite (341 ± 1 Ma) representing the timing of exhumation and cooling of the Eger Complex orthogneisses. The rapid exhumation and cooling was attributed to a fast “elevator-style” movements in combination with the contact between the hot lower crustal rocks of the Eger Complex and the relatively cold crust of the Teplá-Barrandian domain.

[Závada et al. \(2007\)](#) described the evolution of banded low- to high-strain orthogneisses of the Eger Complex in detail through microstructural analysis and CPO of quartz and feldspars. The authors documented the evolutionary impact of partial melting on the rock rheology and evolution of rock microstructure. With the help of thermodynamic modelling, they found that the orthogneiss contained ~2-4 vol % melt at its metamorphic peak.

[Kotkova et al. \(2011\)](#) compared granulite samples from the Eger Complex with granulite samples from drill-cores from the Central Bohemian Uplands and found diamond and coesite in garnet, kyanite and zircon documenting UHP conditions of $P > 40$ kbar for presence of diamond and $P > 30$ kbar for presence of coesite ([Kotkova et al., 2011](#)).

[Konopásek et al. \(2014\)](#) studied redistribution of zirconium along minerals in orthogneisses, granofelses and granulites in the Eger Complex by focusing on CL-investigations, U-Pb dating and mass balance calculation, as well as thermodynamic modelling of P-T conditions of the different rock types. Their thermodynamic modelling suggested a short-lived static heating event from ~ 760 to ~ 850 °C at ~ 16 kbar. While CL-imaging and U-Pb dating of zircon cores yielded a protolith age of 475-470 Ma, the dating of zircon rims confirmed the previously published age (340 Ma) for granulite-facies metamorphism by [Kotková et al. \(1996\)](#). From zircon redistribution calculations they concluded that the formation of zircon rims results from solid-state recrystallization rather than new crystallization of zircon. The study ultimately concludes that a short-lived static event exposing the metagranitoids of the Eger Complex to a temperatures of ~ 850 °C at the base of an arc/fore-arc region led to a partial granulitization of the rocks that terminated due to rapid exhumation and cooling.

[Haifler and Kotková \(2016\)](#) studied samples of garnet-clinopyroxene rocks by performing a petrographic study, bulk rock analysis, chemical analysis and Ti-in-zircon thermometry from which they reconstructed the metamorphic evolution. They found that the garnet-clinopyroxene rocks in the Eger Complex underwent UHP-UHT metamorphism experiencing temperatures within the diamond stability field (c. 1100 °C) at 50 kbar.

1.5 Sample introduction

Four rock samples believed to represent a microstructural sequence have been the focus of investigation in this thesis. The microstructural sequence includes a strongly banded granitic orthogneiss with a completely recrystallized fabric, a migmatitic orthogneiss showing evidence of partial melting and crystallization, a granofels approaching a complete granoblastic microstructure and a well-equilibrated felsic granulite. Based on microstructural appearance, the studied rocks have been divided into four microstructural stages, where type I microstructure is represented by an orthogneiss sample characterized by monomineralic aggregates of K-feldspar, plagioclase and quartz discretely separated by mica-rich domains. Type II microstructure corresponds to a migmatitic orthogneiss where K-feldspar, plagioclase and quartz aggregates contain interstitial grains of the

other phases (i.e quartz aggregates contains interstitial K-feldspar and plagioclase grains etc.). Type III microstructure is represented by a granofels lacking an apparent foliation and where domains enriched in K-feldspar, plagioclase and quartz are barely recognisable. Type IV microstructure is recognized in the granulite where the phases are largely intermixed and no foliation is visible. Detailed descriptions of these microstructural stages are presented in section 3.1.

2 Methods of work

2.1 Microscopic area selection

To draw decent conclusions from any quantitative data analysis, it is important that the analysis is performed on a valid dataset. In the case of this thesis, this entails redrawing a representative cross-sectional area of samples that range from strongly anisotropic to granoblastic textures. Due to the compositional banding exhibited by the two orthogneiss samples (type I and type II microstructures) it would simply take an extensive amount of digitizing, likely spreading over several thin-sections to achieve completely representative data for these two sections. As this would be an impossible task to complete within the time constraints set for this work, digitizing areas for the two samples in question was chosen based on which areas within the thin sections would yield the most representative results.

For the granofels and granulite (type III and type IV microstructures), the general distribution of grains is more homogenous which increases the likelihood that any randomly chosen area would be close to representative for the whole sample. Still, digitizing areas for these samples were also carefully chosen so that a representative cross sectional area for each microstructural type would be redrawn.

2.2 Scanning electron microscopy (SEM) imaging

Today, SEM-imaging is one of the most widely used instruments for direct studies of solid sample surfaces. Easy sample preparation, high-resolution imaging which is directly interpretable in terms of chemical and microstructural properties along with the possibility of using multiple detectors to obtain complementary information are the biggest draws for using SEM-imaging.

2.2.1 Theory behind SEM-imaging

A scanning electron microscope (SEM) usually operates in vacuum and images the sample by raster-scanning the surface with a focused beam of high-energy incident electrons ([Dehm et al., 2012](#)). The electrons emitted from the electron gun carry a large amount of kinetic energy that dissipates as the incident electrons decelerate due to their interaction with the solid sample. Energy dissipated from this interaction takes on a variety of forms, including characteristic X-rays, backscattered electrons (BSE), secondary electrons (SE), visible light (cathodoluminescence) etc. These various emitted

signals are picked up by detectors and subsequently processed to create a grey-scale image where the intensity of the signal is presented by variable brightness.

Back scattered electrons (BSE)

BSE are generally defined as high-energy electrons that result from elastic collisions of the incident electrons with the solid sample, rather than inelastic collisions. Material with high average atomic numbers (\bar{Z}) produces greater elastic scattering compared to material consisting of smaller atoms with lower \bar{Z} , this effect is shown in Figure 2.2-1 and is due to the larger cross-sectional area of heavier atoms (Brandon et al., 2008, Marassi and Nobili, 2009). Consequently, the intensity of signal reaching the BSE-detector is proportional to the average atomic number of the sample volume, meaning that the grey-levels in the BSE output-image directly correlates to \bar{Z} of the sampled material. In Earth sciences, this easy separation of material based on composition is especially useful when investigating mineral phase distributions within a sample.

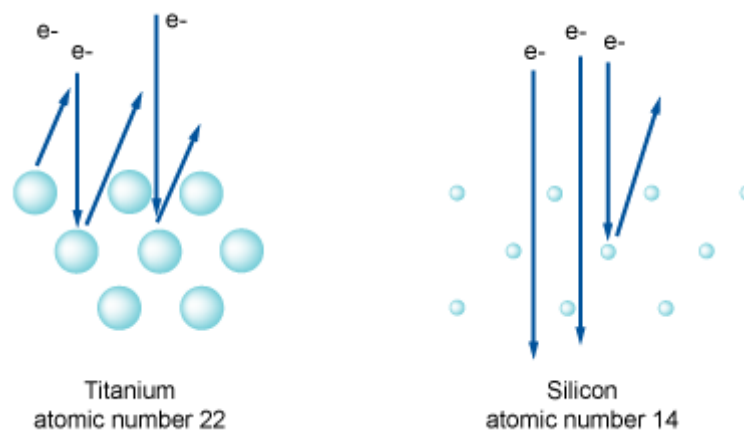


Figure 2.2-1 BSE electron-sample interaction. The figure illustrates how incident electrons and interact with samples of Titanium, representing material with larger Z , and Silicon, representing material with lower Z after [Australian Microscopy & Microanalysis Research Facility \(2014\)](#).

Cathodoluminescence (CL)

Cathodoluminescence is the emission of photons induced in a sample subjected to bombardment of electrons. Electron-bombardment of samples causes electrons in specific chemical impurities to be excited to a higher energy-state, and when electrons return to their original ground-state the energy difference is released as photons. Intensity of the CL-signal depends various complex factors, where mineral conductivity, nature and occurrence of crystal defects are the most significant. Similar to

BSE-imaging, this allows interpretation of the brightness of the resulting grey-scale image as a function of chemical properties of minerals, but in addition, CL-imaging can reveal mineral zoning, growth- and dissolution features as well as deformation features.

Energy dispersive X-ray spectroscopy (EDS)

EDS is a chemical analysis tool used in combination with SEM in order to detect specific elemental composition of solid material. EDS detectors makes use of X-rays that are emitted from the sample when it interacts with a high-energy electron beam. The highly energized electron beam has the potential to knock electrons from the inner shells of the atoms within the sample out of their orbit, the resulting vacancies are quickly filled by electrons of a higher energy state. As the higher energy electron falls down to fill the vacancy, an X-ray photon with sharply defined frequencies is released to balance the energy difference between the two electron states. Since each element has unique set of energy levels for their shells, each element will emit an X-ray pattern that is characteristic for that element. In this way, we can use EDS to map the surface of a sample in terms of its elemental composition. In the resulting map, the intensity or brightness will reveal the relative proportions of elements within the scanned area. EDS is also commonly used to determine mineral chemistry in terms of point analysis and to reveal compositional variations through line scans.

2.2.2 SEM-imaging of the studied samples

Prior to the SEM-imaging, all samples were carbon-coated to help charge dissipation of the non-conductive samples. The main part of the SEM-imaging was carried out at the Faculty of Health Sciences of UiT the Arctic University of Norway using a Zeiss Merlin VP Compact equipped with various detectors. Because of a lengthy EDS malfunction at the Faculty of Health Sciences, a Hitachi TM3030 Tabletop Microscope located in the main laboratory at the Department of Geosciences was used as a substitute for analysis of type I orthogneiss.

Back scattered electrons

Since BSE gives information based upon average atomic numbers (\bar{Z}) of the scanned compounds, it would not be able to adequately distinguish phases that have similar \bar{Z} values, such as plagioclase and quartz. Based on the fact that BSE-imaging clearly distinguishes muscovite and biotite, which both appear black in CL-images, it was chosen to do BSE imaging of the two samples exhibiting well-defined mica bands. The BSE imaging was carried out using an accelerating voltage of 20 kV, 100x magnification and a working distance of 8.2-8.7 mm.

Cathodoluminescence

As there is only a little contrast between plagioclase and quartz in BSE images, CL-imaging of the samples was chosen as it clearly shows grain boundaries for most minerals within the sample. In addition, it provides information complementary to EDS and BSE. CL-images were produced by the use of a variable pressure secondary electron (VPSE) detector in vacuum. A VPSE detector is designed to work in a gaseous environment. The detector picks up photons emitted from gas-molecules as they are hit by secondary electrons emitted from the sample when the sample itself interacts with the incident electron beam. Removing the gaseous environment results in the VPSE detector operating as a CL detector. The CL-imaging was carried out with an accelerating voltage of 15 kV, 100x magnification and a working distance within the range of 7.8 to 8.4 mm.

Energy dispersive X-ray spectroscopy and mineral chemistry

EDS gives essential information about sample chemistry, which allows for relatively easy phase identifications when used in combination with the light microscope. An 18-20 hour long automated analysis was set up for each of the predefined areas, keeping the step-size as small as the given time frame would allow. As it is not possible to configure automated analysis with the table top microscope, single frame analysis was used for the type I orthogneiss. The single frame analysis was mainly used in areas where clear phase identifications could not be accomplished from previously acquired data.

Mineral chemistries were measured for the granofels and granulite with an electron probe micro-analyser with field emission gun (FEG) electron source JXA-8530F by Jeol. The analysis took place in the facilities of Charles University Faculty of Science.

2.3 Redrawing Rock microstructure

SEM images and maps that were obtained for each sample during the preliminary work of the thesis were arranged in layers and subsequently digitized using the open-source geographic information system QGIS. The layers are actually a collage of images that were stitched together using a flat-scanned method, involving only resizing and repositioning in the panorama photo-sticher program, Hugin. The layers were arranged in QGIS with the CL and BSE (if they were taken), images at the base, serving as the primary source of information as they portray the grain boundaries of the sample surface most accurately. As the CL signal depends on several factors including crystal defects two distinct layers of photomicrographs were added in order to corroborate the information from CL

images. On top of the CL and BSE base layers EDS maps were mainly used to identify phases, while photomicrograph-layers taken in XPL and XPL + λ (XPL with the retardation plate inserted) images were used as an additional source of information. To ensure that the redrawing of grain boundaries and phase identification was as accurate as possible the polarizing microscope was used actively while drawing. The grain boundary digitization was achieved by turning the visibility of the layers on and off and gradually drawing the grain boundaries with maximum accuracy. The mineral phase of each grain was manually added by placing a point within each grain and assigning phase information to each particular point. Through the combination of a polygonal line file holding all drawn grain boundary data and a point file containing phase data, a complete digitized grain boundary map with phase identifications for each map was generated for each sample; see Figure 2.3-1 for general digitizing layer-arrangement.

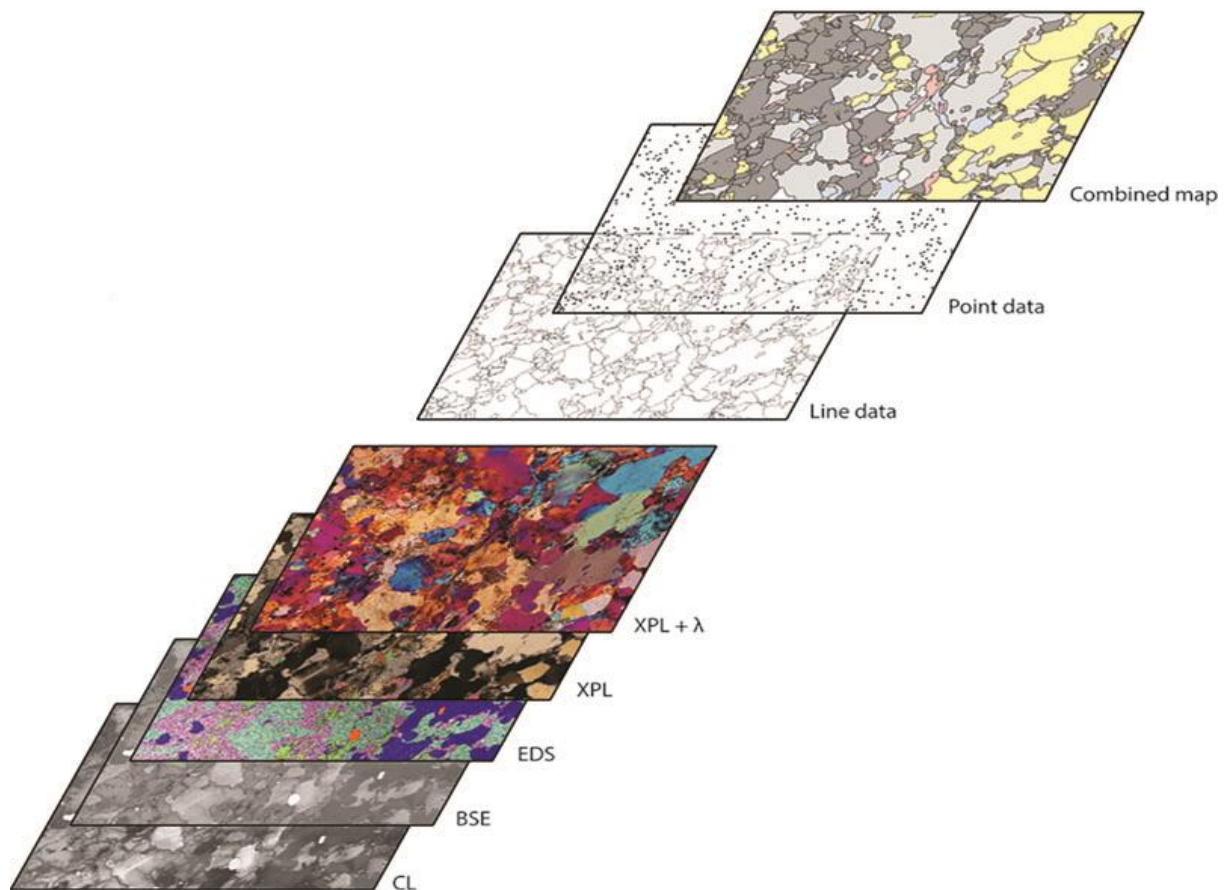


Figure 2.3-1 QGIS digitizing layer-arrangement with showing the different types of input images in the order that they were used (bottom left) and the two different types of output files (line and point data) along with a MATLAB-generated map combining the two output files (top right)

2.4 Statistical analysis using MATLAB™ and PolyLX toolbox

The main focus of the statistical analysis of the four microstructural types was to assess grain size and contact frequencies of K-feldspar, plagioclase and quartz. The statistical evaluation of the samples involved a substantial amount of programming in MATLAB™ through a combination of built-in functions and functions provided in the PolyLX MATLAB™ toolbox ([Lexa, n.d.](#)). In addition, the program STRIPSTAR and the image processing program Image J was used for parts of the grain size analysis ([Heilbronner and Bruhn, 1998](#)).

Grain size

Thin sections are two-dimensional cross-sections of objects in three-dimensional space, and as such the grain size distributions will generally differ from the true size distributions measured in 3D space. Two factors control the deviation from the true distribution; (1) a random cross-section of a grain can be smaller but never larger than the grain; and (2) there is a higher probability of larger grains being included in the random sectioning as they offer a larger intersection area when compared to smaller grains ([Dalen and Koster, 2012](#)). As a result, 2D sections will never accurately represent the true size of sampled grain.

Equal diameter is a widely used measure of particle size and it could be expressed in two ways; (1) in 2D, as the diameter of a circle having the same area as the assessed grain (equal area diameter or EAD, Figure 2.4-1 a) and; (2) in 3D, where it corresponds to the diameter of a sphere of equal volume (Figure 2.4-1 b). EAD of digitized grain cross-sections were calculated directly from grain map topologies through the equation;

$$\text{Equal area diameter (EAD)} = 2 \cdot \sqrt{(\text{Measured grain area}/\pi)}$$

Volumetric grain size distributions were obtained through the STRIPSTAR program which generates results identical to the Schwartz-Saltykov method described in [Underwood \(1970\)](#) ([Heilbronner et al., 2010](#)). The STRIPSTAR program calculates the parent distribution of spheres (Figure 2.4-1 b) from the grain size distribution of EAD (Figure 2.4-1 a). Size distributions calculated by STRIPSTAR can feature negative frequencies, a feature that allows the program to account for under-populated or empty bins and complete the calculation. It should be noted that a large number of grains have to be evaluated in order to achieve representative results, for example, 1000 grains have to be evaluated for a 20 bin histogram with a minimum average density of 50 counts per bin ([Heilbronner et al., 2010](#)).

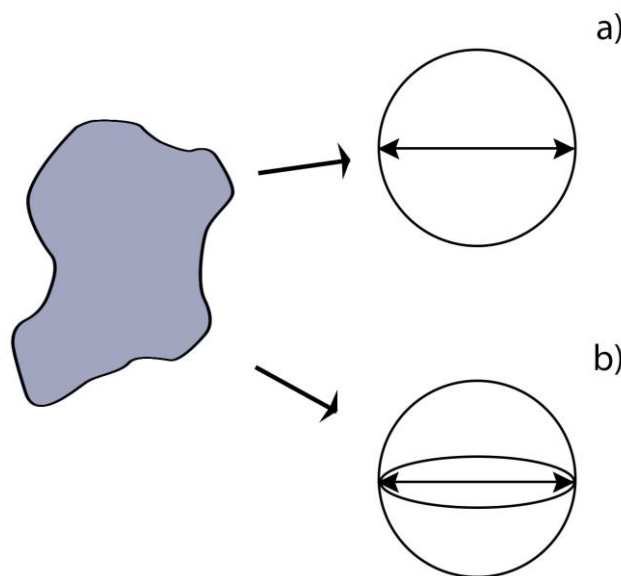


Figure 2.4-1 Equal diameter as a grain size measurement **(a)** in 2D, corresponding to the diameter of a circle of equal area (EAD) and **(b)** in 3D as the diameter of an equivalent sphere.

As a final step of the grain size analysis, grain size maps for K-feldspar, plagioclase and quartz were constructed through the use of JAZY whatever map macro in Image J ([Basel University, n.d](#)). The Jazy grain size mapping colours the evaluated grains based on size or shape and for the purposes of this thesis the grains were colour coded based on their EAD.

Grain contact frequency method

The grain contact frequency method is adapted after [Kretz \(1969\)](#) and is used as a statistical tool to determine to what extent contact relations of certain minerals deviate from a random distribution. The method compares the number of observed contacts (O) shared by two phases with the number of contacts that would be expected (E) for a completely random spatial distribution of the two

phases. The results are given in terms of χ -values, where χ is a measure of the deviation from a random spatial distribution, which is given by the equation:

$$\chi = \frac{\text{Observed contacts} - \text{Expected contacts}}{\sqrt{\text{Expected contacts}}}$$

In the original paper by [Kretz \(1969\)](#), the grain contact frequencies were determined by the use of line intercepts, however in this thesis the determinations were obtained directly from grain map topologies using the PolyLX MATLAB™ toolbox.

2.5 Crystallographic analysis by electron backscatter diffraction (EBSD)

Electron Backscatter Diffraction (EBSD) is a SEM-based technique for attaining crystallographic information for microstructures within crystalline material and is therefore a significant research tool within material science.

2.5.1 Theory behind EBSD

Principally, the EBSD analysis is conducted using a stationary, high-energy electron beam with a shallow angle of incidence on a sample surface in a scanning electron microscope to produce a cone of diffracted electrons, which fluoresces an impeding phosphor screen. This fluorescence produces diffraction patterns which are captured by a specialized camera situated behind the phosphor screen ([Schwarzer et al., 2009](#)). The diffraction patterns consist of intersecting Kikuchi bands, which are typical for particular crystalline solids. The diffraction patterns are computer-analysed to identify the phase, index the pattern and obtain orientation data for analysed spot ([De Graef, 2003](#)). The obtained orientation data is usually described in terms of Euler angles, which can be visualized in a number of ways, one of them is through a Euler map. In Euler maps, the orientation data of individual crystals are presented by plotting the three Euler angles of the crystals using an RGB scheme, these maps only give a rough understanding of the sample microstructure ([Oxford Instruments Plc, 2015](#)). More often, the orientation output is presented as pole figures, translating the obtained 3D orientation to a 2D plot. With pole figures, the arrangement of crystallographic planes is presented rather than the orientations of individual crystals as in Euler maps, the trends that might appear in pole figures allows us to infer sample fabrics.

Thin sections subjected to EBSD analysis need to be carefully prepared before the analysis. The reason why the preparation is such an important factor is that electrons are diffracted from the very surface of the sample, usually no deeper than a couple of tens of nanometers, meaning that any

deformation or contamination of the surface likely will suppress the Kikuchi patterns and hence hamper results of the analysis ([Oxford Instruments Plc, 2016-2017](#)). To achieve optimum Kikuchi pattern intensity, the tilt angle of the sample should be 70 degrees from the horizontal and the distance between the electron gun and the sample (i.e. the working distance) should be 6-12 mm to ensure ideal analytical conditions.

2.5.2 EBSD analysis conditions

As with SEM-imaging, all samples were carbon-coated to reduce any surface charging, the sample was then mounted on an aluminium stage before applying strips of copper tape, functioning as an extra adhesive as well as helping charge-dissipation during subsequent analysis. The EBSD analyses were performed at the Faculty of Health Sciences at UiT the Arctic University of Norway using a Zeiss Merlin VP Compact with an accelerating voltage of 20 kV outfitted with an Oxford instruments HKL Nordlys EBSD detector. The magnification was set to x100 and the step-size was chosen as small as possible for each predefined sample-area while still allowing an overnight run-time of 18-20 hours. Overall, the step-sizes for the analysed samples ranged from 4-8 microns, with the exception of large quartz grains in type I orthogneiss which required a larger area of analysis and consequently a larger step-size of 12 microns. Finally, the output EBSD-data were analysed through Aztec and further post-processed through Channel5, both programs provided by Oxford Instruments Plc.

3 Results

In the following chapter, the results of this work are presented. The chapter will start with a description of the samples, both as they appear in hand specimen and in thin section, before presenting manually redrawn grain maps for each thin section. Then results of the statistical analysis are presented, including grains size statistics, grain boundary frequencies. Finally, results of CPO measurements are presented as pole figures.

3.1 Sample description

The upcoming subchapter concerns the description of four hand specimens and thin sections made of them. The samples were collected and cut by dr. Prokop Závada from the Geophysical Institute of the Czech Academy of Sciences in Prague. All samples were cut perpendicular to the observed (or inferred in the case of the granofels and granulite) foliation and parallel to mineral lineation. As it was described previously by [Závada et al. \(2007\)](#) and [Konopásek et al. \(2014\)](#), formation and subsequent crystallization of low amounts of melt is believed to be the main factor contributing to the change of the fabric and microstructure of the studied samples of metagranitoid rocks. Thus, special attention was paid to the description of grain shapes and nature of contacts among K-feldspar, plagioclase and quartz, as well as an overall description of the microstructure in which these mineral phases appear.

For macroscopic sample descriptions, hand specimens for type II migmatitic orthogneiss, type III granofels and type IV granulite were available for examination while hand specimen for type I orthogneiss were unfortunately not recovered. As an alternate solution, another hand sample of strongly banded orthogneiss equivalent to the type I orthogneiss taken from the same location, was used for macroscopic descriptions. Thin sections are described using fabric nomenclatures from [Passchier et al. \(2005\)](#) and [Vernon \(2004\)](#).

3.1.1 Type I : Orthogneiss

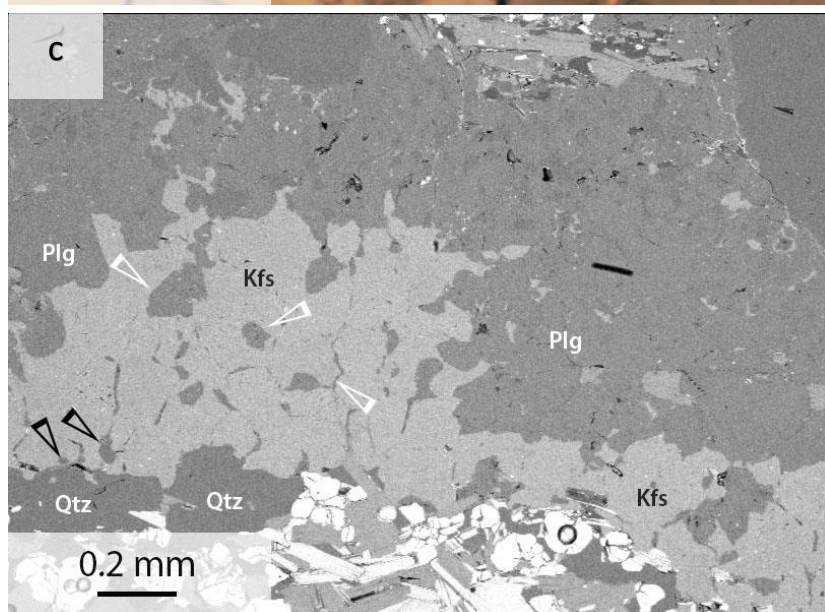
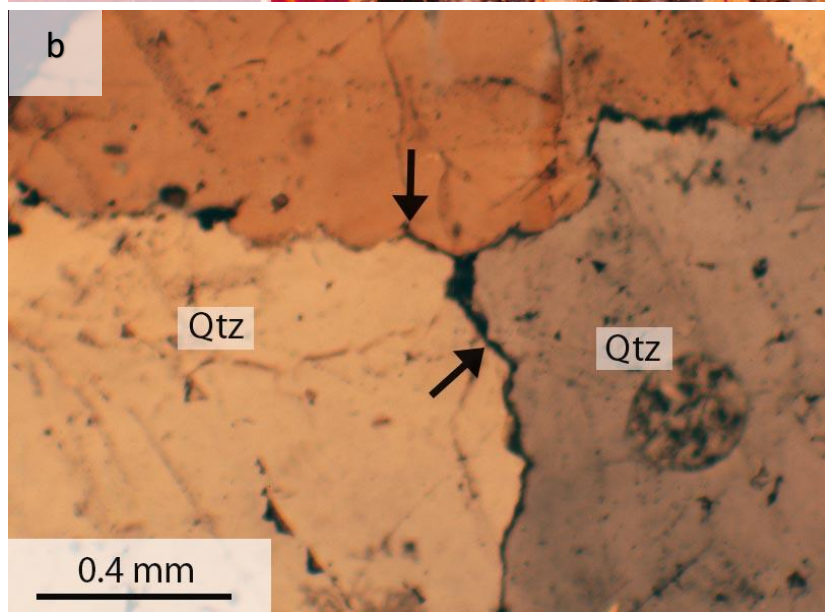
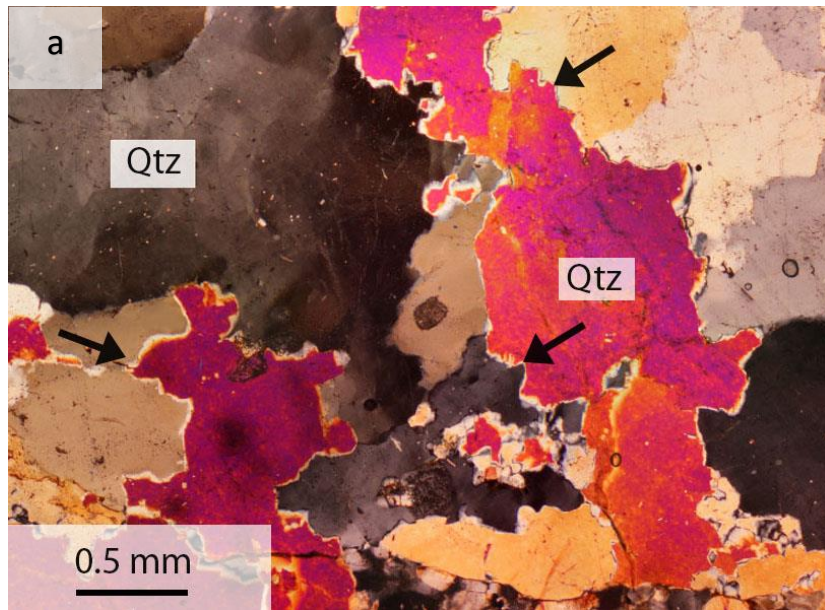
Sample KL22A(B4) is a granitic orthogneiss from Zámecký park in Klasterec (N 50.3841376 E 13.1768775). The sample is macroscopically characterized by a gneissic microstructure consisting of alternating 0.1-0.4 cm wide monomineralic bands of quartz, plagioclase and K-feldspar separated by 0.1-0.2 cm intermittent mica-rich bands (Figure 3.1-1). Both the hand specimen and field outcrop show signs of folding.



Figure 3.1-1 Hand sample EC8Y, type I orthogneiss, corresponding to macroscopic appearance of sample KL22-A.

The sample equilibrated under upper amphibolite facies conditions ([Konopásek et al., 2014](#)) and has the mineral assemblage quartz (25-35%), K-feldspar (35-45%), plagioclase (20-30%), muscovite (1-5%), biotite (1-5%), minor amounts of garnet (1-3%) and accessory amounts of rutile, apatite and zircon. Biotite has $X_{Fe} = 0.54-0.55$ while garnet has $X_{Fe} = 0.83$ and is compositionally (%) made up of Alm_{66} , Py_{13} , GrS_{13} , Sps_1 . Plagioclase within this sample contained 2-14% of the An component and 0-2% of the Kfs component while K-feldspar contains 3-14% of Ab and 0% An (mineral chemistry obtained from [Konopásek et al. \(2014\)](#)).

Microscopically, the type I orthogneiss shows a completely recrystallized microstructure with alternating bands of feldspars and quartz without relict porphyroclasts. Quartz aggregates are made up of large grains with highly interlocking intraphase boundaries occasionally with individual grains exhibiting sweeping undulose extinction (Figure 3.1-2 a). The intraphase quartz boundaries are generally forms straight zig-zag segments upon close inspection (Figure 3.1-2 b). Smaller quartz grains are rounded to elongated and mostly situated within K-feldspar aggregates (Figure 3.1-2 c) and in association with mica rich domains. Feldspar bands are largely monomineralic, consisting of a mosaic of equidimensional grains with straight interphase boundaries and numerous 120° triple junctions, exhibiting typical foam microstructures (Figure 3.1-2 d and e). Plagioclase bands contains randomly oriented interstitial muscovite while K-feldspar bands contain both interstitial grains of quartz and plagioclase often forming thin elongated grains lining K-feldspar boundaries or occurring as isolated grain along boundaries and in triple junctions (Figure 3.1-2 c).



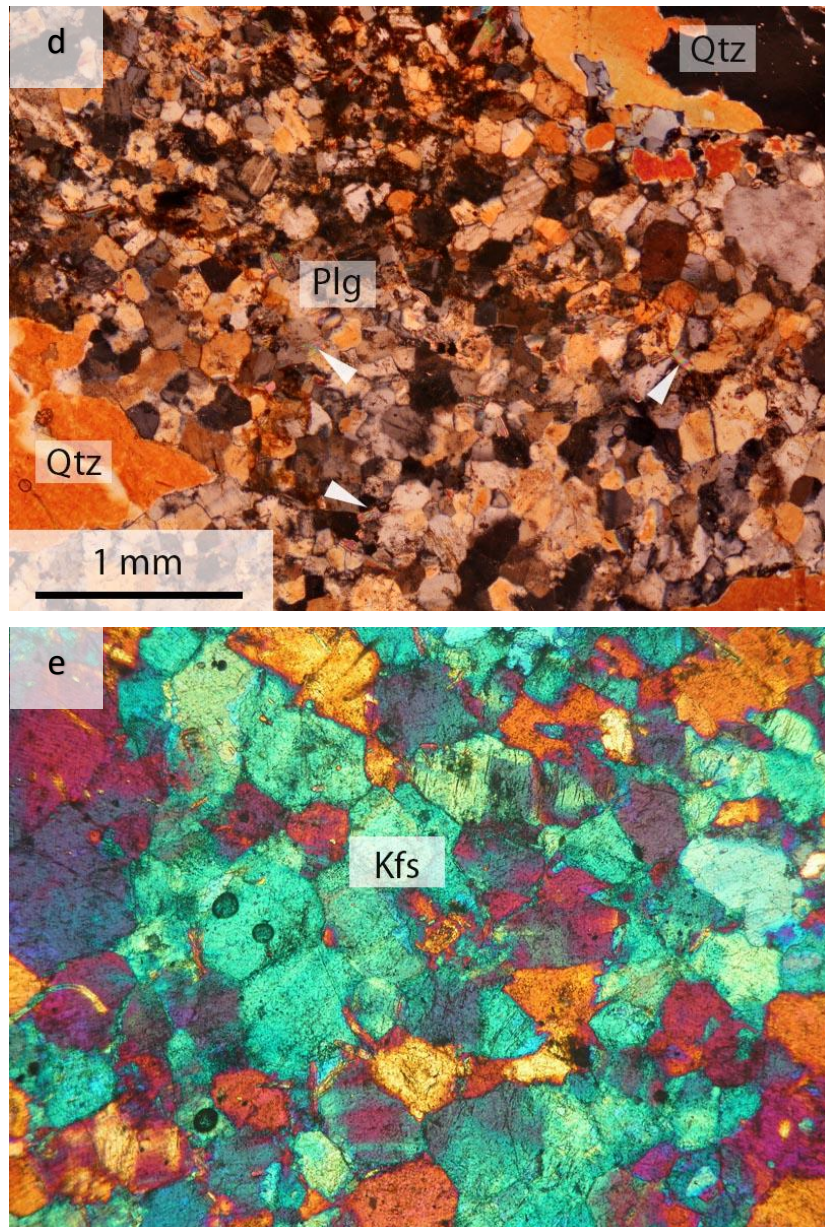


Figure 3.1-2 Details of BSE and photomicrographs for type I orthogneiss. **(a)** Interlocking intraphase quartz boundaries (white arrows) in contrast to the relatively straight boundaries with adjacent Kfs aggregates. Quartz shows anomalous interference colours due to larger thickness of the thin section. **(b)** Close-up of quartz intraphase boundaries showing that quartz intraphase boundaries form angular zig-zag patterns (white arrows). **(c)** BSE images showing interstitial grains of plg (white arrow) and qtz (black arrow) within a thin Kfs band. **(d)** Polygonal microstructure exhibited by a (largely) monomineralic plagioclase band with subordinate amounts of interstitial muscovite (white arrows). **(e)** Photomicrograph of polygonal texture of K-feldspar aggregates taken under cross polarized light with the retardation plate inserted. The image unfortunately has no scale but generally the diameter of individual K-feldspar grains within this sample lies between 0.1-0.4 mm

3.1.2 Type II : Migmatitic orthogneiss

Sample EZ 22P from Krvava skala in Kadan (N 50.3731064 E 13.2762747E), is a migmatitic orthogneiss with 0.1-0.3 mm thick discontinuous, diffusely separated bands of felsic material with thin 0-0.1 mm

mica-rich domains (Figure 3.1-3). Apart from a few relict quartz bands, the bands of quartz, plagioclase and K-feldspar in this sample are not strictly monomineralic as in the type I orthogneiss. Within the hand sample, crystallized melt is present in shear bands oblique to the foliation, which macroscopically indicates a certain degree of rock migmatization. The sample has the same mineral assemblage as type I orthogneiss, containing quartz (25-35%), K-feldspar (30-45%), plagioclase (20-30%), muscovite (1-5%), biotite (1-5%) and accessory garnet, rutile, apatite and zircon. Unfortunately, there is no microprobe data for the migmatitic orthogneiss.



Figure 3.1-3 Hand sample EZ 22P, type II migmatitic orthogneiss. Image illustrates the macroscopic appearance of the migmatitic orthogneiss. Notice crystallized melt in shear bands obliquely crosscutting the gneissic foliation

Microscopically the type II migmatitic orthogneiss consists of alternating bands of felsic minerals dominated by either K-feldspar, plagioclase or quartz with thin bands consisting of biotite and muscovite. Quartz grains in relicts of aggregates have lobate interphase boundaries with K-feldspar and plagioclase (Figure 3.1-4 a), while their intraphase boundaries form more or less straight segments (Figure 3.1-4 b). Interstitial grains of quartz form rounded to elongated grains situated within K-feldspar- or plagioclase-rich domains. K-feldspar- and plagioclase-aggregates are built up of larger, irregularly shaped grains with gently curved intraphase boundaries. Interstitial K-feldspar and plagioclase are round to elongate and sometimes exhibits cusped shapes. The interstitial grains of

quartz, plagioclase and K-feldspar is situated within domains dominated by the other felsic phases (i.e Plagioclase is found within K-feldspar and/or quartz dominated domains). Vermicular intergrowths of quartz in plagioclase (myrmekites) occur within this sample ([Vernon, 2004](#)).

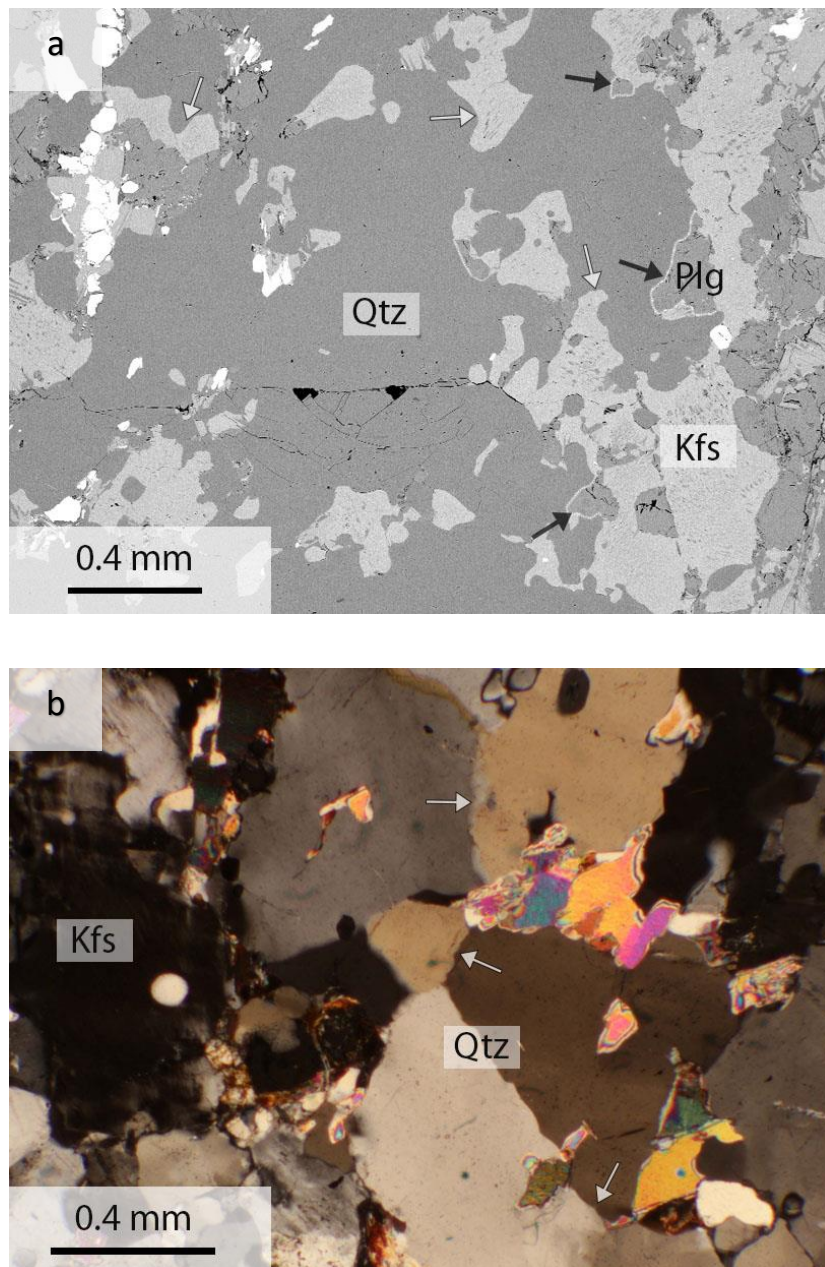


Figure 3.1-4 Details of BSE and photomicrograph for type II migmatitic orthogneiss. **(a)** BSE image showing microstructure on the border of a quartz dominated domain (middle) and a Kfs dominated domain (right) with interlobate Qtz-Kfs (white arrows) and Qtz-plg (black arrows) boundaries. **(b)** Quartz aggregate (center) with straight to gently curved nature of quartz intraphase boundaries (white arrows).

3.1.3 Type III : Granofels

Sample EZ 22R from Krvava skala in Kadan (N 50.3731064 E 13.2762747E), is a granofels characterized by a diffuse macroscopic foliation defined by subparallel orientation of micas (Figure 3.1-5). The sample largely exhibits a granoblastic microstructure and it is interpreted as an intermediate stage between the type II migmatitic orthogneiss and the granulite. The granofels has the mineral assemblage quartz (30-40%), K-feldspar (30-40%), plagioclase (20-30%), biotite (2-4%), muscovite (1-3%) along with accessory garnet, apatite, rutile and zircon in addition to very limited occurrences of kyanite.



Figure 3.1-5 Hand sample EZ 22R, type III granofels. Sample shows diffuse foliation defined by subparallel alignment of mica.

In the sample biotite has $X_{Fe} = 0.54-0.57$ while garnet has $X_{Fe} = 0.87-0.91$ and the composition (%) $Alm_{72-78}, Py_{8-11}, Grs_{8-12}, Sps_1$ (Table 3.1-1). Plagioclase ($An_{12-14}Kfs_{1-2}$) has sporadic albitic rims ($An_{0-2}Kfs_{0-1}$) along contacts with K-feldspar ($Ab_{10-14}An_0$) (Table 3.1-1). Relicts of K-feldspar, plagioclase and quartz-aggregates are irregularly shaped with lobate interphase boundaries and generally curved to slightly lobate intraphase boundaries. Smaller grains of feldspars and quartz are commonly present as rounded and elongated grains within domains dominated by the other felsic phases (Figure 3.1-6 a). As in the type II orthogneiss, myrmekites are present within this sample along with intergrowths of quartz in muscovite (Figure 3.1-6 a)

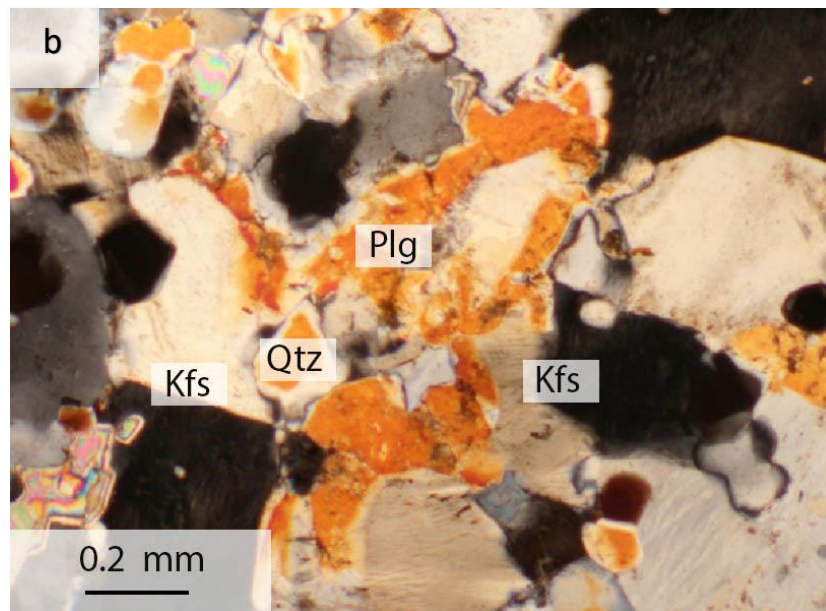
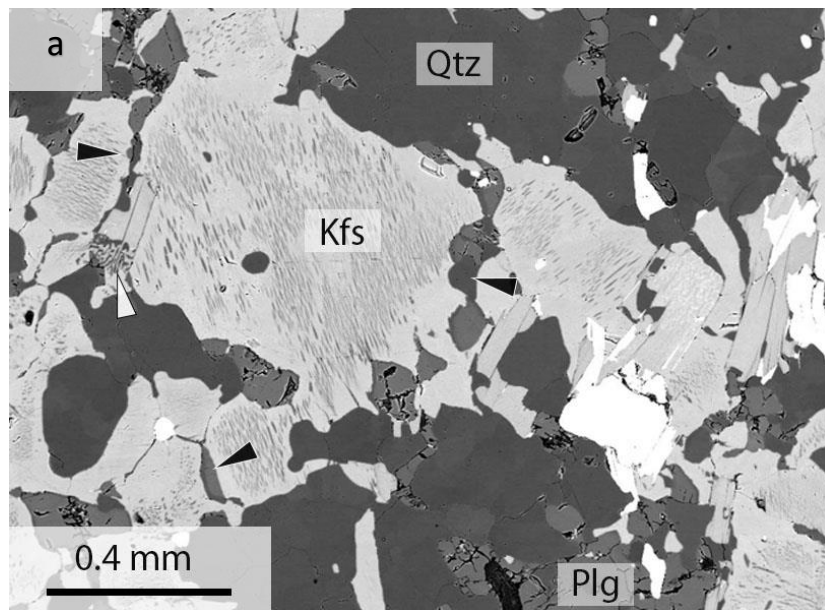


Figure 3.1-6 Details of-BSE image and photomicrograph for type III granofels. **(a)** BSE image showing typical microstructure of relict aggregates, in this case Kfs. Interstitial grains are still recognizable along grain boundaries within relict aggregates (black arrows) and intergrowths of quartz in muscovite (white arrow) are common occurrence within the microstructure. **(b)** Corroded plg grain with highly irregular interphase boundaries toward Kfs and Qtz. The anomalous colours exhibited by minerals in the image are a consequence of the thickness of the thin section.

3.1.4 Type IV : Granulite

In hand specimen, sample EZ 22S from Kadan (N 50.3731064 E 13.2762747E) appears to have a very faint gneissic foliation defined by alternating subparallel polymineralic layers and interstitial biotite (Figure 3.1-7). This faint banding locally disappears and the rock shows homogenous granoblastic areas from which the thin section of this sample was cut. The sample equilibrated at granulite facies conditions (Konopásek et al., 2014) and has the mineral assemblage quartz (30-40%), K-feldspar (30-40%), plagioclase (20-30%) garnet (2-5%), biotite (1-4%) and accessory rutile, apatite, kyanite and zircon and very limited occurrences of late muscovite.

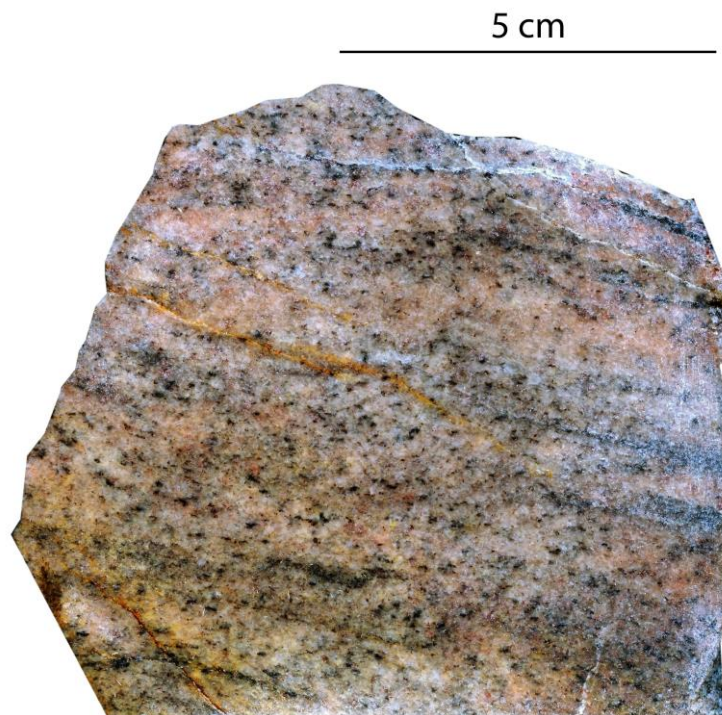


Figure 3.1-7 Hand sample EZ 22S, type IV granulite with a close to a granoblastic appearance. Notice faint foliation which can be inferred from the sub-parallel alignment of interstitial biotite and alternating polymineralic felsic layers.

The granulite microstructure is characterized by dispersed felsic phases where larger grain relicts of aggregates are intermixed with smaller grains (Figure 3.1-8 a). A weak foliation which can be inferred from the sub-parallel orientations of interstitial biotite ($X_{Fe} = 0.49-0.52$) which often occurs as corroded grains (Figure 3.1-8 b). Garnets ($X_{Fe} = 0.77-0.80$) form isometric crystals with the following end-member ratios (%): Alm₆₅₋₇₈, Py₁₃₋₂₀, Grs₇₋₁₃, Sps₁. Entirely dispersed K-feldspar (Ab₁₁₋₁₄An₀), plagioclase (An₁₀₋₁₅Kfs₁₋₂) and quartz generally form anhedral grains with lobate interphase boundaries and straight or gently curved intraphase boundaries (see Table 3.1-1 for mineral chemistry). Plagioclase exhibits sporadic albitic rims (An₀₋₂Kfs₀₋₁) along contacts with K-feldspar (Figure 3.1-8 c). Diffusely defined myrmekites sometimes occur within this sample.

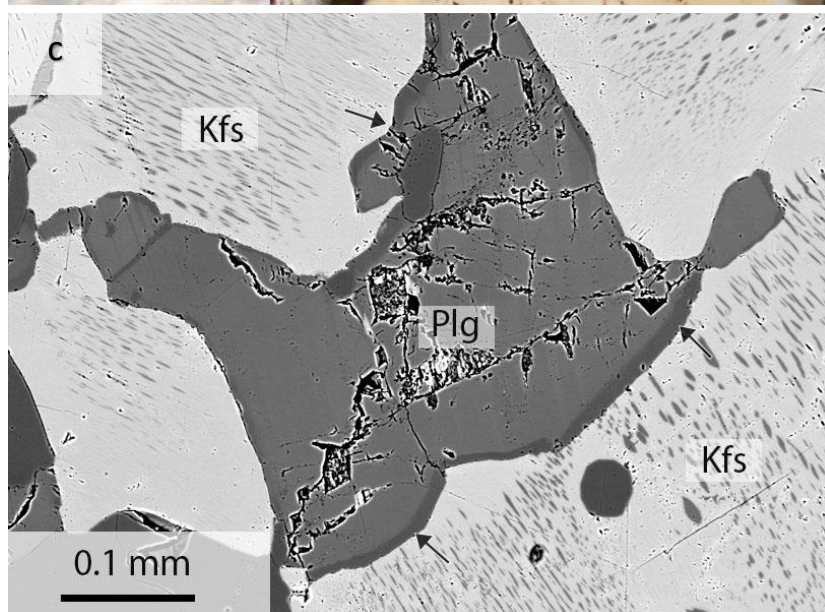
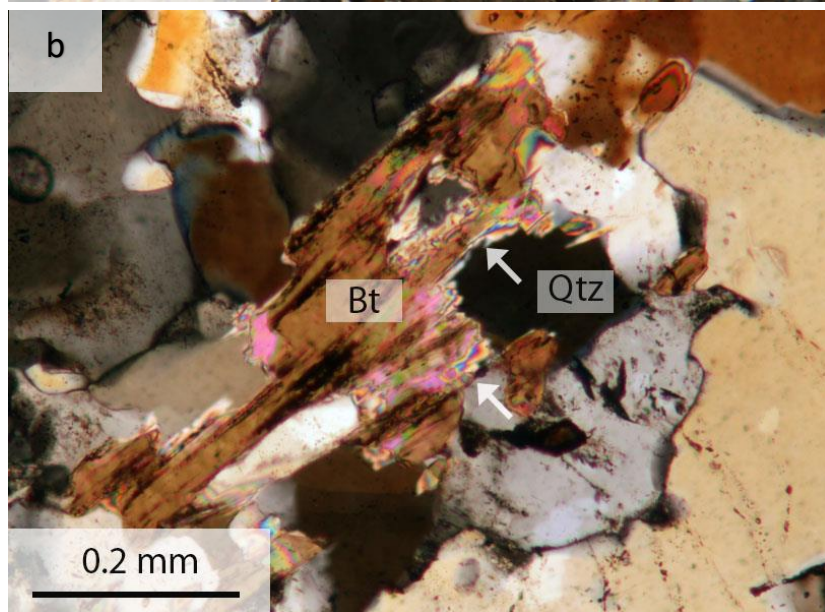
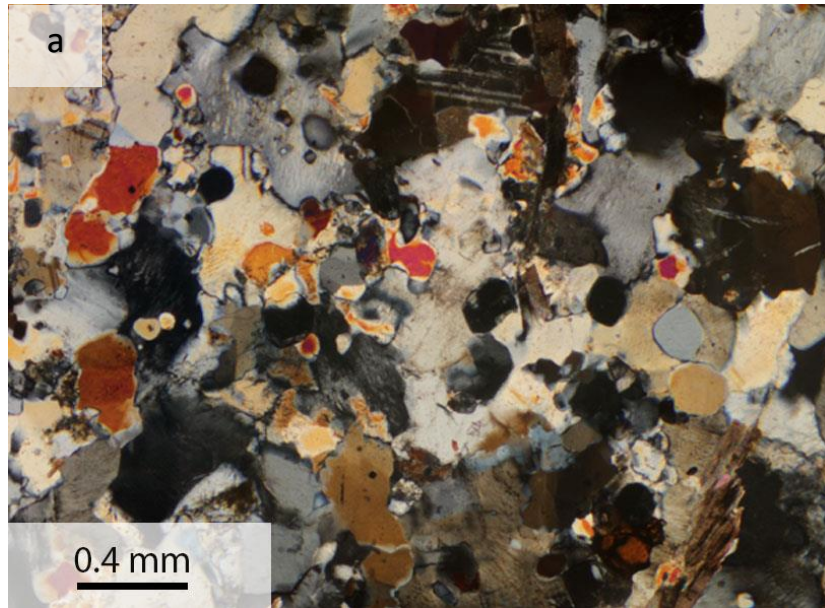


Figure 3.1-8 Details of BSE-image and photomicrograph for type IV granulite. **(a)** typical microstructure of type IV granulite, where irregular larger grain relicts are intermixed with smaller grains. Due to lack of feldspar twinning, the two phases can only rarely be distinguished based on microscopy alone. **(b)** Corroded biotite grain embayed with quartz. **(c)** albitic rims (white arrows) lining a plagioclase aggregate along certain boundaries plg-Kfs boundaries.

Table 3.1-1 Results of microprobe analysis of minerals for type III granofels and type IV granulite. In calculation of molar proportions all Fe is taken as Fe+2, ignoring the possibility of Fe+3 presence

	Type III : Granofels					Type IV : Granulite				
	Biotite	Garnet core	Garnet rim	Plagioclase	K-feldspar	Biotite	Garnet core	Garnet rim	Plagioclase	K-feldspar
<i>Weight percent</i>										
SiO ₂	37.57	37.43	37.28	65.35	65.6	37.32	38.12	38.07	65.27	65.31
TiO ₂	3.56	0.03	0.04	0.01	0.01	3.18	0.04	0.03	0.00	0.01
Cr ₂ O ₃	0.00	0.01	0.01	0.01	0.01	0.01	0.01	0.01	0.01	0.01
Al ₂ O ₃	15.92	21.30	20.94	21.77	18.51	16.57	21.34	21.29	21.80	18.58
FeO	19.36	34.01	34.83	0.01	0.05	17.93	31.39	32.51	0.02	0.01
MnO	0.03	0.54	0.57	0.01	0.00	0.04	0.47	0.51	0.00	0.01
MgO	8.90	2.81	2.54	0.00	0.00	10.14	4.74	4.56	0.00	0.00
CaO	0.00	4.41	4.13	2.77	0.00	0.00	4.44	3.67	2.83	0.00
Na ₂ O	0.07	0.04	0.04	9.78	1.32	0.05	0.03	0.02	9.69	1.38
K ₂ O	9.85	0.00	0.00	0.27	14.89	9.76	0.00	0.00	0.26	14.81
F	2.80	-	-	-	-	0.93	-	-	-	-
Cl	0.14	-	-	-	-	0.2	-	-	-	-
Total	98.20	100.58	100.38	99.98	100.39	96.13	100.58	100.66	99.89	100.13
<i>Molar proportion</i>										
Si	2.86	2.99	2.99	2.87	3.00	2.83	3.00	3.00	2.78	3.00
Ti	0.2	0.00	0.00	0.00	0.00	0.18	0.00	0.00	0.00	0.00
Cr	0	0.00	0.00	0.00	0.00	0.00	0.00	0.00	-	-
Al	1.43	1.99	1.98	1.13	1.00	1.48	1.98	1.98	1.13	1.01
Fe _{tot}	1.23	2.28	2.37	0.00	0.00	1.14	2.07	2.14	0.00	0.00
Mn	0	0.04	0.04	0.00	0.00	0.00	0.03	0.03	0.00	0.00
Mg	1.01	0.34	0.29	0.00	0.00	1.15	0.56	0.54	0.00	0.00
Ca	0	0.38	0.34	0.13	0.00	0.00	0.37	0.31	0.13	0.00
Na	0.01	0.01	0.00	0.83	0.12	0.01	0.00	0.00	0.83	0.12
K	0.96	0.00	0.00	0.01	0.87	0.94	0.00	0.00	0.01	0.87
F	0.68	-	-	-	-	0.03	-	-	-	-
Cl	0.02	-	-	-	-	0.22	-	-	-	-
<i>Garnet Fe-Mg ratio</i>										
X _{Fe}	0.55	0.87	0.89			0.50	0.79	0.80		
<i>Feldspar composition</i>										
An%				13	0				14	0
Kfs%				1	88				1	88
Ab%				85	12				85	12

3.2 Quantitative microstructural analysis

Quantitative microstructural analysis of the four samples is based on statistical evaluation of digitized grain maps in terms of grain size and grain contact frequency. The results presented in this chapter were attained through the use of MATLAB™, PolyLX toolbox for MATLAB™ ([Lexa, n.d](#)), Image J and the STRIPSTAR program ([Heilbronner and Bruhn, 1998](#)).

3.2.1 Grain maps

In this section, the microstructure of the four investigated samples is presented as manually redrawn grain maps. The main focus in the redrawing was to accurately portray the sample microstructure. Particular effort went into redrawing the nature and occurrence of quartz, K-feldspar and plagioclase grains. As these minerals crystallize from the partial melt, it enables analysis of how the microstructure changes through the evolutionary sequence of samples.

The produced grain maps represent XZ sections of the four samples and these are presented with same the scale in Figure 3.2-1, for larger images of each individual grain map, see appendix A. The grain maps in Figure 3.2-1, reflect what has already been described in the preceding chapter, namely that there is a gradual disappearance of the compositional banding between the sample of anisotropic orthogneiss to the homogenous granulite.

To achieve reliable results from the statistical analysis, approximately 2000 grains were digitized for each sample (for full overview see Table 3.2-1). The compositional banding in the type I and II orthogneisses poses challenges when it comes to digitizing, where the main difficulty lies in deciding which area within the thin section is the most representative for the sample and therefore appropriate to redraw. Because of the strong anisotropy in the orthogneisses, the modal proportions strongly depend on the analysed area (i.e. the relative proportions of redrawn Kfs, plg and qtz bands) and therefore it would require a much larger sampling pool than ~2000 grains to achieve a statistically representative number of grains. From the area percentages of K-feldspar, plagioclase and quartz in Table 3.2-1 it becomes clear that the digitized maps in the two orthogneisses (type I and type II microstructure) do not span a large enough area to accurately reflect the whole-rock mineral proportions. Even though the modal proportions of feldspars and quartz for the orthogneisses are somewhat invalid, the size of the redrawn area is believed to be valid for the statistical analysis of the changes in terms of the grain size, grain contact frequencies and other microstructural parameters.

Table 3.2-1 Table showing the number of digitized grains and their area percentage within each of the samples subdivided by phase (Kfs, plg and Qtz). Note that area percentages for the orthogneiss and migmatitic orthogneiss is in cursive as they do not fully represent the whole-rock relationship of the major phases.

	Number of digitized grains				Area percentage			
	Kfs	Plg	Qtz	<i>Total (includes all phases)</i>	Kfs	Plg	Qtz	<i>Other</i>
Orthogneiss	380	549	265	2038	16,5	15,2	63,6	4,7
Migmatitic orthogneiss	515	620	475	2211	19,2	23,4	44,7	12,6
Granofels	598	518	577	1996	32,1	21,6	38,1	8,2
Granulite	597	590	623	2047	34,8	23,3	36,1	5,8

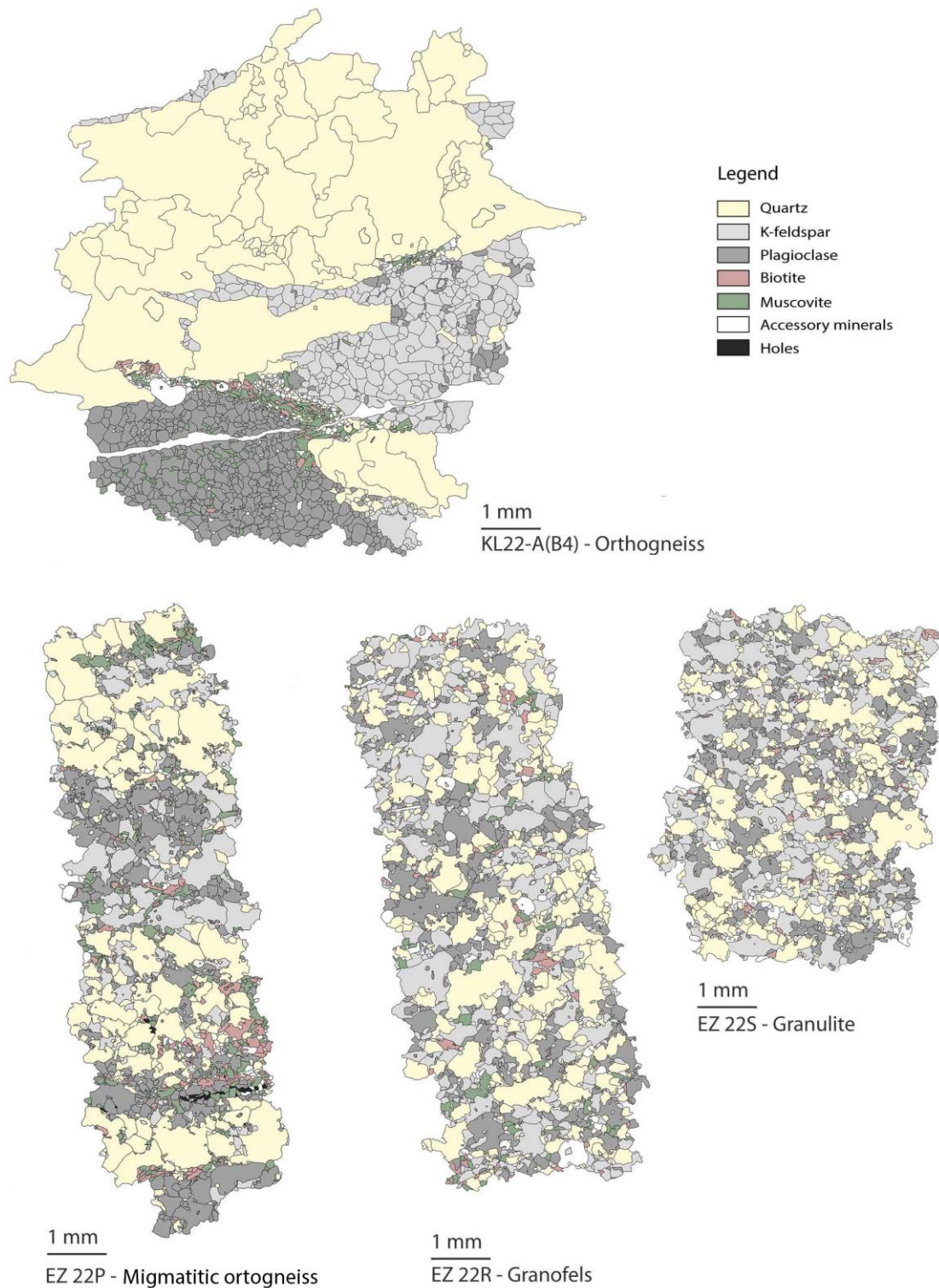


Figure 3.2-1 Digitized grain maps showing the microstructural character of XZ sections of the investigated samples. Type I orthogneiss (top) exhibits distinct monomineralic banding consisting of alternating polygonal mosaics of plg and Kfs and ribbons of quartz discretely separated of bands of $bt \pm gt \pm ms \pm ru \pm ap \pm cor$. Type II migmatitic orthogneiss (bottom left) consists of alternating qtz-, Kfs- and plg-rich domains, partly separated by $bt \pm gt \pm ms \pm ru \pm ap \pm cor$ rich domains. Type III granofels (bottom middle) has diffuse alternations between qtz-, Kfs- and plg-rich domains with interstitial micas approaching a granoblastic texture. Type IV granulite (bottom right) consisting of intermixed qtz, Kfs and plg with minor amounts of $bt \pm gt \pm ky \pm ap$. The grain maps are all represented with equal scale and are oriented so that the main foliation of the sample is horizontal.

3.2.2 Grain size

Grain size distributions were evaluated for K-feldspar, plagioclase and quartz within the microstructural rock types of the studied quartzofeldspathic rocks. The mean grain size is expressed in terms of median EAD (Figure 2.4-1 a), which is the most widely used measure of particle size. The full range of the 2D distributions of grain sizes is illustrated by the grouped box plots in Figure 3.2-2 where the “box” marks the limits of the interquartile range (IQR), containing 50% of the dataset entries while the horizontal line within the “box” marks the median. In 2D, the studied grains follow a right-skewed log-normal distribution where most of the grains are concentrated within the lower end of the grain size spectra, reflected by the right skewed median in Table 3.2-2 and in both Figure 3.2-2 and Figure 3.2-3. In order to fully investigate the evolution of grain sizes, volumetric grain size distributions (Figure 3.2-3) expressed in terms of equal volume diameters (Figure 2.4-1 b) were calculated. These show the parent distribution of spheres that would show the measured cross-sectional areas measured in 2D. The volumetric grain size distribution for K-feldspar, plagioclase and quartz were calculated from frequency weighted histograms of EAD measurements through the use of the STRIPSTAR program. Some outliers were omitted in the evaluation of the volumetric grain size distribution (Figure 3.2-3), for the full range of the dataset see Figure 3.2-2. The volumetric grain size distributions are presented together with the median EAD values to point out the difference in distribution from 2D to 3D. The numerical median values presented or mentioned in this chapter corresponds to measured cross-sectional EAD, unless stated otherwise. The reason being that the 3D distributions and associated statistics calculated by STRIPSTAR is based on frequencies of binned 2D-data and not the individual data entries.

A visual representation of how the various grain sizes are distributed throughout the evaluated area was achieved through colour-coding of grains based on their EAD. The color-coding procedure was carried out in the image processing program Image J. Due to the quantity and large size of the resulting images, only grain size maps for quartz (Figure 3.2-4) are presented within the text of the thesis, whereas the grain size maps for K-feldspar and plagioclase are located in appendix B.

Table 3.2-2 EAD measurements of K-feldspar, plagioclase and quartz in millimetres in terms minimum, median and maximum values for grains within types I-IV.

	EAD measurements, mm								
	K-feldspar			Plagioclase			Quartz		
	<i>min</i>	<i>median</i>	<i>max</i>	<i>min</i>	<i>median</i>	<i>max</i>	<i>min</i>	<i>median</i>	<i>max</i>
Orthogneiss (type I)	0,023	0,137	0,551	0,024	0,109	0,371	0,014	0,073	2,260
Migmatitic orthogneiss (type II)	0,005	0,049	0,760	0,011	0,065	0,610	0,011	0,050	1,046
Granofels (type III)	0,010	0,075	0,770	0,012	0,068	0,683	0,007	0,065	0,957
Granulite (type IV)	0,008	0,058	0,543	0,009	0,058	0,512	0,006	0,058	0,835

3.2.2.1 K-feldspar grain size analysis

Evaluated K-feldspar grains within type I orthogneiss range in size from 0.023 to 0.551 mm with a median size of 0.137 mm and with few outliers (Table 3.2-2). Figure 3.2-2 shows a slightly right skewed distribution of grains where the lower grain size fractions have a slightly higher frequencies resulting in a right-skewed median and box. However, when looking at the volumetric grain size distribution (Figure 3.2-3 a-I) it becomes evident that the evaluated grains are in fact normally distributed. The slight skewness of the box plot (Figure 3.2-2) is caused by an “over population” of small cross-sectional areas compared to the true distribution, and is eliminated through the calculation of the parent distribution spheres. The observed normal distribution is in accordance with what can be visually observed in the colour-coded grain size map in appendix B, K-feldspar-I.

From type I to type II the grain size range increases in both directions, resulting in a grain size interval between 0.005 and 0.76 mm with a median of 0.049 mm (Table 3.2-2). The volumetric grain size distribution shows that K-feldspar has more of a bimodal distribution caused by an increased proportion of grains with sizes of 0-0.1 mm and 0.375-0.5 mm and a decreased proportion of mid-range sizes (Figure 3.2-3 a-I and a-II). The jaggedness of bins within parts of the size distribution is a result of the sample size being too small to adequately represent the grain size range. The larger grains often occur together with mid-sized grains, while the smaller fractions are mostly dispersed within plagioclase-rich and quartz-rich domains and only rarely occur adjacent to other K-feldspar grains (see appendix B, K-feldspar-II).

In type III granofels, the grain size ranges from 0.010 mm to 0.77 mm with a median value of 0.058 mm (Table 3.2-2). The volumetric grain size distribution shows a slightly increased proportion of grains of larger sizes from type II to type III, which is especially noticeable in the 0.4-0.5 mm population (Figure 3.2-3 a-II and a-III). The smallest population of grains (0-0.1 mm) decreases in

proportion and there is a noticeable shift in the mid-range population toward larger sizes (Figure 3.2-3 a-II and a-III). This shift toward larger grain sizes is also observed in the grouped boxplot (Figure 3.2-2) where both the IQR and median shift upward compared to type II. Grain size map for K-feldspar in type III Granofels (Appendix B, K-feldspar-III) shows that the largest grains are partly dispersed and tend to occur alongside clusters of grains of medium size. Mid-range grains usually appear as partly connected aggregates while the smaller grains still occur as interstitial grains in areas dominated by quartz and plagioclase.

In type IV granulite, the K-feldspar grains range in size from 0.008 to 0.543 mm with a median value of 0.058 mm (Table 3.2-2). Outliers for K-feldspar grains within type IV are closely spaced (Figure 3.2-2) and a relatively random volumetric distribution without any well-defined peaks can be recognized (Figure 3.2-3 a-IV). When comparing the volumetric distributions of microstructural types III and IV, it seems that there is a general tendency for bins showing higher volumes for certain grain sizes to become smaller from the granofels (type III) towards the granulite (type IV), whereas for empty or low-volume bins the opposite is true (Figure 3.2-3 a-III and a-IV). Grain size maps for K-feldspar shows a progressive increase in grain separation, where only few isolated relict aggregates of large- and medium-sized grains are present (Appendix B, K-feldspar-I to K-feldspar-IV). As in types I-III, the smallest K-feldspar grains in type IV granulite occur as isolated interstitial grains in contact with grains of quartz and plagioclase, and only rarely occur in contact with other K-feldspar grains (Appendix B, K-feldspar-IV).

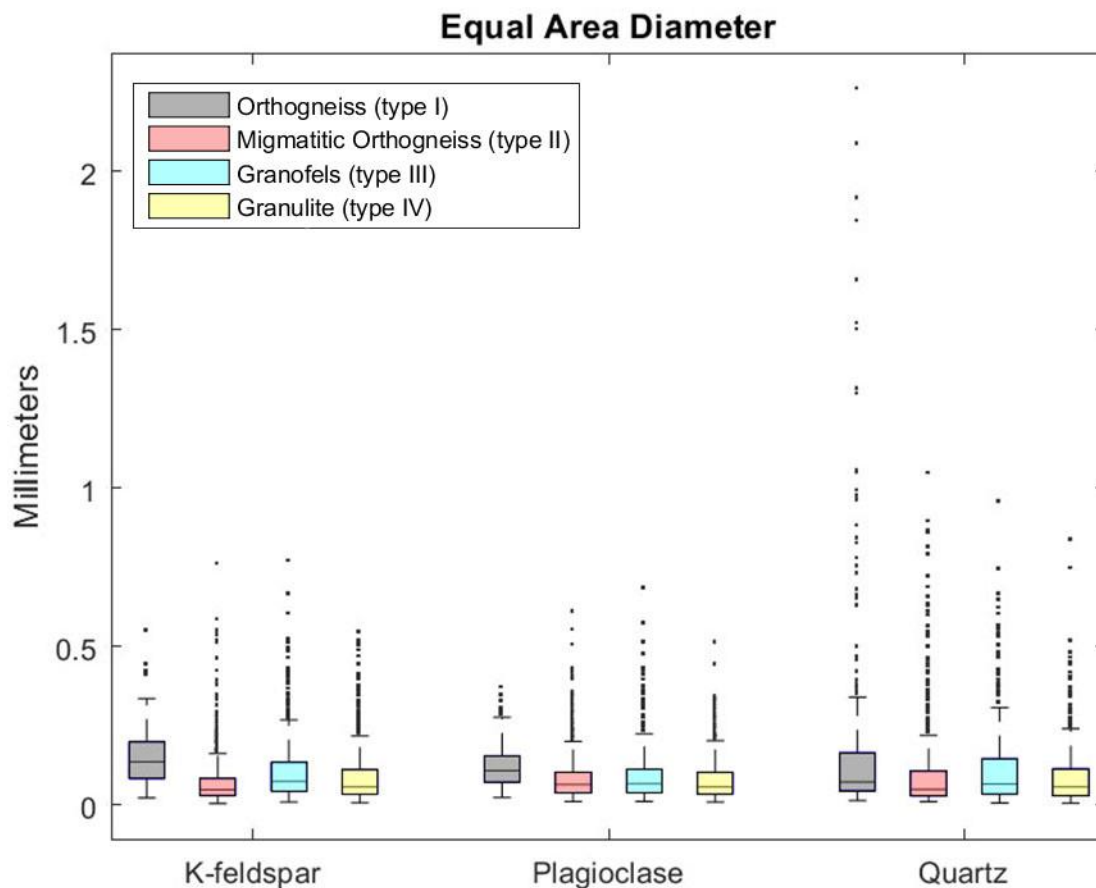


Figure 3.2-2 Grouped boxplot showing the grain size distribution in terms of equal area diameter (EAD) in mm of the data sets for phases within the four microstructural types. The box marks the interquartile range (IQR), the horizontal line within the box marks the median value, whiskers indicate the minimum and maximum values while the outliers are represented as asterisks. In the plot, datasets from orthogneiss are depicted in grey, migmatitic orthogneiss in red, granofels in blue and granulite in yellow.

3.2.2.2 Plagioclase grain size analysis

In type I orthogneiss, plagioclase grains have sizes ranging from 0.024 mm to 0.371 mm with a median of 0.109 and few outliers (Table 3.2-2). From the volumetric grain size distribution in Figure 3.2-3 b-I, it is clear that the grains are normally distributed with high proportions of grains have equal diameters (3D) between 0.1 mm to 0.3 mm. In the type II migmatitic orthogneiss the grains have EADs between 0.011 mm and 0.61 mm with a right-skewed median value of 0.065 mm (Table 3.2-2 and Figure 3.2-2). The volumetric grain size distribution suggest that the grain size follows a bimodal distribution with two peaks, one at 0.075-0.175 mm and another one at 0.325 mm and one intermediate peak, which is likely due to overlapping of tails from the main peaks (Figure 3.2-3 b-II). From type I to type II, the volumetric grain size range spreads out in both directions, with increasing proportions of 0-0.075 mm and 0.3-0.4 mm grains and a decreasing proportion of grains with intermediate size (Figure 3.2-3 b-I and b-II). Larger grains (purple) are associated with medium-sized grains making up the plagioclase-rich domains showing strong clustering tendencies, while the

smaller grain size fractions (yellow) are dispersed adjacent to K-feldspar grains in K-feldspar-rich domains and to quartz in quartz-rich domains, rarely occurring within plagioclase domains (Appendix B Plagioclase-II).

Plagioclase within type III granulites has grain sizes ranging from 0.012 mm to 0.683 mm with a median value of 0.068 mm (Table 3.2-2). These values are similar to the grain size ranges measured in the type II orthogneiss. When compared with type II microstructural stage, the bimodal volumetric grain size distribution in type III granulites shows decreased proportion of 0-0.1 mm grains and a general increased proportion of grains with sizes of 0.3-0.4 mm (Figure 3.2-3 b-II and b-III).

Plagioclase grains larger than 0.25 mm are rarely in contact and if they are, their contact surface is minimal. Grains of medium size either occur as; (1) largely isolated grains or groups of grains adjacent to K-feldspar in K-feldspar-rich domains and to quartz in quartz-rich domains; and (2) in connection with larger grain relicts in plagioclase-rich domains (Appendix B, Plagioclase-III).

In the type IV granulite, the grain size ranges from 0.009 to 0.512 mm with a median value of 0.058 mm (Table 3.2-2). The volumetric grain size distribution for the granulite shows an increased proportion of 0-0.075 mm grains and a decrease in larger sized 0.3-0.4 mm grains. The same distribution also shows that grains larger than 0.35 mm have been eliminated from type III to type IV (Figure 3.2-3 Plagioclase b-III and b-IV). It is however evident from the box plot that there are several outliers above 0.4 mm (Figure 3.2-2). When compared with the type III granulites the plagioclase in type IV granulite shows a narrowing grain size range with the grain size approaching a normal distribution (Figure 3.2-3 Plagioclase b-III and Plagioclase-IV). The granulite grain size maps for plagioclase shows that the grains are largely dispersed where larger grains (purple) are only rarely in contact (Appendix B, Plagioclase-IV).

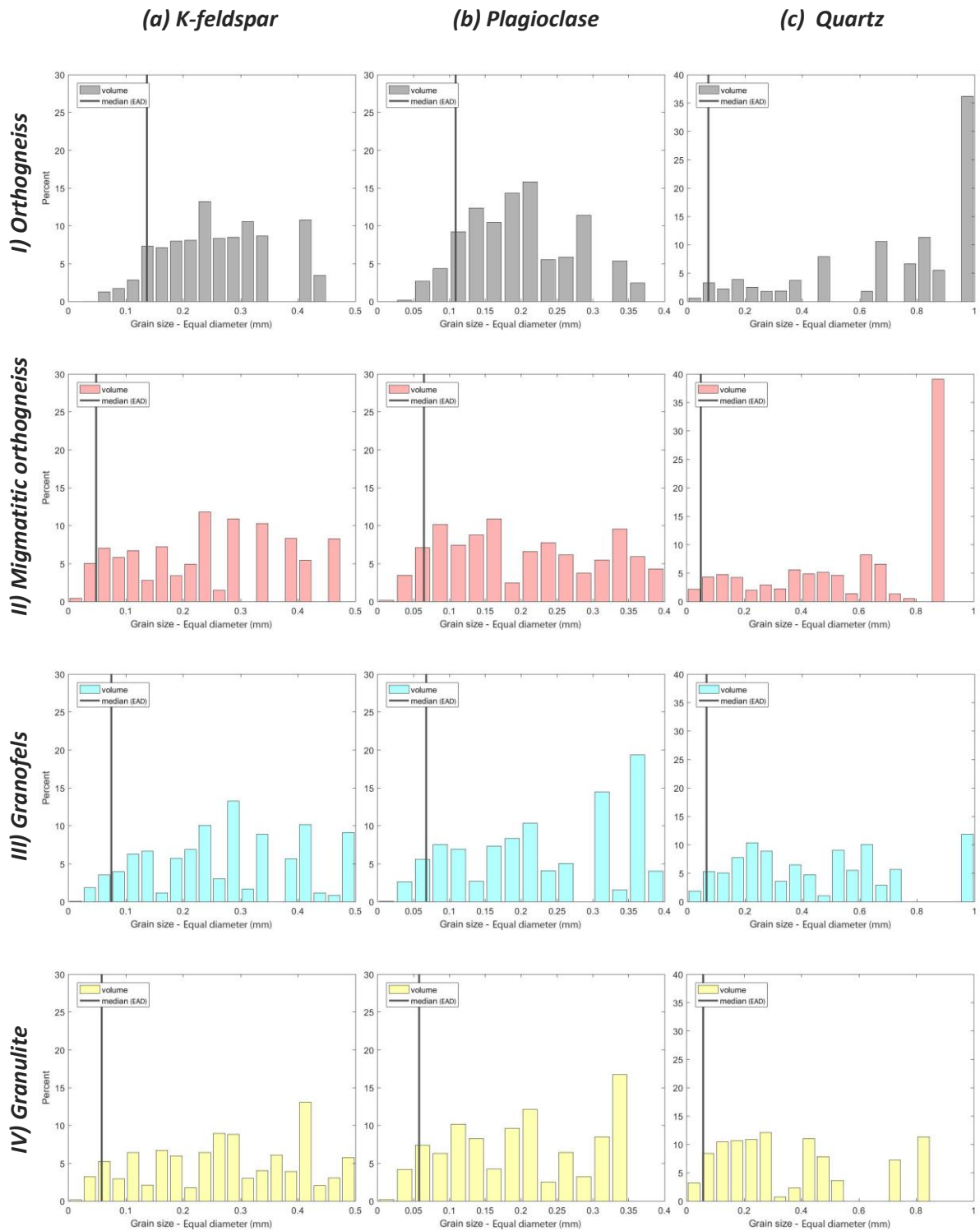


Figure 3.2-3 Grain size distribution for Kfs, plg and Qtz within all textural types (I-IV) where the histogram represents the volumetric distribution in terms of diameter of a sphere of equal volume. The grey vertical line represents the median diameter in 2D (i.e. equal area diameter). The distributions for each phase are within the four textural types are arranged in columns, facilitating direct comparison between distributions within the textural types. All grain size distributions for each separate phase are presented with equal scales on both axes, but when comparing between phases note that the scales differ. Column a) sequential Kfs grain size distributions from type I (grey color) through type II (red color) and III (blue color) and type IV (yellow color). Column b) plg grain size distributions, presented in the same order as in column a. Column c) Qtz grain size distributions for the four textural types presented as in column a and b.

3.2.2.3 Quartz grain size analysis

Quartz grain size in type I orthogneiss ranges from 0.014 mm to 2.26 mm including outliers with a median of 0.073 mm (Table 3.2-2). The 2D grain size data show a strongly right-skewed distribution of the EAD with a large number of outliers (Figure 3.2-2). Volumetrically, the grains can be interpreted to follow a bimodal distribution. A low-volume peak appears close to 0.175 mm and a peak could be inferred from 0.4-1 mm although there are both empty bins and bins with a large volume percentage within this range (Figure 3.2-3 c-I). This indicates that the dataset is not large enough to statistically cover the full range of quartz grain sizes within the sample (Figure 3.2-3 c-I). The bimodal grain size distribution can also be inferred from the grain size map in Figure 3.2-4a where there is a clear divide between grains larger than 0.4 mm occurring as aggregates and <0.25 mm large grains appearing as isolated interstitial grains in mica-rich domains and within K-feldspar aggregates.

In type II migmatitic orthogneiss, quartz ranges in size from 0.011 to 1.064 mm with a strongly right-skewed median value of 0.050 mm (Table 3.2-2). The 3D volumetric distribution of data shows that there is a well-defined peak around 0.1 mm, while the grain sizes above 0.25 mm are rather randomly distributed showing both empty bins and a bin with an extreme value of ~40% (Figure 3.2-3 c-II). Compared to type I, there is a significant reduction of the interquartile range and spread of outliers (Figure 3.2-2). Volumetrically there is an increase in proportion of grains with sizes of 0-0.2 mm and a decreased proportion of grains larger than 0.6 mm compared to the preceding microstructural stage (Figure 3.2-3 c-I and c-II). The grain size maps in Figure 3.2-4 b show that large grains (purple) are considerably less connected and smaller grains (yellow) are more dispersed compared to the type I microstructure. Grains larger than 0.4 mm are generally in contact with other large grains while grains smaller than 0.3 mm mostly appear in mica-, K-feldspar- and plagioclase-dominated domains and only rarely occur adjacent to larger quartz grains (Figure 3.2-4 b).

In the granofels sample (type III) the grains range in size from 0.007 to 0.957 mm with a median grain size of 0.065 mm (Table 3.2-2). The volumetric grain size distribution for this sample suggest a bimodal distribution with peaks at 0.2-0.25 mm and 0.5-0.65 mm (Figure 3.2-3 c-IV). Compared to the 2D distribution in the type II migmatitic orthogneiss sample, the median value and the IQR in type III granofels is slightly shifted toward the larger grain sizes (Figure 3.2-2). Volumetrically, there is an increased proportion of grains with sizes of 0.2-0.5 mm and a decrease in proportion of grains larger than 0.5 mm (Figure 3.2-3 c-II and c-III).

In the type IV granulite, the grain size ranges from 0.06-0.835 mm with a relatively narrow interquartile range and a median grain size of 0.058 mm (Table 3.2-2). The narrow IQR suggest that the grain sizes are relatively closely spaced, at least within this range as it holds 50% of the sampled grains (Figure 3.2-2). This fact is reflected in both the volumetric size distribution where 0-0.6 mm grains are roughly normally distributed and in the grain size maps where the large proportion of mid-sized grains (green to blue) can be directly observed (Figure 3.2-3 c-IV and Figure 3.2-4 d). Compared to the preceding evolutionary stage, the IQR and range of outliers both decrease (Figure 3.2-2). Volumetrically, the grains are normally distributed showing an increase in both small 0-0.1 mm and middle 0.1-0.5 mm grains while the frequency of grains larger than 0.5 decreases (Figure 3.2-3 c-III and c-IV).

3.2.2.4 General trends in grain size evolution

Feldspars

Grain sizes in both feldspars change from a normal distribution in type I orthogneiss toward a bimodal distribution due to an increased frequency of smaller (0-0.075 mm) and larger (0.35-0.5 mm for Kfs and 0.3-0.4 mm for plg) grains relative to mid-sized grains in type II migmatitic orthogneiss (Figure 3.2-3 a-I and II, and b-I and II). As an effect of this change, the IQR and median is shifted toward smaller grain sizes and the IQR also shrinks substantially while the range of outliers increases (Figure 3.2-2). In the type III granofels, the data show an increase of the IQR and slightly higher median value especially in the case of K-feldspar, indicating a larger spread of grain sizes within the IQR compared to type II migmatitic orthogneiss sample (Figure 3.2-2). Volume distribution in the type II granofels shows a decreased proportion of smaller, 0-0.1 mm grains and a slight increase of large grains (0.35-0.5 mm for Kfs and 0.3-0.4 mm for plg) with respect to distributions observed for the stage II migmatitic orthogneiss (Figure 3.2-3 a-II and II, and b-II and III). As the evolution progresses toward the type IV granulite, the distribution of EAD changes again and shows a decrease in the IQR, in the range of outliers, as well as the decrease of the median value (Figure 3.2-2). Such a change is most prominent in K-feldspar. The volumetric grain size distribution shows that there is a slight decrease in the largest grain size fractions for both feldspars (most prominent in the data for plg) and the overall size distribution is close to random in the case of K-feldspar while for plagioclase the grain size approaches a normal distribution (Figure 3.2-3 a-IV and b-IV).

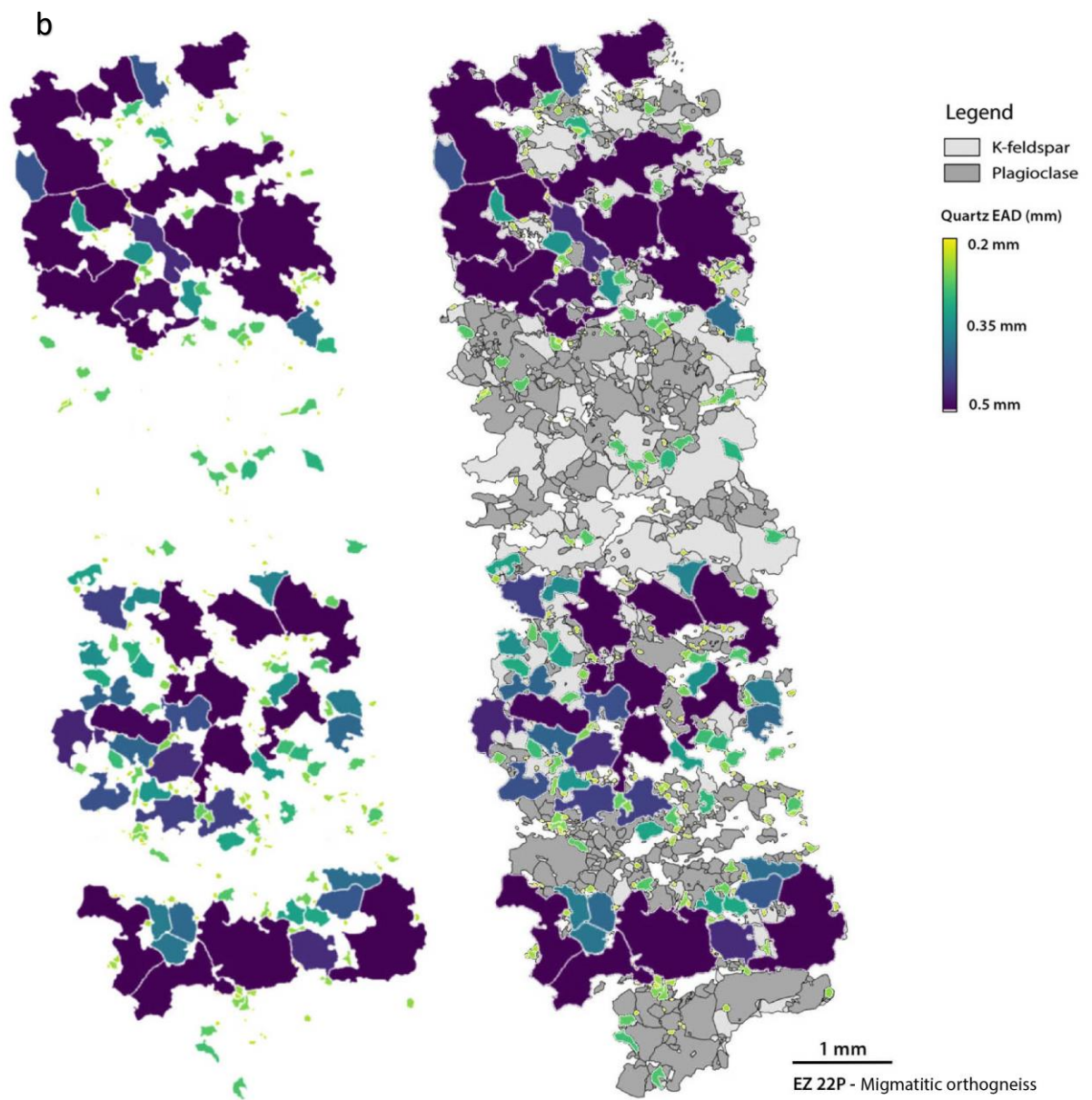
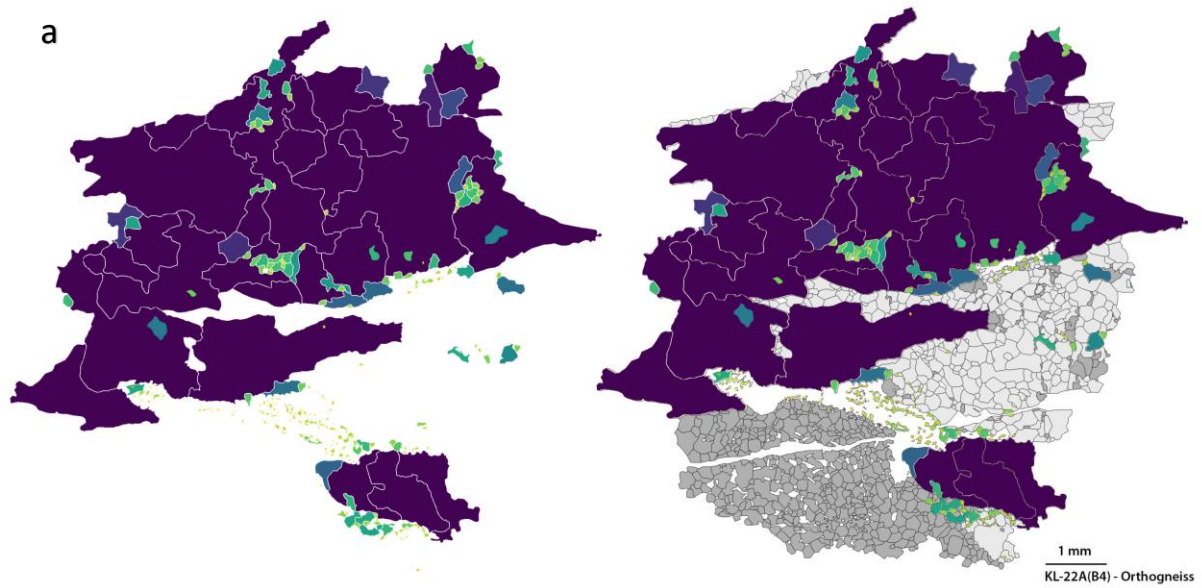
Grain size maps for plagioclase in appendix B show an increased tendency toward crystallization of interstitial feldspar grains in domains dominated by the complementary phases. There is also a gradual dismemberment of monomineralic aggregates as the evolution progresses from

microstructural type I to type IV. It is worth noting that smaller grain rarely appears together with larger grains of the same phase and that the grain size range of interstitial grains steadily increases toward larger sizes between microstructural type I and type IV (Appendix B K-feldspar-I to IV and Plagioclase-I to IV).

Quartz

Quartz shows the greatest range in grain size and, unlike for the feldspar grains, the range of outliers continuously decreases from type I to type IV (Figure 3.2-2). The greatest change in grain size occurs between the type I and type II microstructures where the IQR decreases dramatically and the median value is shifted toward smaller grain sizes (Figure 3.2-2). Quartz in both type I and type II orthogneisses has bimodal volumetric grain size distribution, there is however a general grain size reduction visible as lower fractions of grains larger than 0.6 mm and an increase proportion of small, 0-0.1 mm grains (Figure 3.2-3 c-I and c-II). Toward type III granofels, the range of IQR increases and it is slightly shifted toward larger grain sizes (Figure 3.2-2). Volumetrically, there is an increase in grains of medium size (0.2-0.5 mm) while there is a decrease in the proportion of large 0.5 mm grains from type II orthogneiss to type III granofels (Figure 3.2-3 C-II and c-III). Again, the grain size distribution changes in type IV granulite where the IQR decreases and the median is lowered (Figure 3.2-2). Compared to the grain size distribution of type III granofels, there is an increase in proportion of both small (0-0.1 mm) and middle sized (0.1-0.5 mm) grains while the proportion of grains larger than 0.5 decreases (Figure 3.2-3 c-III and c-IV). The volumetric grain size distribution of quartz in type IV granulite approaches a normal distribution, at least from 0-0.55 mm (Figure 3.2-3 c-IV). The grains that are larger than 0.55 are considered as outliers and relict of the initial aggregates.

Grain size maps for quartz (Figure 3.2-4) reveal an evolution similar to the feldspars. Quartz grains suffer from a major grain size reduction, increased proportion of interstitial grains within feldspar domains and a gradual break-up of the initial aggregate distribution throughout the microstructural evolution from type I to type IV (Figure 3.2-4 a-d). As with the feldspars, the size-range of interstitial quartz grains increases to include progressively larger sizes.



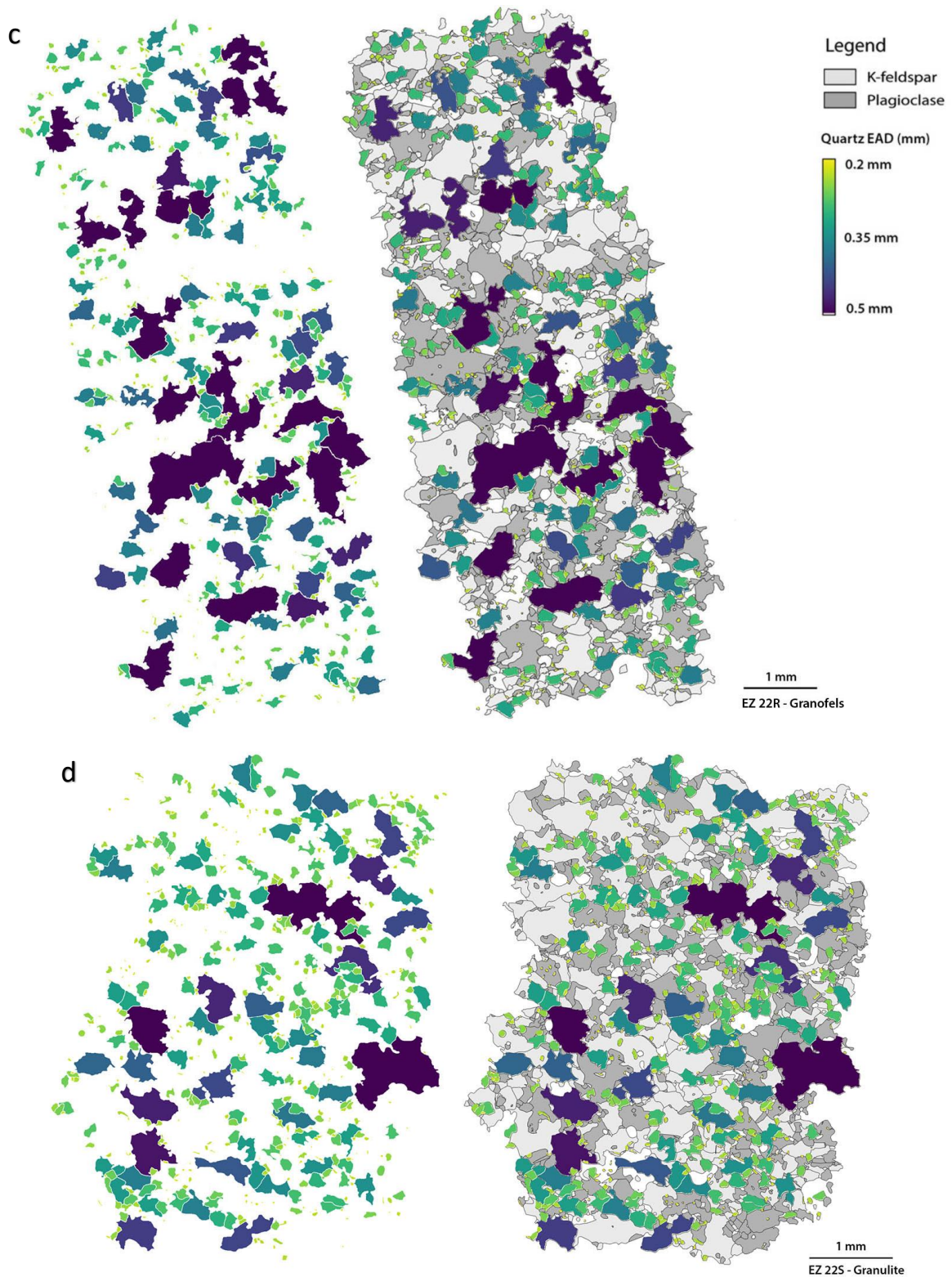


Figure 3.2-4 Grain size maps for quartz within the four microstructural types based on EAD. Within the grain size maps, all grains larger than 0.5 mm are coloured purple and all grains smaller than 0.2 mm are depicted in yellow, the intermediate range is coloured in the accordance with the colour ramp in the legend. On the left hand side of (a)-(d) the grain size map is presented and on the right-hand side the grain size map of quartz is overlaid onto a grain map of the complementary felsic phases. Grain size maps for **(a)** type I orthogneiss, **(b)** type II migmatitic orthogneiss, **(c)** type III granulite and **(d)** type IV granulite. Note that the colour coding process considers inclusions as being part of the host grain, which might have led to a slight overestimation of EAD of certain grains

3.2.3 Contact frequency

The grain contact frequency method established by [Kretz \(1969\)](#) is used to evaluate, to which extent the distribution of phases within the sample volume statistically deviates from a random distribution. In this work, grain contact frequencies for K-feldspar, plagioclase and quartz in all microstructural types were evaluated. The results of the evaluation are presented in Figure 3.2-6, where the χ -value represent the deviation from a random distribution plotted against types of intraphase (like-like) and interphase (unlike) grain contacts. The phases can be randomly distributed (Figure 3.2-5 b) throughout the sample volume, resulting in a χ -value between 1 and -1, or it can deviate in two ways, either; (1) toward an aggregate distribution (Figure 3.2-5 c) where intraphase contacts are predominate due to clustering of grains of the same phase or; (2) they can deviate toward a regular distribution (Figure 3.2-5 a) where interphase contact dominate as the phases occur in a chessboard-like fashion. When it comes to the χ -value, interphase and intraphase contacts mirror each other, meaning that a positive χ -value implies a deviation towards an aggregate distribution for intraphase contacts while a negative χ -value implies the same for interphase grain contacts. Since the contact frequency considers number of contacts and not their spatial orientations and length, it should be noted that interphase contacts in strongly anisotropic material can misleadingly point toward random distributions due to the large number of unlike phase contacts occurring along the borders of monomineralic bands.

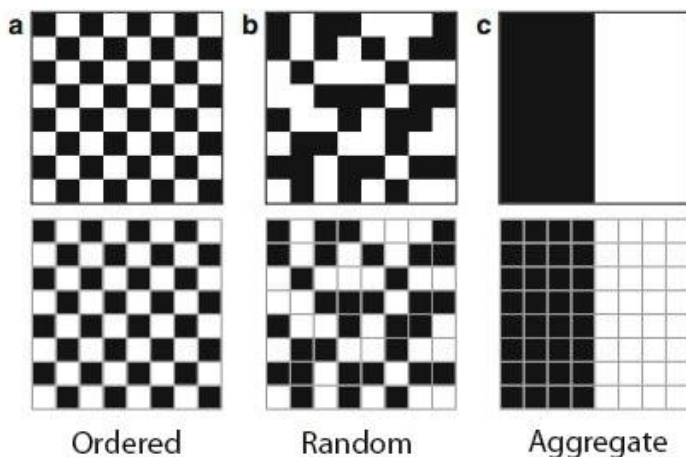


Figure 3.2-5 Model of spatial distribution of phases. Three types of distribution of a two-phase system is shown without (top) and with (bottom) boundaries. (a) A perfectly ordered distribution of phases; (b) a random distribution of phases and (c) a perfect aggregate distribution. Adapted after [Heilbronner et al. \(2010\)](#)

Type I microstructure represented by the orthogneiss is characterized by a large fraction of intraphase contacts compared to what is expected for a random distribution, hence indicating a strong aggregate distribution (Figure 3.2-6 a). The strongest maximum for interphase contacts is found in k-feldspar while the χ -value is drastically lower for plagioclase and lowest for quartz. The larger χ -value for K-feldspar, is attributed to that fact that K-feldspar appears as uninterrupted monomineralic aggregates, while both plagioclase and quartz exhibits slightly weaker aggregate

distributions. The slightly weaker aggregate distribution of plagioclase and quartz in this microstructural type is due to interstitial plagioclase and quartz being present in K-feldspar domains, elongate biotite grains separating plagioclase grains in plagioclase domains and a large amount of interstitial quartz associated with mica bands. The interphase phase contacts also lean toward an aggregate distribution for the type I orthogneiss, but to a lesser extent compared to the interphase contacts. Especially the K-feldspar-plagioclase and plagioclase-quartz contacts show strong evidence for aggregate distributions while K-feldspar-quartz contacts have an apparent random distribution of contacts. As K-feldspar and quartz domains are in continuous contact and the section through their contact surface offers a large number of individual K-feldspar-quartz grain contacts, it results in the observed number of contacts not being too different from the expected value, hence falsely indicating a random distribution of their contacts.

From the well-developed aggregate distribution in type I microstructure there is a dramatic change when moving toward the type II-IV microstructures as there is a clear evolutionary trend toward a regular distribution. Despite the strong macroscopic anisotropy in type II migmatitic orthogneiss, an aggregate distribution is not observed. On the contrary, the data reveal a random and weakly ordered distribution for K-feldspar and quartz intraphase contacts, respectively (Figure 3.2-6 b). The intraphase contacts of plagioclase still suggest a weaker aggregate distribution compared to K-feldspar and quartz. The reduction in aggregate-type contact frequency from type I orthogneiss to type II migmatitic orthogneiss is attributed to the large number of small grains of plagioclase, K-feldspar and quartz lining the outer boundaries of inherited aggregate domains as well as occurring as interstitial grains causing a separation of original K-feldspar and quartz intraphase contacts (Figure 3.2-6 a and b). From the type I orthogneiss to type IV granulite, the frequency of interphase contacts continually decreases while the frequency of intraphase contacts generally increases. K-feldspar and quartz have the strongest tendency to arrange in an ordered fashion in type III and type IV samples (Figure 3.2-6 c and d). Plagioclase exhibits a random distribution in type III and a weak ordered distribution in type IV microstructure (Figure 3.2-6 c and d).

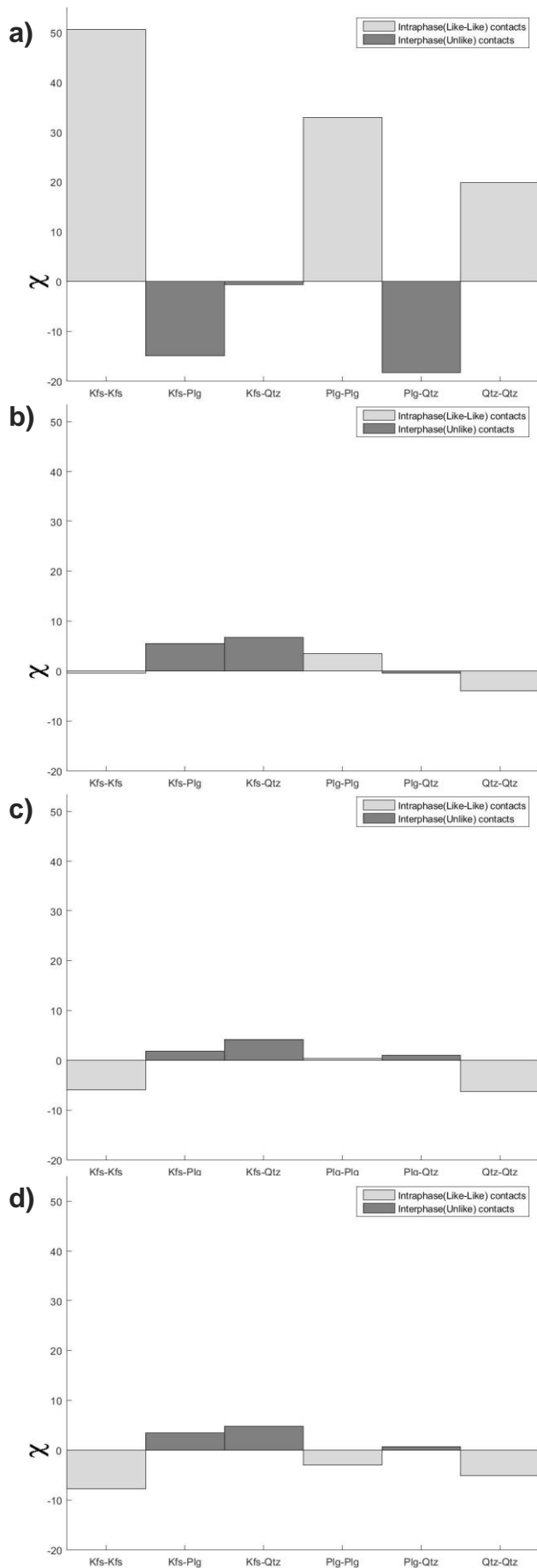


Figure 3.2-6 Grain boundary contact frequencies for **(a)** orthogneiss (type I), **(b)** migmatitic orthogneiss (type II), **(c)** granofels (type III) and **(d)** granulite (type IV). Grain boundary statistics for the four textural types plotted as the deviation from a random spatial distribution of phases where a positive χ points toward an aggregate arrangement for intraphase (like-like) contacts (opposite for interphase contacts) and a negative χ indicates an ordered arrangement for intraphase contacts (opposite for interphase contacts).

3.3 Results of EBSD analysis

Crystallographic-preferred orientation (CPO) measurements of K-feldspar, plagioclase and quartz were performed for the four microstructural types in order to determine if there is a relative change in fabric or fabric intensity. In this sub-chapter, results of EBSD-analysis of the four thin sections are presented in terms of point data opposed to grain data in order to enhance the existing fabric. Contoured pole figures shows the fabric intensity as multiples of uniform distribution (MUD) where the grey-levels of quartz and feldspars are set with respect to the global maxima of that specific phase. This was not done for biotite as one of the samples exhibits an extreme MUD value compared to biotite-data for the other samples.

3.3.1 Biotite

Within type I and II microstructure, a strong foliation is macroscopically defined by the parallel alignment of micas localized in narrow domains. For microstructural types III and IV the foliation is no longer macroscopically visible which complicates the procedure of making thin sections within equal reference planes. The thin sections used in this thesis represent XZ sections where both the foliation and lineation for type III granofels and type IV granulite have been inferred from their relation to banded gneisses within the outcrop. This method of deduction is however flawed if the outcrop is macroscopically or even microscopically folded. As a test of the accuracy of inferred orientations, CPO of biotite was measured as it is believed that biotite will define a relict foliation inherited from the banded gneisses in both the granofels and granulite.

EBSD data for biotite are presented in terms of poles to the basal plane ($\{001\}$) and orientation of the a and b axis represented by poles to the $\{100\}$ and $\{010\}$ planes, respectively. Pole figures of biotite basal planes show a well-defined foliation for microstructural types II-IV and random orientations of the a and b axis within the foliation plane (Figure 3.3-1 b-d). There is however, a limited number of sample points due to limited occurrences of biotite in the granulite sample, which results in one extreme maximum in the resulting pole figure. In type I orthogneiss, the foliation is clearly visible macroscopically, however, biotite CPO implies that the foliation lies in the XZ plane (Figure 3.3-1a). Closer microscopic investigation revealed that in some instances the micas seem to have enveloped recrystallized quartz and feldspar aggregates resulting in a variety of orientations deviating from the expected orientation parallel to the XY-plane. Unfortunately, the EBSD analysis of this sample was carried out in such an area, which might explain the surprising CPO of biotite in type I orthogneiss (Figure 3.3-1 a).

As results of the EBSD analysis show that biotite does in fact have strong CPOs for types II-IV, it was decided to rotate both the pole figures for these microstructural types into an orientation based on biotite CPOs instead of their inferred orientations from field outcrops. Because of the orientation-correction, the direction of the lineation in now unknown and is oriented in some direction within the XY plane. As the foliation in type I orthogneiss is clearly visible macro- and microscopically, the corresponding grain maps and pole figures were oriented with respect to the main microscopic orientation rather than biotite CPO data.

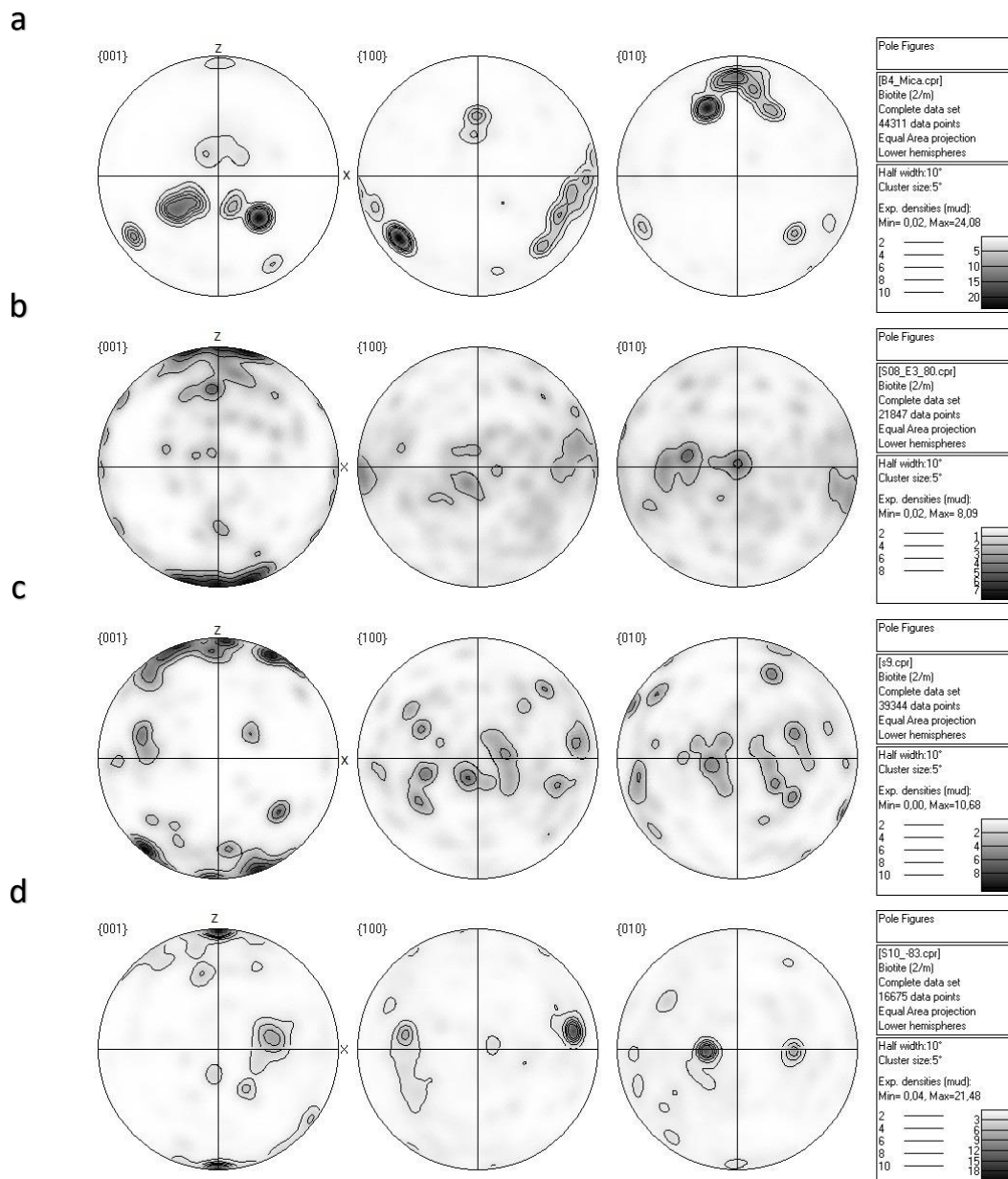


Figure 3.3-1 Biotite CPO data for (a) type I orthogneiss (b) type II migmatitic orthogneiss (c) type III granofels and (d) type IV granulite. Pole figures are contoured as multiple of uniform distribution, lower hemisphere, equal area projections. Z designates the direction of poles to the foliation while the lineation is oriented in some unknown direction within the XY plane.

3.3.2 Quartz

Quartz CPO is presented in terms of poles to the m -plane ($\{10\cdot10\}$), r -plane ($\{10\cdot11\}$) and orientation of the c -axis through poles to the basal plane ($\{0001\}$). Quartz in type I microstructure has a weakly defined clustered c -axis maximum which is indicative of a fabric (Figure 3.3-2a). For the microstructural types II-IV, quartz within the sampled area has a random CPO with scattered maxima of variable strength and orientations (Figure 3.3-2b-d).

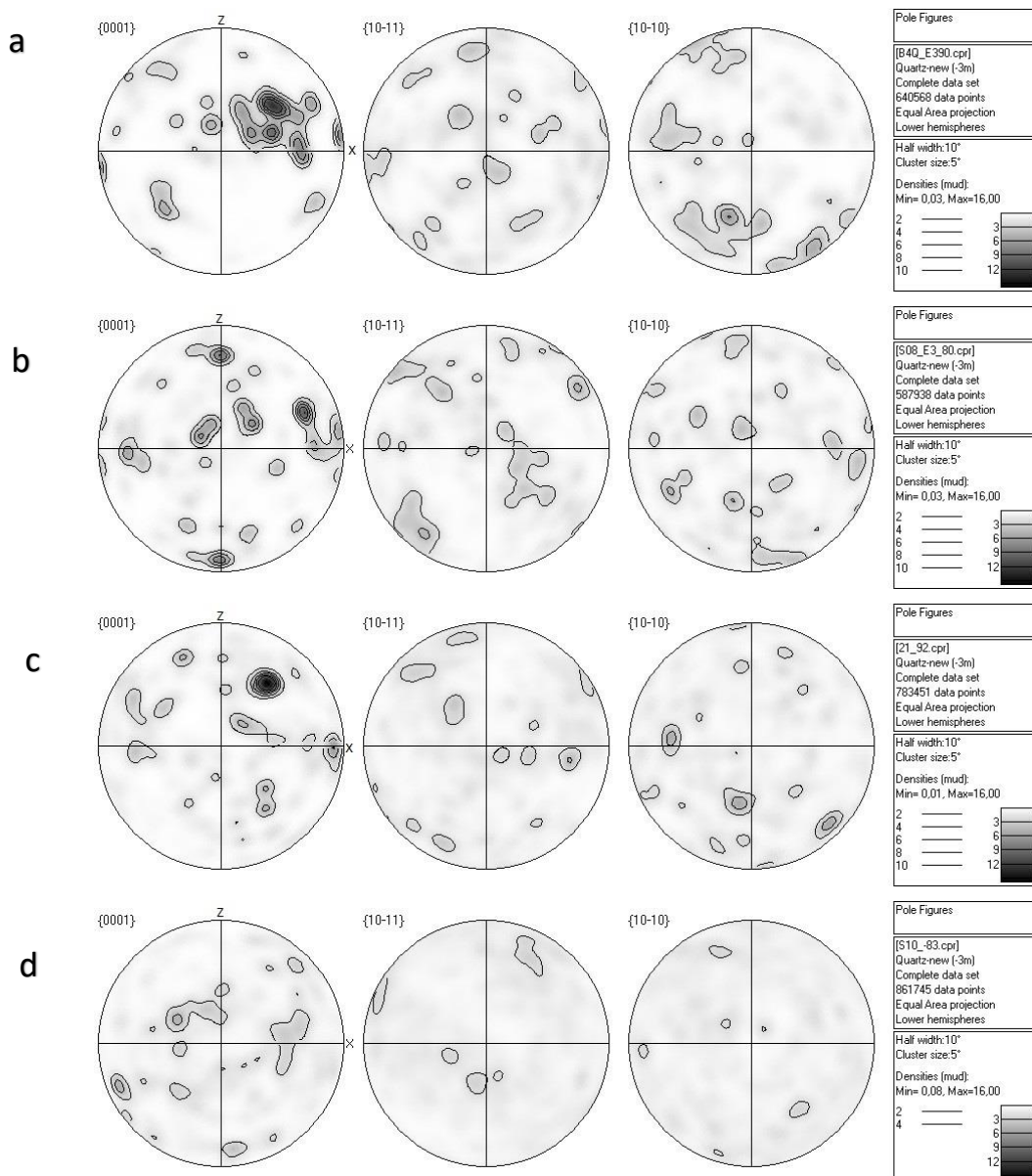


Figure 3.3-2 Quartz CPO data for (a) type I orthogneiss (b) type II migmatitic orthogneiss (c) type III granofels and (d) type IV granulite. The pole figures are contoured as multiple of uniform distribution, lower hemisphere, equal area projections coloured in accordance with observed global MUD maxima. Z designates the direction of poles to the foliation while the lineation is oriented in some unknown direction within the XY plane.

3.3.3 K-feldspar

EBSD results for K-feldspar is given in terms of orientations of poles to the {001}, {100} and {010} crystallographic planes. CPO data for K-feldspar in type I orthogneiss shows a defined CPO where the measured crystallographic planes exhibits smooth population maxima (Figure 3.3-3a). For types II-IV there is no preferred orientation of the evaluated K-feldspar data points (Figure 3.3-3b-d).

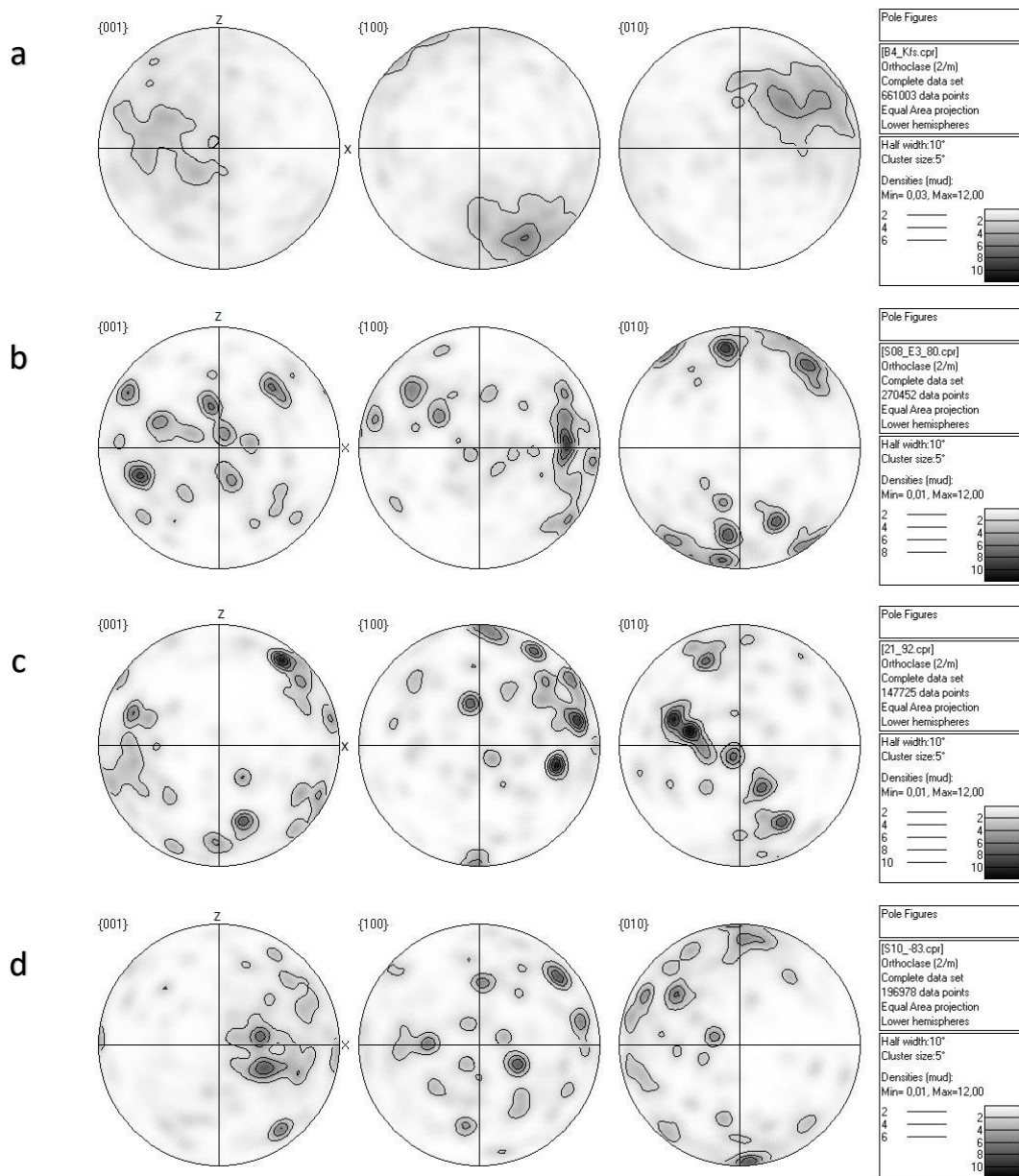


Figure 3.3-3 K-feldspar CPO data for (a) type I orthogneiss (b) type II migmatitic orthogneiss (c) type III granofels and (d) type IV granulite. Pole figures are contoured as multiple of uniform distribution, lower hemisphere, equal area projections colored in accordance with observed global MUD maxima. Z designates the direction of poles to the foliation while the lineation is oriented in some unknown direction within the XY plane.

3.3.4 Plagioclase

EBSD results for plagioclase is presented orientations of poles to the {001}, {100} and {010} crystallographic planes. Plagioclase in the four samples has an oligoclase composition, and albite yielded better solutions in the indexing of Kikuchi patterns compared to anorthite. As a consequence, the CPO of plagioclase is given in terms of albite solutions. The resulting pole figures shows that plagioclase within microstructural types I-IV have random CPOs (Figure 3.3-4a-d). The strength and isolation of maximums within the pole figures suggest that the sample size was not large enough.

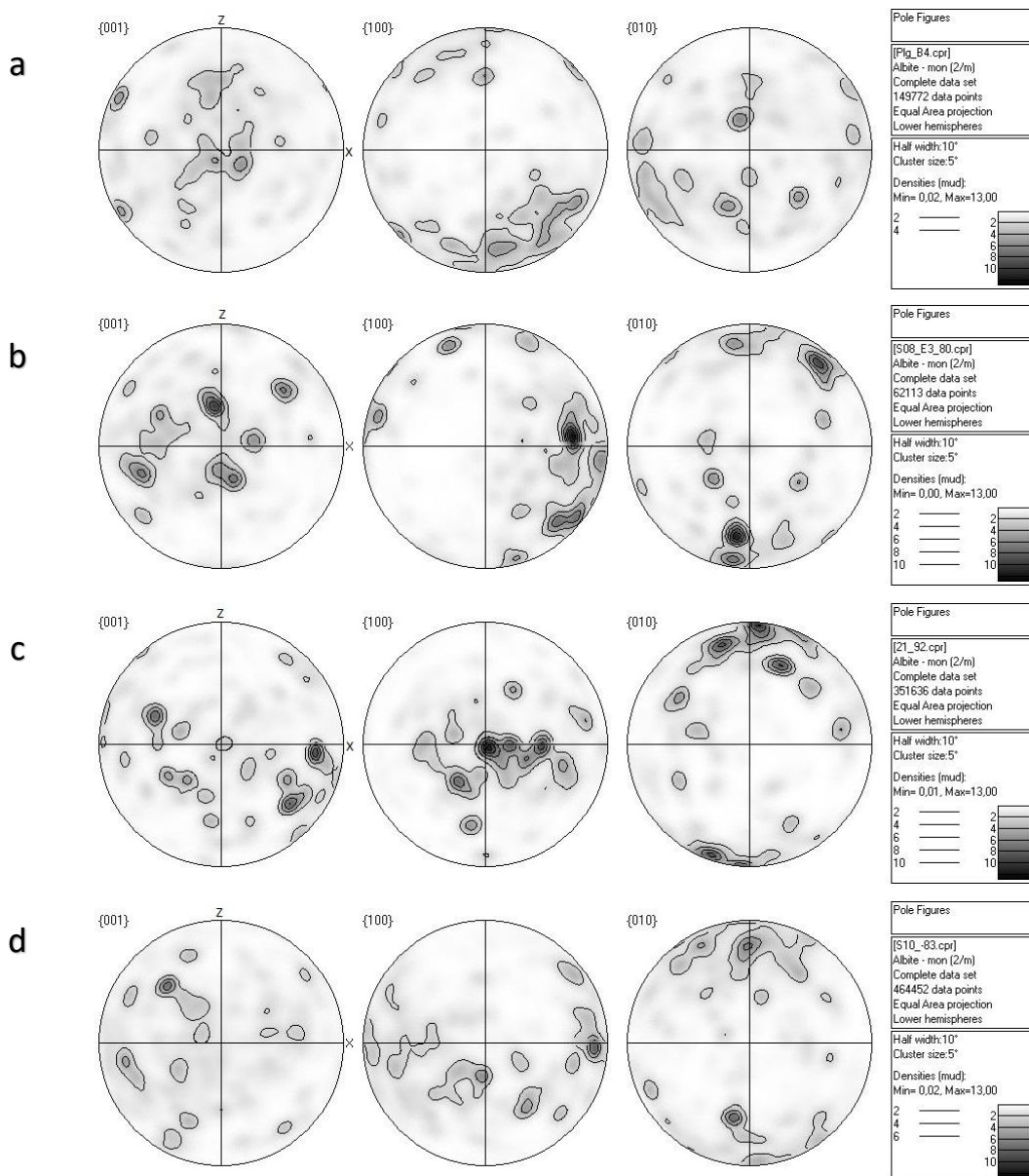


Figure 3.3-4 Albite CPO data for **(a)** type I orthogneiss **(b)** type II migmatitic orthogneiss **(c)** type III granofels and **(d)** type IV granulite. Pole figures are contoured as multiple of uniform distribution, lower hemisphere, equal area projections colored in accordance with observed global MUD maxima. Z designates the direction of poles to the foliation while the lineation is oriented in some unknown direction within the XY plane.

4 Discussion

Results of the quantitative microstructural analysis, supported by macroscopic and microscopic observations reveals an evolutionary trend from a strongly anisotropic orthogneiss (type I), migmatitic orthogneiss (type II) and granofels (type III) to the well-equilibrated granulite (type IV). In this chapter the interpretations of the results are discussed, starting with quantitative observations and previously established facts before interpretations of the quantitative results are given. Lastly, hypotheses concerning the microstructural evolution are discussed.

4.1 Interpretation of qualitative observations

4.1.1 Solid state deformation

Peak metamorphic conditions were estimated at 9.5 kbar and 700 ± 20 °C for partially molten orthogneiss ([Závada et al., 2007](#)), ~750 to 770 °C and ~14-16 kbar for the granofels and ~820 to 860 °C and ~14-16.5 kbar for the granulite ([Konopásek et al., 2014](#)). Peak metamorphic conditions are sufficient for dynamic recrystallization of quartz and both feldspars that represent the main mineral phases in the studied quartzofeldspathic. Within this range of temperatures, feldspars and quartz dynamically recrystallize through different processes. Quartz tends to recrystallize through grain boundary migration and resulting the microstructure will show lobate intraphase boundaries and pinning structures. Feldspars will recrystallize through both bulging and subgrain rotation resulting in either core and mantle structures, or if deformed at higher strains, completely recrystallized aggregates ([Passchier et al., 2005](#)). Deformation induced myrmekites are also common within this temperature range ([Simpson and Wintsch, 1989](#)).

Quartz in type I orthogneiss exhibits sweeping undulose extinction which is taken as evidence of intracrystalline plasticity, however this may be a later feature. Highly interlocking intraphase boundaries in quartz (Figure 3.1-2b) also suggest that dynamic recrystallization was active through high-temperature grain boundary migration. Feldspars within this sample form polygonal fabric with straight grain boundaries, numerous 120° triple junctions and with individual grains showing little evidence of solid state deformation which suggest that recovery and annealing kept up with the deformation. In microstructural types II-IV, evidence of solid-state deformation is scarce and limited to few occurrences of sweeping undulose extinction in larger quartz grains. Type II-IV samples do contain myrmekite, but this feature is not diagnostic of solid state deformation as it can also directly result from melt crystallization or melt-solid reaction ([Hibbard, 1979](#), [Vernon, 1991](#)).

4.1.2 Evidence of melting

[Konopásek et al. \(2014\)](#) found that the orthogneisses of the Eger complex equilibrated within the melt stability field, but the amount of the melt phase did not exceed ~4 wt% at the metamorphic peak, which is consistent with the previous calculations by [Závada et al. \(2007\)](#). Toward the granulite, the melt fraction melt increases to ~5.5 to 8.5 wt%. Muscovite and biotite initially appear as euhedral grains in type I and becomes increasingly more corroded toward type IV granulite, where the muscovite is eliminated from the mineral assemblage. Intergrowths of quartz with muscovite (Figure 3.1-6 a) which is present type II to type III and increasingly corroded biotite grains from type II to type IV suggests dehydration melting of muscovite and later biotite. This is supported by the generalized melt-producing reactions proposed by [Závada et al. \(2007\)](#) ($Bt + Ms + Plg + Qtz = Grt + Kfs + melt$ for the orthogneisses) and [Konopásek et al. \(2014\)](#) ($Ms + Bt + Plg + Ilm + Qtz = Grt + Kfs + Ky + Rt + melt$ for the transition from amphibolite to granulite facies).

In this work K-feldspar, plagioclase and quartz occurring as elongated grains along grain boundaries and as cusped interstitial grains is taken as microstructural evidence of the former existence of melt in types I and II (Figure 3.1-2a). Interstitial grains of K-feldspar, plagioclase and quartz are rarely present within aggregates dominated by the same phase (i.e interstitial K-feldspar in K-feldspar aggregate etc.), indicating that either; (1) such nucleation is unfavoured or; (2) that the crystallization of the particular phase is realized as an addition to existing grains. In types III and IV, inferring melt presence becomes more problematic as the phases are largely intermixed. Reactant minerals become progressively more corroded and embayed, probably as the melt fraction increases. Indentations and corrosion of relict grains (Figure 3.1-6 b and Figure 3.1-8) in microstructural types III and IV can be taken as evidence of former melt presence ([Sawyer et al., 1999](#), [Sawyer, 2001](#)). It should be noted that the above mentioned microstructural evidence is indicative but not conclusive evidence of melt presence. Previous thermodynamic modelling of the studied microstructural types supports the argument of melt presence. Macroscopic evidence of melt is limited to observations suggesting that melt has crystallized within shear bands. Both macroscopic and microscopic observations along with thermodynamic modelling suggest that all the microstructural types have equilibrated in the presence of melt, and the degree of interaction between the host rock and melt increases throughout the studied evolutionary set of samples.

4.1.3 Static recrystallization

Static recrystallization (or annealing) operates in the absence of deformation either after deformation has ceased or during passive heating of previously deformed material (i.e [Passchier et](#)

[al., 2005](#)). The process is driven by reduction of surface energy and grain boundary area reduction is considered as the primary mechanism of this type of recrystallization. Static recrystallization is more effective when assisted by a fluid phase and generally leads to grain coarsening at high temperatures ([Higgins, 2006](#)). Evidence of extensive static recrystallization involving grain boundary area reduction includes the development of mosaics of polygonal grains and the presence of straight grain boundaries meeting in 120° triple junctions ([Passchier et al., 2005](#)). In rocks that are not completely recrystallized, straight and gently curved intraphase boundaries may be taken as an indicator of static recrystallizing activity.

In type I orthogneiss, monomineralic bands of K-feldspar and plagioclase form polygonal mosaics of grains with very straight intraphase boundaries (Figure 3.1-2 d and e), which is taken as evidence that static recrystallization took place in the sample. Quartz boundaries have interlocking boundaries, which forms straight zig-zagging segments (Figure 3.1-2 b) considered as an annealed quartz fabric ([Kruhl and Peterneil, 2002](#)).

In microstructural types II-IV, intraphase boundaries of K-feldspar and plagioclase remain straight or gently curved, which might be a feature from the stage when the samples still had unmodified type I microstructure. The nature of quartz intraphase boundaries changes from interlocking boundaries to straight and gently curved from type I to types II-IV, suggesting that the samples may have been further statically recrystallized through grain boundary area reduction. Interphase boundaries are highly lobate which may be attributed to the presence of 2nd phase grains which may pin and block grain coarsening ([Higgins, 2006](#)).

4.2 Interpretation of quantitative statistical results

4.2.1 Interpretation of grain size

Grain growth involves the uniform increase in average grain size and according to kinetic theory, grains smaller than the mean grain size will become smaller while grains larger than the mean size will grow larger ([Kretz, 1994](#)). The growth rate of grains is inversely proportional, meaning that grains just above the critical radius will have the fastest growth while an infinitely large grain will have a growth rate of zero. In monomineralic aggregates, this coarsening is driven by reduction of grain surface energy mainly through grain boundary mobility. In melt-bearing systems, material from grains smaller than the critical size may be transferred by diffusion ([Higgins, 1998](#)). Reduction of mean grain size is commonly associated with dynamic recrystallization, the same can be achieved through nucleation of mineral phases from melt.

The overall trend in the four investigated microstructural types involves a consistent oscillation of the median grain size for K-feldspar, plagioclase and quartz. From type I to type II the median grain size for these phases drops significantly while there is an overall increase in the median value toward the type III granofels, especially in the case of K-feldspar. In the type IV granulite, the median grain size is again lowered.

In the type I microstructure, fast grain boundary migration resulted in a large grain size within quartz aggregates, which together with the presence of small interstitial grains of quartz within K-feldspar- and mica-rich domains leads to a large spread in grain size and a bimodal distribution. Partial dynamic recrystallization through bulging or subgrain rotation typically leads to bimodal distributions and as the grain sizes for the feldspars are unimodal, it suggests that the feldspars have been completely dynamically recrystallized. However, since the feldspars have clearly undergone static recrystallization in terms of grain boundary area reduction, it is not possible to make detailed interpretation of their syn-deformational grain size development.

Inspection of volumetric grain size distributions shows that from type I to type II microstructure there is a change from normal to bimodal distribution in feldspars, while both microstructures show a bimodal distribution for quartz (Figure 3.2-3 I and II). Toward type II microstructure, the change in grain size distribution of both feldspars is caused by an increased proportion of smaller grains and reduced proportion of mid-ranged grains outweighing an increased proportion of larger grains. This suggest that the grain size development is dominated by nucleation, but that some grain growth was active too.

In type III granofels the proportion of smaller grains decreases, while there is an increasing proportion of larger grains for both feldspars (Figure 3.2-3 a-II and a-III, and b-II and b-III). This suggest a pure ripening of the microstructure which is most prominent in K-feldspar and may be linked to the lack of dissolution of the existing K-feldspar during the melting reaction. In quartz, the mid-range grain sizes increases while the proportion of larger grains decreases for this microstructural type (Figure 3.2-3 c-II and c-III). As with the feldspars, the median value and the IQR of the EAD increases for quartz (Table 3.2-2 and Figure 3.2-2). This implies that the increased proportion of medium-range grain sizes out-power the effect of loss of large grains and increased proportion of smaller grains observed in the volumetric quartz size distribution (Figure 3.2-3 c-II and c-III). Together, the grain size statistics for feldspar and quartz points to a simultaneous interplay between nucleation and grain growth, where the growth is more effective for medium grain sizes.

Type IV granulite shows a consistent median grain size for all phases, and is otherwise characterized by increased proportion of smaller grains and a general decrease in the proportion of larger grain sizes (Table 3.2-2 and Figure 3.2-3 IV). In this microstructural type, the grain size ranges for both plagioclase and quartz decrease and while the plagioclase distribution is without any well-defined peaks it seems like quartz is approaching a perfect bell-shaped, i.e. normal grain size distribution. K-feldspar however, does not exhibit narrowing of the grain size range and seems to show a random distribution (Figure 3.2-2 and Figure 3.2-3 a-IV). Throughout the microstructural evolution, the grain sizes of quartz and plagioclase have evolved through an interplay between melting, nucleation and growth. In type IV granulite, the evolution of the grain size suggests that there has been a re-equilibration of the grain size which is now approaching a normal distribution for plagioclase and especially in the case of quartz (Figure 3.2-3 b-IV and c-IV).

Grain size reductions are most often attributed to dynamic recrystallization in terms of bulging and subgrain rotation. In such a case, the grain size reduction is consistent in both feldspars and quartz, which recrystallize through different mechanism within the estimated temperature range and along with arguments made in section 4.1.1, mechanisms of dynamic recrystallization can be excluded as a source of the observed reductions in grain size. It has already been established that the investigated microstructural types equilibrated within the melt stability field, so the grain size reduction from type I orthogneiss to type II migmatitic orthogneiss is interpreted as being a result of melt crystallization along high-energy grain boundaries and triple junctions. From type II migmatitic orthogneiss to type III orthogneiss there is a coarsening of the feldspar grain size, where larger grains have grown at the expense of smaller grains. This process is often referred to as Oswald ripening when involving solid or liquid solution and in this case, high-energy small crystals are likely dissolved in partial-melt network along grain boundaries and subsequently re-precipitated as an addition to larger grains ([McLellan, 1983](#)). The ripening process is most evident in K-feldspar, which is interpreted as an effect of the fact, that no pre-existing K-feldspar is consumed during the melt-producing reaction. In quartz, the grain size suggests that the processes of nucleation, growth and melting are competing, and an overall ripening cannot be inferred for quartz.

4.2.2 Interpretation of spatial distribution of phases

A random spatial distribution of minerals is considered as a result of random nucleation and growth from an isotropic medium (i.e melt or fluid) preserved through rapid cooling in the case of nucleation from melt ([McLellan, 1983](#)). Aggregate distribution on the other hand, develops through coalescence of like-phases under solid-state differentiation at high strains, where the solid state differentiation is

mostly associated with dynamic recrystallization ([Schulmann et al., 1996](#), [Kruse and Stünitz, 1999](#), [Lexa et al., 2005](#)). [Flinn \(1969\)](#) explained the regular distributions of minerals in granulites as a result of equilibration of the rock through minimization of interfacial energy, recording the disappearance of high-energy intraphase contacts and an increase in low-energy interphase contacts. More specifically he suggested that redistribution of grains, favouring insertion of interphase phases between like phases lowers the interfacial energy of the rock and causes the minerals to be distributed in an ordered fashion. Generally, an ordered distribution can be predicted for rocks that have undergone considerable solid-state annealing, i.e. most high grade metamorphic rocks ([McLellan, 1983](#)).

Quantitative statistical analysis of spatial distribution of K-feldspar, plagioclase and quartz shows a progressive change from a strong aggregate distribution toward a regular distribution of phases, which is in agreement with an increasing degree of microstructural equilibrium between the host rock and the melt phase. Melt crystallization leads to new mineral growth along the high-energy interphase boundaries of pre-existing grains, resulting in an increasing frequency of interphase contacts as the crystallization process proceeds ([Hasalová et al., 2008](#)). The spatial evolution of feldspars and quartz from type I orthogneiss to type IV granulite is consistent with crystallization of a minor phase in triple junctions and along grain interphase boundaries. A feature that was documented by [Dallain et al. \(1999\)](#) who found that in polycrystalline aggregates, the predominance of interphase phase contacts was a result of grain boundary wetting by fluids or melts and subsequent precipitation of other phases along intraphase boundaries. Modern experiments within the field of material science also found that boundaries with a low misorientation angle within a single-phase aggregate are preserved during grain boundary wetting, while a second phase will tend to precipitate on boundaries with high misorientation angles. Thus continuously eliminating high energy boundaries from the inherited microstructure by infiltration of another phase ([Kim and Rohrer, 2004](#), [Lexa et al., 2005](#)).

The development of the spatial distribution from a strong aggregate arrangement exhibited by type I orthogneiss toward a regular distribution observed in the type IV granulite sample is driven by melt crystallization and solid-state annealing. A regular distribution is considered to be the energetically lowest state of this type of polymineralic material ([Devore, 1959](#)), and it is believed that melt crystallization will to some extent follow the principle of surface energy reduction through elimination of high-energy boundaries (commonly non-coherent intraphase contacts) as documented by [Dallain et al. \(1999\)](#) and [Kim and Rohrer \(2004\)](#). Even though melt crystallization is inferred as the primary mechanism for the continuous elimination of high energy boundaries from type I to type IV,

contribution from solid state annealing which is commonly active in high-grade rocks cannot be excluded.

4.2.3 Interpretation of EBSD-results

The isolated and sometimes extreme maxima in the CPO data suggest the sample area hasn't been sufficiently large. Ideally one should have smooth population maxima like that of K-feldspar in Figure 3.3-3 if there is a CPO present, and scattered low value maxima if the CPO is absent. The results of the CPO analysis do not allow for in-depth interpretations; however, some general assumptions can be made.

Although both biotite and muscovite breaks down through the melt producing reaction, there is a much higher proportion of muscovite entering the melt relative to biotite. Compared to biotite there is limited solid solution in muscovite, resulting in a virtually univariant melting of muscovite while the biotite is more persistent throughout the evolution and hence retaining the orientation of a relict foliation ([Gardien et al., 1995](#)). As a result the CPO of biotite can be used to reconstruct the foliation of samples where the foliation is not macro- or microscopically visible (see also section 3.3.1).

Quartz and K-feldspar exhibit a weak CPO in the type I orthogneiss, but such preferred orientation is lacking in microstructural types II-IV. The CPO of K-feldspar and quartz in type I microstructure along with sweeping undulose extinction in quartz indicates some degree of intracrystalline deformation. As the CPO is absent in types II-IV, it strongly suggests that a CPO-weakening mechanism or process has operated between the microstructural stage I and II. This lack of CPO in rock-types II-IV could reflect alteration of the deformation-related CPO as a result of static recrystallization post-dating the main deformation event ([Green, 1967](#)). Recent studies on quartz CPO patterns in naturally and experimentally deformed rocks show that static recrystallization had little impact on CPO patterns even after extensive annealing ([Heilbronner and Tullis, 2002](#), [Otani and Wallis, 2006](#)).

Diffusion creep-accommodated grain boundary sliding is considered as a deformation mechanism that hinders the development of a CPO and possibly destroys pre-existing CPOs ([Jiang et al., 2000](#)). However, the lack or weak CPO in types II-IV cannot be considered as conclusive evidence of GBS nor can it be ruled out as a possible contributing mechanism in any of the microstructural types based on the available CPO data. As it has been already shown that the investigated microstructures in type II-IV samples involve melt crystallization, it seems that the most plausible explanation for the observed CPO weakening is related to the increasing amount of new grains inferred to be melt crystallization products. In this respect, it is inferred that there are at least two distinct grain generations within the

types II-IV microstructures: (1) An older grain generation generally consisting of larger grains with inherited features resulting from high-temperature solid-state deformation; and (2) a younger generation of smaller grains devoid of intracrystalline deformation that have a random CPO consistent with melt crystallization. As the volume of newly crystallized grains increases, the inherited CPO of the older grain generation will be inferior resulting in a weakening of the observed CPO. The lack of development or enhancement of a pre-existing CPO suggest that the observed microstructural changes take place under static conditions.

4.3 Interpretation of chemical changes in minerals

Microprobe analysis of the minerals in the type III granofels and type IV granulite along with existing analyses of minerals in the type I orthogneiss have shown that the X_{Fe} -values of garnet and biotite increase slightly from type I to type III and that these values significantly decrease in the granulite. This effect is especially seen in garnet while the X_{Fe} of biotite is more stable. Plagioclase composition also seems to be relatively stable throughout the evolution with no real change in the anorthite component. Experimental studies and field observations suggest that in the case of partial melting, plagioclase composition tends to show increased proportions of the anorthite component and that the X_{Fe} -value of garnet and biotite would decrease ([Breton and Thompson, 1988](#), [Vielzeuf and Holloway, 1988](#), [Dallain et al., 1999](#)).

Albite rims in plagioclase along certain contact surfaces with K-feldspar in granitic rocks have been the subject of many studies, and there are several explanations of their origin. The most probable explanation is un-mixing of the albite component from adjacent K-feldspar grain and its nucleation on adjacent plagioclase or in form perthite ([Ramberg, 1962](#)).

4.4 Origin of evolutionary sequence

The investigated rock types represent a sequence of four microstructural stages from a banded orthogneiss to a granoblastic granulite. As suggested by [Hasalová et al. \(2008\)](#) the possible origin of similar sequences can be driven by; (1) an increasing degree of one-step *in situ* partial melting; (2) melt infiltration from an external source; or (3) the sequence can be comprised of genetically unrelated migmatitic rocks evolved from distinctly separate protoliths. Additionally, the possibility of; (4) melt infiltration from a local source will be discussed.

Independent evolution from distinct protoliths?

Observations of field outcrops suggest that the microstructural sequence is intimately linked as the transitions from banded orthogneisses to granulites are continuous both in outcrop and hand specimen scale. Figure 1.1-1 **Error! Reference source not found.** shows how this progressive transition takes place on a cm scale. [Konopásek et al. \(2014\)](#) showed that the whole rock chemistry and mineral chemistry is consistent throughout the microstructural types, the only exception being the granulite. Here one should keep in mind that the granulite equilibrated at considerably higher temperature compared to the orthogneisses and granofels. Both field observations and rock chemistry strongly suggest that the microstructural sequence did in fact evolve from the same protolith. It should be noted that before anatexis the gneisses underwent solid-state deformation at variable intensity which resulted in a gneiss variability from mylonites with perfectly parallel foliation planes to less deformed gneisses where the foliation is not as well defined ([Závada et al., 2007](#)). The difference between the CPO of biotite in type I orthogneiss and in microstructural types II to IV might be explained by such variability in gneissic protoliths. More specifically, it is possible that the gneissic protolith of types II-IV underwent strains than the type I orthogneiss as the biotite CPO is stronger in types II-IV. The mentioned interpretation is only one of several possibilities that might account for the opposing biotite CPOs. As a conclusion, the investigated samples evolved from the same protholith which may have had various intensity of solid-state deformation prior to the partial melting.

Model of *in situ* one-step melting

The mineral chemistry remains relatively stable for the microstructural types I and III. The significant drop in X_{Fe} of both garnet and biotite within the granulite sample is consistent with changes in mineral assemblage (i.e muscovite is absent and kyanite is present). This change in mineral assemblage must be associated with an increased proportion of melt compared to microstructural types I-III due the more intensive dehydration melting of biotite and especially muscovite.

The thermodynamic modelling suggests the presence of ~0-4 wt% melt for the orthogneiss and granofels while ~5.5 to 8.5 wt% melt is present in the granulite ([Závada et al., 2007](#), [Konopásek et al., 2014](#)). From type I to type II microstructure there is a relative increase in the smallest grain size fraction (0-0.1 mm for feldspars) which roughly amounts to 10 vol % in the case of K-feldspar and plagioclase (Figure 3.2-3 a-I to a-II and b-I to b-II). The small grains responsible for the increase is interpreted as being newly crystallized from the melt. The relative increase of ~ 10 vol % only represents the crystallized silicate fraction of the melt that additionally must have contained a high proportion of water. The presented data suggest that the amount of newly nucleated grains is

incompatible with predicted proportion of ~0-4 wt% in-situ melt in the orthogneisses and granulites. However, the thermodynamic modelling shows that some *in-situ* partial melting has occurred and likely contributed to the disintegration of the initial fabric.

Melt infiltration model

The thermodynamic modelling suggests a low melt fraction in the studied samples, which is insufficient to completely destruct the compositional banding and so the melt has to come from another source, either local or external. In this model, melt infiltrates the rock volume through pulses or pervasive percolation along grain boundaries effectively changing the macroscopic and microscopic appearance of the infiltrated rock. This process would progressively deconstruct relict aggregates as melt wets and eventually heterogeneously crystallize on high-energy intraphase boundaries. This model would also be accompanied by a grain size reduction due to the increased proportion of small, newly crystallized grains and a decreased CPO, all of which are consistent with what is macroscopically and microstructurally observed in the rock.

A possible explanation for the evolutionary trends recognized in the quantitative analysis involves melt infiltration from an external source. If this is the case, then one would expect a progressive change in whole rock composition and mineral chemistry, but only if the source of the melt is sufficiently contrasting and the amount of infiltrating melt is large. If the infiltrating melt and the host rock are similar in composition, then the distinction between melt infiltration from an external and local source becomes problematic.

When the melt infiltrates the rock from a local source, chemical changes are often negligible because the melt is in equilibrium with its source rock. In our case, the whole rock compositions and mineral chemistries remain constant, except for decreased X_{Fe} values for garnet and biotite in the granulite which relates to the metamorphic changes taking place. As the melting occurred through dehydration melting of muscovite and biotite, the melting was largely confined to mica bands, which were the source of melt for a potential local melt infiltration scenario. The melt originating within the mica bands might have been redistributed on a local scale due to a variety of factors including melt overpressure, pressure gradients and buoyancy. As the melt flowed through the rock and crystallized, the released fluid could have facilitated new partial melting of the rock. Such cyclic process of melting and melt crystallization could explain an apparently higher melt proportion than inferred from the thermodynamic modelling and could lead to the observed fabric disintegration.

The model of local melt infiltration might be appropriate model for the observed microstructural evolution as the mica rich domains in types I and II contain many interstitial grains, which are inferred to crystallize from melt. Based on the analysis presented in this thesis, the model of melt infiltration seems to be best explain the observed results. Melt infiltration from a compositionally different external source can be excluded based on the overall homogenous rock chemistry. As no clear distinction can be made between local infiltration and external infiltration of an indistinguishable source, neither local or external melt infiltration can be excluded as the primary contributor to the microstructural change. However, the model of cyclic melt infiltration from a local source is may be more plausible than cyclic melt infiltration from a compositionally similar, external source.

4.5 Evolutionary model

The original microstructure of the type I orthogneiss before anataxis and annealing is marked by a solid-state fabric consisting of alternating monomineralic bands of recrystallized K-feldspar, plagioclase and quartz discretely separated by layers rich in micas and garnet. Deformation microstructures in quartz, the presence of segregated monomineralic aggregates and CPO results for feldspar and quartz are consistent with high temperature deformation of a granite ([Schulmann et al., 1996](#)). The initial fabric is progressively converted into a polymineralic granoblastic microstructure represented by the type IV granulite. The grain size decrease from type I orthogneiss to type II migmatitic orthogneiss, as well as the transition from a CPO to a randomized texture and the change from an aggregate distribution toward an ordered distribution, suggests that the evolution is dominantly driven by crystallization of new grains along high-energy contacts. Further, there is a ripening of the microstructure observed in type III granofels where grain coarsening is dominant. Grain size statistics for quartz in this microstructural stage suggests that some nucleation is also taking place, this is supported by the decreased contact frequencies of interphase boundaries. Together the available data for this microstructural stage point to an evolution dominated by annealing processes and some degree of continued melt crystallization. Quantitative grain size statistics for type IV granulite suggests nucleation of new grains, development of a regular spatial distribution and decreased X_{Fe} of biotite and garnet related to metamorphic changes and an increased melt proportion. The presented data suggest that, in the final microstructural stage the increase in temperature leads to increased melting. The increased melt proportion in the final microstructural stage contributes to an almost complete disintegration of relict aggregates and the formation of a new relatively homogenous and equidimensional mosaic of grains.

5 Conclusions

Based on field and microstructural study, four microstructural stages are distinguished in metamorphosed quartzofeldspathic rocks in the Eger Complex: (1) Orthogneiss (type I) characterized by recrystallized monomineralic layers of K-feldspar, plagioclase and quartz discretely separated by layers rich in micas; (2) Migmatitic orthogneiss (type II) composed of K-feldspar-, plagioclase- and quartz-rich domains with diffuse boundaries and numerous small interstitial grains; (3) granofels (type III) comprised of intermixed domains, locally enriched in K-feldspar, plagioclase and quartz where the foliation is not visible microscopically; (4) Granulite (type IV) with a homogenous microstructure, with no relicts of the initial gneissic fabric. Detailed microstructural analysis of the microstructural sequence of samples demonstrates that the monomineralic banding produced through high temperature solid-state deformation of a granite is, with increasing temperature under static conditions, is progressively transformed into a polymineralic ordered microstructure of K-feldspar, plagioclase and quartz. In the early stage of the microstructural evolution, the median grain size generally decreases for all felsic phases due to nucleation of new grains from the melt, preferably along high-energy intraphase boundaries, which leads to the development of a regular spatial distribution of felsic phases. There is a considerable ripening of the microstructure before the final breakdown of muscovite at the granulite facies conditions, which again promotes nucleation and melt crystallization. In addition, previously developed solid-state crystallographic preferred orientation is destroyed from type I to type II microstructure. It is proposed that the progressive transformation is mainly driven by melt crystallization along high energy intraphase contacts and triple junctions, resulting in a progressive disruption of monomineralic aggregates. As it seems unlikely that the low melt proportion suggested by thermodynamic modelling is sufficient to completely re-equilibrate the rock fabric, a model of melt infiltration is proposed. The model involves a periodic influx of melt either from a local source or from an external source with the same composition. The melt infiltration would result in a stepwise disintegration and re-equilibration of the initial gneissic fabric which is now approaching a normal distribution, at least for quartz.

6 Acknowledgements

First, I would like to thank my amazingly patient supervisor Jiří Konopásek for always taking his time to answer my questions. Thank you for providing excellent guidance throughout the work of this thesis, your help has been completely essential. A sincere thanks goes to my co-supervisor Petr Jeřábek for teaching me the basics of Matlab™ and PolyLX programing and for his guidance and advice during my traineeship in Prague. I would also like to thank my other co-supervisors, Renée Heilbronner and Holger Stünitz for sharing their expertise. To Kai Neufeld, Prokop Závada, Martin Racek and the staff at the lab at the Institute of geosciences in Tromsø, thank you for all your help and assistance.

Mange takk til hyggelige medstudenter og til Ane for hyggelig stemning på kontoret. Det å kunne dele frustrasjonen med deg har gjort dette året levelig! Tusen takk til alle venner fjern og nær og ikke minst til min familie for all oppmuntring og støtte gjennom dette året.

Og til Martin, tusen takk for at du har holdt ut med meg gjennom alle opp- og nedturene det siste året!

A handwritten signature in black ink, reading "Kristine Hafne". The signature is written in a cursive, flowing style.

Kristine Hafne

Tromsø, May 2017

Works cited

- AUSTRALIAN MICROSCOPY & MICROANALYSIS RESEARCH FACILITY. 2014. *Generating an image* [Online]. Available: <http://www.ammrf.org.au/myscope/sem/practice/principles/imagegeneration.php> [Accessed 11.03.2017].
- BASEL UNIVERSITY. n.d. *Image J macros* [Online]. Available: <https://earth.unibas.ch/micro/> [Accessed 01.05.2017].
- BRANDON, D., KAPLAN, W. D. & BRANDON, D. G. 2008. *Microstructural Characterization of Materials*, Hoboken, Wiley.
- BRETON, N. & THOMPSON, A. 1988. Fluid-absent (dehydration) melting of biotite in metapelites in the early stages of crustal anatexis. *Contributions to Mineralogy and Petrology*, 99, 226-237.
- DALEN, G. V. & KOSTER, M. 2012. 2D & 3D particle size analysis of micro-CT images.
- DALLAIN, SCHULMANN & LEDRU 1999. Textural evolution in the transition from subsolidus annealing to melting process, Velay Dome, French Massif Central. *Journal of Metamorphic Geology*, 17, 61-74.
- DE GRAEF, M. 2003. *Introduction to conventional transmission electron microscopy*, Cambridge, Cambridge University Press.
- DEHM, G., HOWE, J. M. & ZWECK, J. 2012. *In-situ Electron Microscopy : Applications in Physics, Chemistry and Materials Science*, Hoboken, Wiley.
- DEVORE, G. W. 1959. Role of Minimum Interfacial Free Energy in Determining the Macroscopic Features of Mineral Assemblages. I. the Model. *The Journal of Geology*, 67, 211-227.
- FLINN, D. 1969. Grain contacts in crystalline rocks. *LITHOS*, 2, 361-370.
- FRANKE, W. 2000. The mid-European segment of the Variscides: Tectonostratigraphic units, terrane boundaries and plate tectonic evolution. *Geological Society Special Publication*, 179, 35-56.
- GARDIEN, V., THOMPSON, A. B., GRUJIC, D. & ULMER, P. 1995. Experimental melting of biotite + plagioclase + quartz \pm muscovite assemblages and implications for crustal melting. *Journal of Geophysical Research: Solid Earth*, 100, 15581-15591.
- GREEN, H. W., II 1967. Quartz; extreme preferred orientation produced by annealing. *Science*, 157, 1444-1446.
- HAIFLER, J. & KOTKOVÁ, J. 2016. UHP–UHT peak conditions and near-adiabatic exhumation path of diamond-bearing garnet–clinopyroxene rocks from the Eger Crystalline Complex, North Bohemian Massif. *LITHOS*, 248-251, 366-381.
- HASALOVÁ, P., SCHULMANN, K., LEXA, O., ŠTÍPSKÁ, P., HROUDA, F., ULRICH, S., HALODA, J. & TÝCOVÁ, P. 2008. Origin of migmatites by deformation-enhanced melt infiltration of orthogneiss: a new model based on quantitative microstructural analysis. *Journal of Metamorphic Geology*, 26, 29-53.
- HEILBRONNER, R. & BRUHN, D. 1998. The influence of three-dimensional grain size distributions on the rheology of polyphase rocks. *Journal of Structural Geology*, 20, 695-705.
- HEILBRONNER, R. & TULLIS, J. 2002. The effect of static annealing on microstructures and crystallographic preferred orientations of quartzites experimentally deformed in axial compression and shear. *Geological Society Special Publication*, 200, 191-218.
- HEILBRONNER, R. E., BARRETT, S. D. & SPRINGERLINK 2010. *Image Analysis in Earth Sciences*, Dordrecht, Springer.
- HIBBARD, M. J. 1979. Myrmekite as a marker between preaqueous and postaqueous phase saturation in granitic systems. *Bulletin of the Geological Society of America*, 90, 1047-1062.
- HIGGINS, M. D. 2006. *Quantitative textural measurements in igneous and metamorphic petrology*, Cambridge, Cambridge University Press.

- JIANG, Z., PRIOR, D. J. & WHEELER, J. 2000. Albite crystallographic preferred orientation and grain misorientation distribution in a low-grade mylonite: implications for granular flow. *Journal of Structural Geology*, 22, 1663-1674.
- KIM, C.-S. & ROHRER, G. 2004. Geometric and Crystallographic Characterization of WC Surfaces and Grain Boundaries in WC-Co Composites. *Interface Science*, 12, 19-27.
- KONOPÁSEK, J., PILÁTOVÁ, E., KOŠLER, J. & SLÁMA, J. 2014. Zircon (re)crystallization during short-lived, high- P granulite facies metamorphism (Eger Complex, NW Bohemian Massif. *Journal of Metamorphic Geology*, 32, 885-902.
- KONOPASEK, J. & SCHULMANN, K. 2005. Contrasting Early Carboniferous field geotherms: evidence for accretion of a thickened orogenic root and subducted Saxothuringian crust (Central European Variscides). *J. Geol. Soc.*, 162, 463-470.
- KOTKOVÁ, J. 1992. *Granulites and associated peridotites of North Bohemia*. MS, PhD thesis.
- KOTKOVÁ, J. 1993. Tectonometamorphic history of lower crust in the Bohemian Massif-examples of north Bohemian granulites. *Spec. Pap. Czech Geol. Surv*, 2, 1-42.
- KOTKOVÁ, J., KRÖNER, A., TODT, W. & FIALA, J. 1996. Zircon dating of North Bohemian granulites, Czech Republic: further evidence for the Lower Carboniferous high-pressure event in the Bohemian Massif. *Geologische Rundschau*, 85, 154-161.
- KOTKOVA, J., O'BRIEN, P. J. & ZIEMANN, M. A. 2011. Diamond and coesite discovered in saxony-type granulite; solution to the Variscan garnet peridotite enigma. *Geology (Boulder)*, 39, 667-670.
- KRETZ, R. 1969. On the spatial distribution of crystals in rocks. *LITHOS*, 2, 39-65.
- KRETZ, R. 1994. *Metamorphic crystallization*, Chichester, Wiley.
- KRONER, U. H., T.; ROMER, ROLF R. ; LINNEMANN, ULF 2007. The Variscan orogeny in the Saxo-Thuringian zone—Heterogenous overprint of Cadomian/Paleozoic Peri-Gondwana crust. *Geological Society of America*, Special Paper 153-172.
- KRUHL, J. H. & PETERNELL, M. 2002. The equilibration of high-angle grain boundaries in dynamically recrystallized quartz: the effect of crystallography and temperature. *Journal of Structural Geology*, 24, 1125-1137.
- KRUSE, R. & STÜNITZ, H. 1999. Deformation mechanisms and phase distribution in mafic high-temperature mylonites from the Jotun Nappe, southern Norway. *Tectonophysics*, 303, 223-249.
- LEE, A. L., WALKER, A. M., LLOYD, G. E. & TORVELA, T. 2017. Modeling the impact of melt on seismic properties during mountain building. *Geochemistry, Geophysics, Geosystems*, 18, 1090-1110.
- LEXA, O. n.d. *PolyLX Toolbox* [Online]. Available: <http://petrol.natur.cuni.cz/~ondro/polylx/home> [Accessed 01.05.2017].
- LEXA, O., ŠTÍPSKÁ, P., SCHULMANN, K., BARATOUX, L. & KRÖNER, A. 2005. Contrasting textural record of two distinct metamorphic events of similar P – T conditions and different durations. *Journal of Metamorphic Geology*, 23, 649-666.
- LINNEMANN, U., GEHMLICH, M., TICHOMIROVA, M., BUSCHMANN, B., NASDALA, L., JONAS, P., LÜTZNER, H. & BOMBACH, K. 2000. From Cadomian subduction to Early Palaeozoic rifting: The evolution of Saxo-Thuringia at the margin of Gondwana in the light of single zircon geochronology and basin development (Central European Variscides, Germany). *Geological Society Special Publication*, 179, 131-153.
- LINNEMANN, U., MCNAUGHTON, N., ROMER, R., GEHMLICH, M., DROST, K. & TONK, C. 2004. West African provenance for Saxo-Thuringia (Bohemian Massif): Did Armorica ever leave pre-Pangean Gondwana? – U/Pb-SHRIMP zircon evidence and the Nd-isotopic record. *International Journal of Earth Sciences*, 93, 683-705.
- MARASSI & NOBILI, R. F. 2009. Measurement Methods: Structural and Chemical Properties: Scanning Electron Microscopy.
- MATTE, P., MALUSKI, H., RAJLICH, P. & FRANKE, W. 1990. Terrane boundaries in the Bohemian Massif: Result of large-scale Variscan shearing. *Tectonophysics*, 177, 151-170.

- MCLELLAN, E. L. 1983. Contrasting textures in metamorphic and anatectic migmatites. *Journal of Metamorphic Geology*, 1, 241-264.
- MINGRAM, B. 1998. The Erzgebirge, Germany, a subducted part of northern Gondwana: geochemical evidence for repetition of early Palaeozoic metasedimentary sequences in metamorphic thrust units. *Geol. Mag.*, 135, 785-801.
- MINGRAM, B., KRÖNER, A., HEGNER, E. & KRENTZ, O. 2004. Zircon ages, geochemistry, and Nd isotopic systematics of pre-Variscan orthogneisses from the Erzgebirge, Saxony (Germany), and geodynamic interpretation. *International Journal of Earth Sciences*, 93, 706-727.
- MLČOCH, B. & KONOPÁSEK, J. 2010. Pre-Late Carboniferous geology along the contact of the Saxothuringian and Teplá-Barrandian zones in the area covered by younger sediments and volcanics (western Bohemian Massif, Czech Republic). *Journal of Geosciences*, 55.
- NANCE, R. D. & MURPHY, J. B. 1994. Contrasting basement isotopic signatures and the palinspastic restoration of peripheral orogens: example from the Neoproterozoic Avalonian-Cadomian belt. *Geology*, 22, 617-620.
- O'BRIEN, P. & CARSWELL, D. 1993. Tectonometamorphic evolution of the Bohemian Massif: evidence from high pressure metamorphic rocks. *Geologische Rundschau*, 82, 531-555.
- OTANI, M. & WALLIS, S. 2006. Quartz lattice preferred orientation patterns and static recrystallization; natural examples from the Ryoke Belt, Japan. *Geology (Boulder)*, 34, 561-564.
- OXFORD INSTRUMENTS PLC. 2015. *EBS D Explained: From data acquisition to advanced analysis* [Online]. Online: Oxford Instruments plc,. Available: <https://www.oxford-instruments.com/products/microanalysis/ebsd> [Accessed].
- OXFORD INSTRUMENTS PLC. 2016-2017. *EBS D Sample preparation* [Online]. Online: Oxford Instruments Plc. Available: <http://www.ebsd.com/14-hints-tips-for-ebsd-data-collection/ebsd-sample-preparation> [Accessed 07.03.2017].
- PASSCHIER, C. W., TROUW, R. A. J. & SPRINGERLINK 2005. *Microtectonics*, Springer Berlin Heidelberg.
- PERCHUK, A. 2008. Melt inclusions in garnet from diamondiferous gneiss, Erzgebirge, Germany. *Doklady Earth Sciences*, 421, 832-834.
- RAMBERG, H. 1962. Intergranular precipitation of albite formed by unmixing of alkali feldspar. *Neues Jahrbuch für Mineralogie/Journal of Mineralogy and Geochemistry*, 98, 14-34.
- ROETZLER, K., SCHUMACHER, R., MARESCH, W. V. & WILLNER, A. P. 1998. Characterization and geodynamic implications of contrasting metamorphic evolution in juxtaposed high-pressure units of the western Erzgebirge (Saxony, Germany). *European Journal of Mineralogy*, 10, 261-280.
- SAWYER, E. W. 2001. Melt segregation in the continental crust: distribution and movement of melt in anatectic rocks. *Journal of Metamorphic Geology*, 19, 291-309.
- SAWYER, E. W., BROWN, M. G. & KOTKOVA, J. 1999. Criteria for the recognition of partial melting. *Physics and Chemistry of the Earth. Part A: Solid Earth and Geodesy*, 24, 269-279.
- SCHULMANN, K., KONOPÁSEK, J., JANOŠEK, V., LEXA, O., LARDEAUX, J.-M., EDEL, J.-B., ŠTÍPSKÁ, P. & ULRICH, S. 2009. An Andean type Palaeozoic convergence in the Bohemian Massif. *Comptes rendus - Géoscience*, 341, 266-286.
- SCHULMANN, K., LEXA, O., JANOŠEK, V., LARDEAUX, J. M. & EDEL, J. B. 2014. Anatomy of a diffuse cryptic suture zone: an example from the bohemian massif, European Variscides.(Report)(Author abstract). *Geology*, 42, 275.
- SCHULMANN, K., MLČOCH, B. & MELKA, R. 1996. High-temperature microstructures and rheology of deformed granite, Erzgebirge, Bohemian Massif. *Journal of Structural Geology*, 18, 719-733.
- SCHWARZER, R. A., FIELD, D. P., ADAMS, B. L., KUMAR, M. & SCHWARTZ, A. J. 2009. *Present state of electron backscatter diffraction and prospective developments*.
- SIMPSON, C. & WINTSCH, R. P. 1989. Evidence for deformation-induced K-feldspar replacement by myrmekite. *Journal of Metamorphic Geology*, 7, 261-275.

- ŠTEMPROK, M. & BLECHA, V. 2015. Variscan Sn–W–Mo metallogeny in the gravity picture of the Krušné hory/Erzgebirge granite batholith (Central Europe). *Ore Geology Reviews*, 69, 285-300.
- UNDERWOOD, E. E. 1970. *Quantitative stereology*, Reading, Mass, Addison-Wesley.
- VERNON, R. H. 1991. Questions about myrmekite in deformed rocks. *Journal of Structural Geology*, 13, 979-985.
- VERNON, R. H. 2004. *A practical guide to rock microstructure*, Cambridge, Cambridge University Press.
- VIELZEUF, D. & HOLLOWAY, J. 1988. Experimental determination of the fluid-absent melting relations in the pelitic system. *Contributions to Mineralogy and Petrology*, 98, 257-276.
- ZÁVADA, P., SCHULMANN, K., KONOPÁSEK, J., ULRICH, S. & LEXA, O. 2007. Extreme ductility of feldspar aggregates—Melt-enhanced grain boundary sliding and creep failure: Rheological implications for felsic lower crust. *Journal of Geophysical Research: Solid Earth*, 112, n/a-n/a.
- ZULAUF, G., DÖRR, W., FIALA, J., KOTKOVÁ, J., MALUSKI, H. & VALVERDE-VAQUERO, P. 2002. Evidence for high-temperature diffusional creep preserved by rapid cooling of lower crust (North Bohemian shear zone, Czech Republic). *Terra Nova*, 14, 343-354.

Appendix A




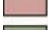


Digitized grain maps

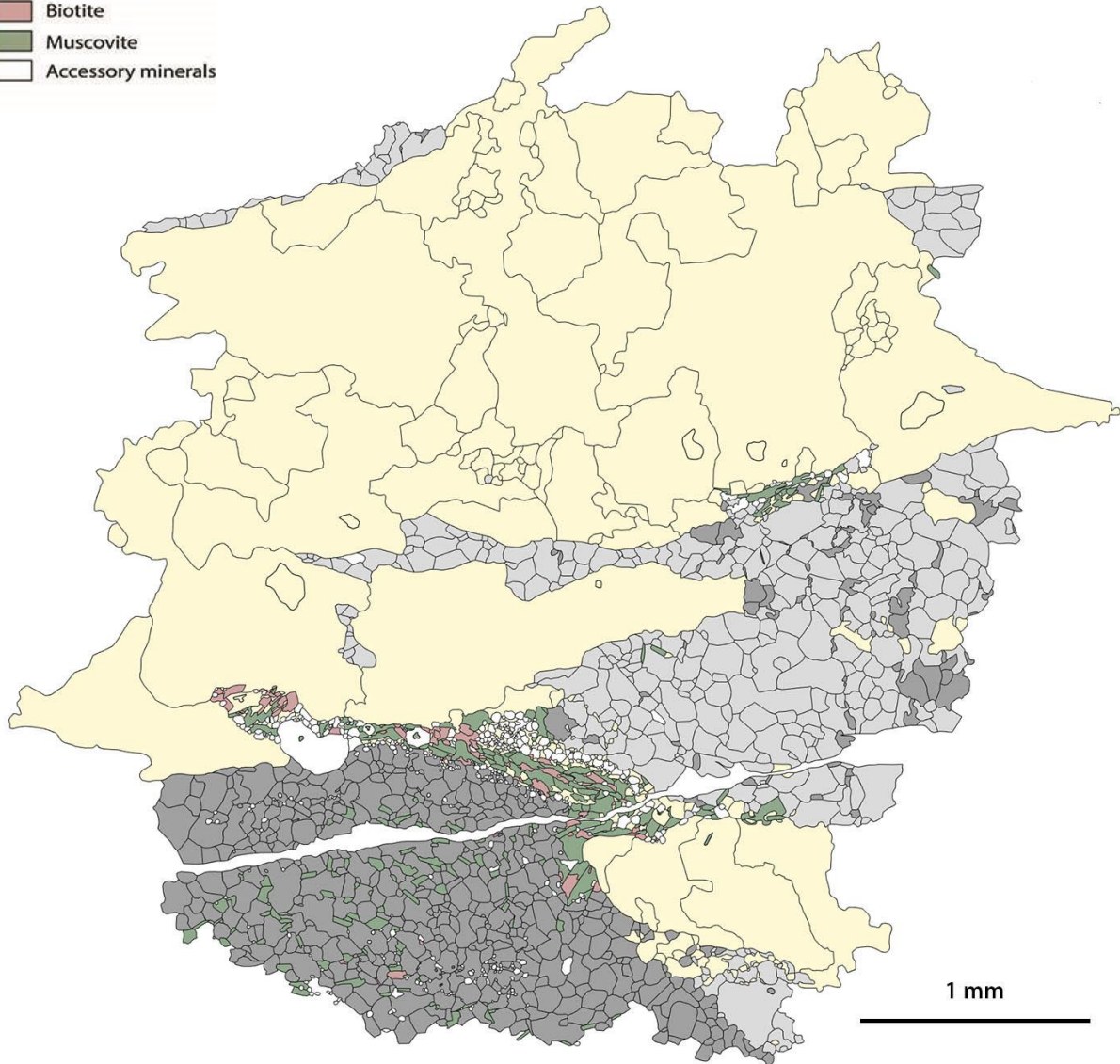
In this appendix, digitized grain maps introduced in the main text of the thesis are presented in full size, allowing closer examination of their microstructure. The grain maps are presented in successive order starting with the anisotropic orthogneiss (type I), followed by migmatitic orthogneiss (type II) and granofels (type III) and lastly the granulite (type IV) grain map is presented. When comparing the individual grain maps, one should note that there is a difference in scale (see individual scale bars)

Appendix A: Digitized grain maps

Orthogneiss (Sample KL22-A(B4))

Legend



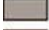

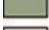


-  Quartz
-  K-feldspar
-  Plagioclase
-  Biotite
-  Muscovite
-  Accessory minerals

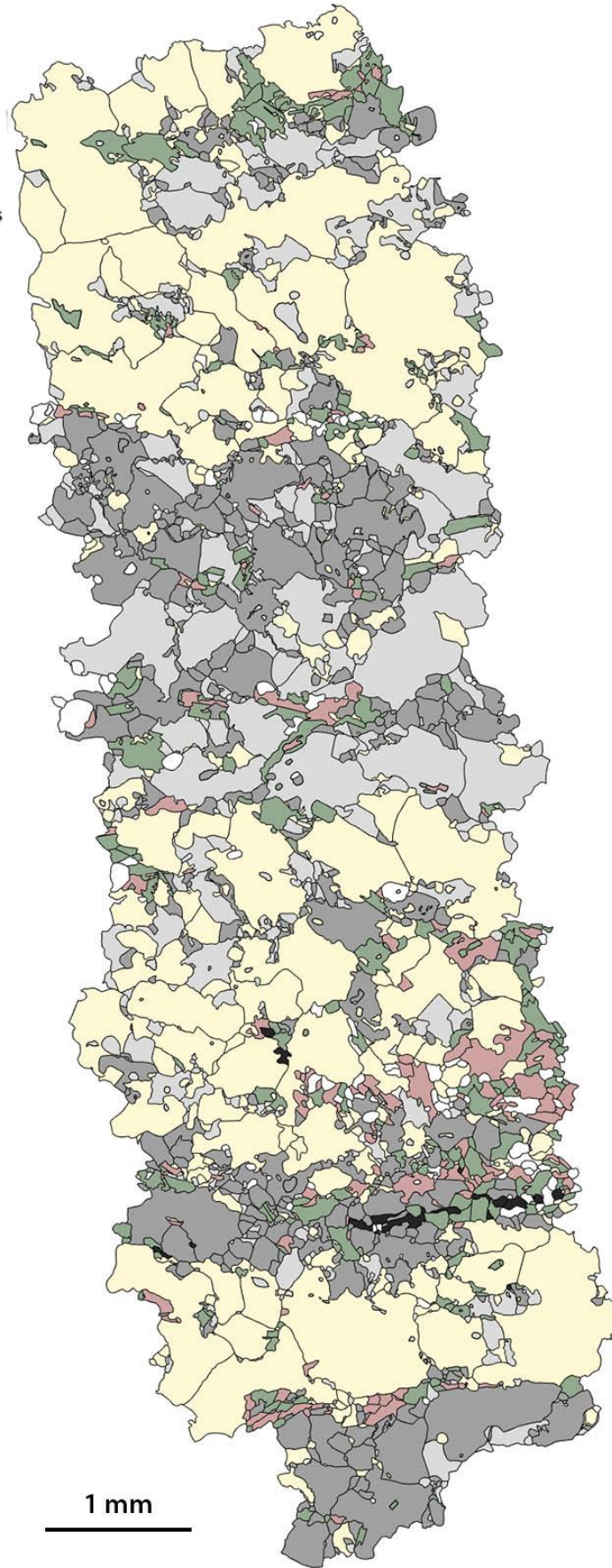


Appendix A: Digitized grain maps

Migmatitic orthogneiss (EZ 22P)

Legend

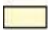



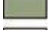

-  Quartz
-  K-feldspar
-  Plagioclase
-  Biotite
-  Muscovite
-  Accessory minerals
-  Holes

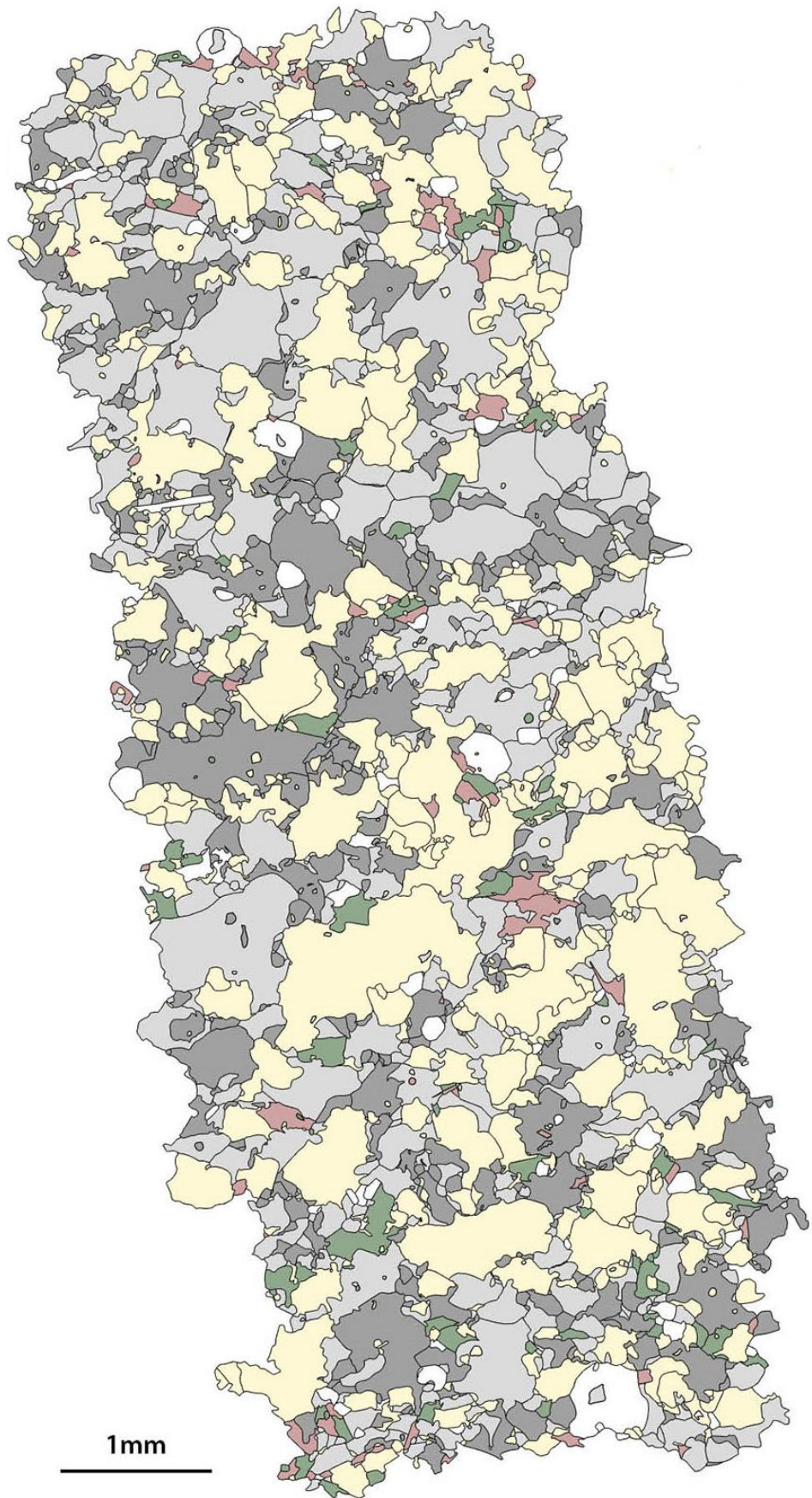


Appendix A: Digitized grain maps

Granofels (Sample EZ 22R)

Legend

-  Quartz
-  K-feldspar
-  Plagioclase
-  Biotite
-  Muscovite
-  Accessory minerals

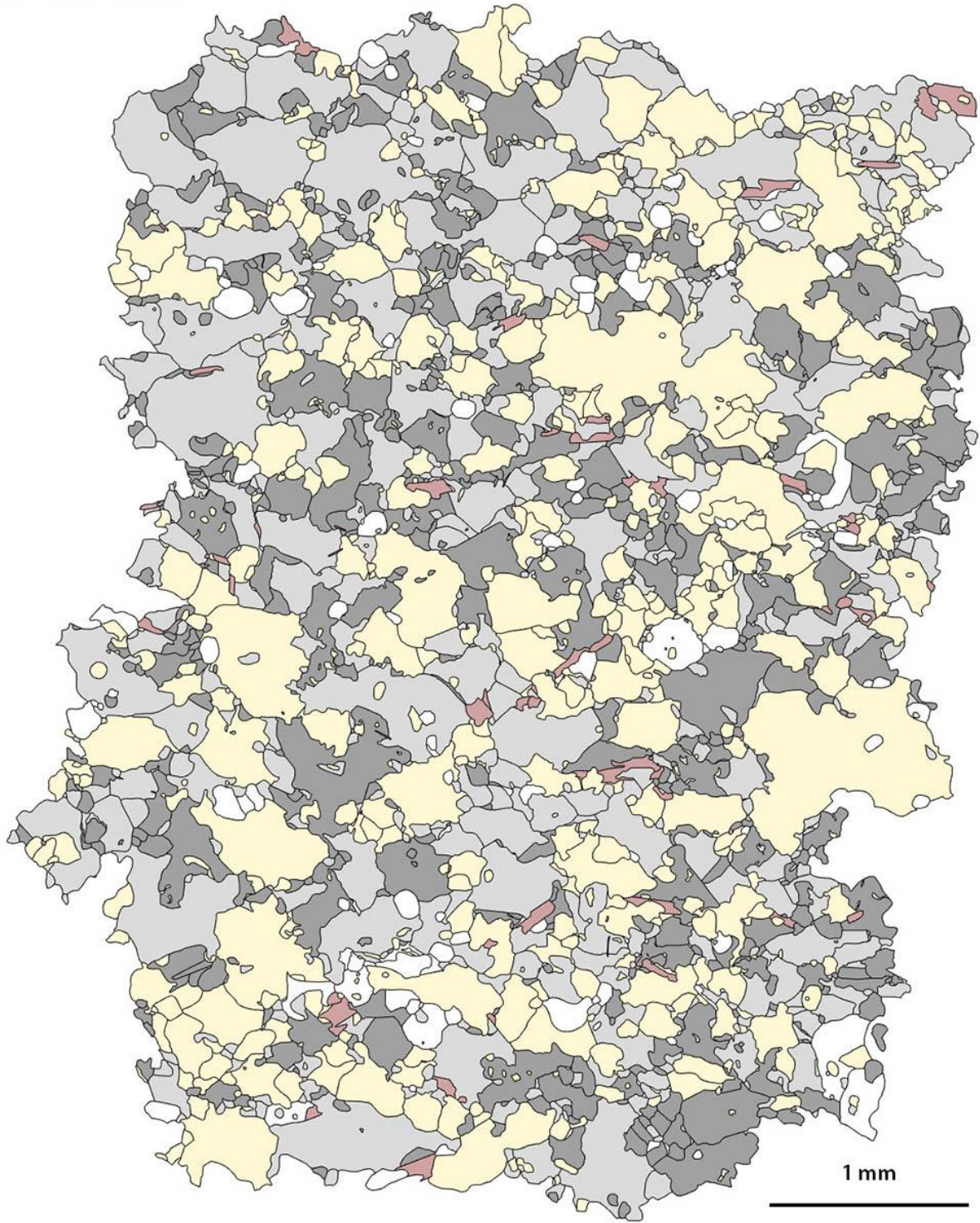


Appendix A: Digitized grain maps

Granulite (sample EZ 22S)

Legend

-  Quartz
-  K-feldspar
-  Plagioclase
-  Biotite
-  Accessory minerals



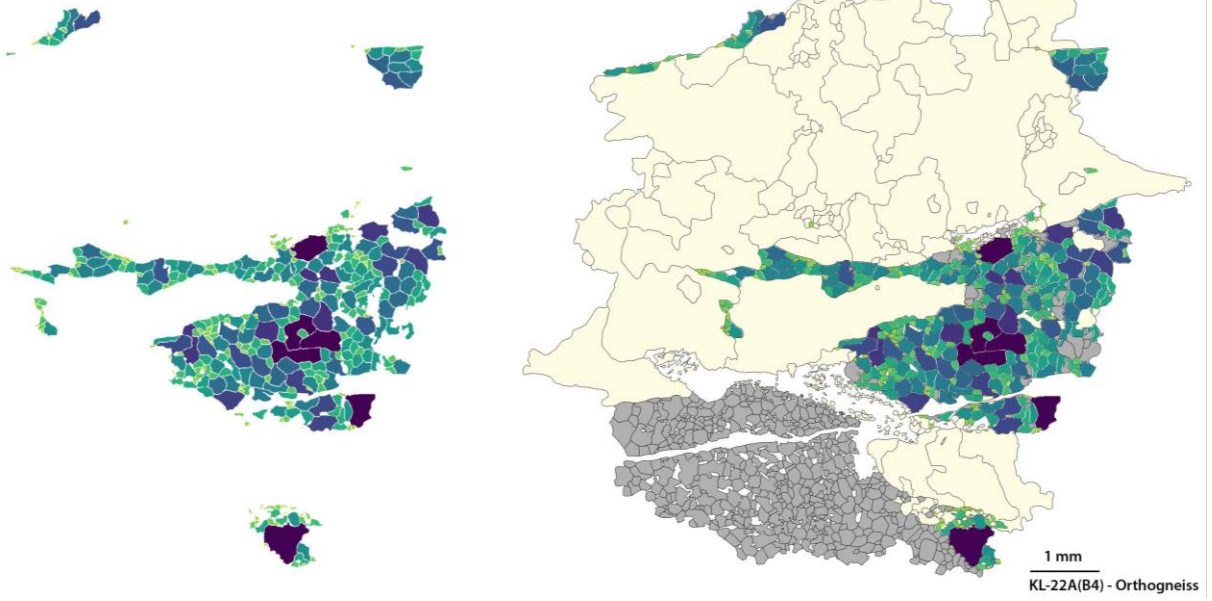
Appendix B

Grain size mapping

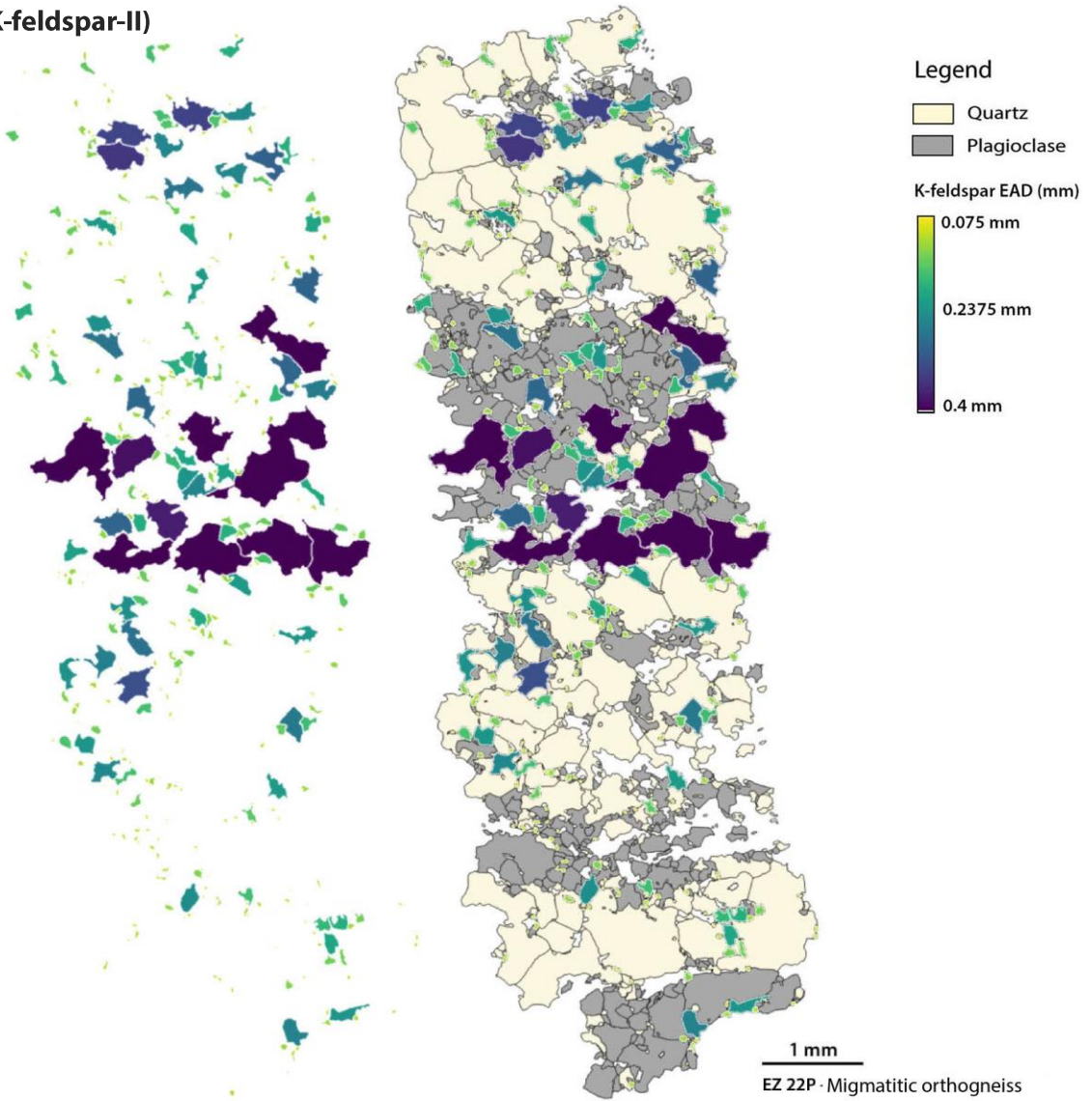
In this appendix, results of grain size maps of K-feldspar and plagioclase, which has not been published within the text of the thesis are presented for each of the investigated samples. The size mapping involves colour coding of grains according to certain grain size parameters, in this case the mapping has been done according to equal area diameter of grains. This allows for direct comparison with the previously presented box plot (Figure 3.2-2). The colour coding process considers inclusions as being part of the host grain, which might have led to a slight overestimation of EAD of certain grains. The colour coding only reflects the cross-sectional size of grains, so it is likely that some of the smaller grains are sections of a larger grains, still it provides a visual insight into the distribution of grain sizes within the samples. The grain size maps are presented phase by phase starting with K-feldspar size maps for all samples in successive order from type I to type IV, followed by grain size maps for plagioclase. The grain size maps are presented in two ways, firstly as a standalone size map (left) and secondly as the grain size map overlaid onto grain maps (right) showing the relative distribution of grain sizes within the other complementary felsic phases. When looking at the size maps one should note that the physical scale is different for each of the samples. Also, for each phase, the thresholds for the colour coding are equal which allows for direct visual comparison, note however that the colour coding changes from phase to phase. Keep in mind that all grains falling below the minimum threshold (0.0075 mm in the case of K-feldspar) and above the maximum threshold (0.4 mm in the case of K-feldspar) are evaluated as a part of the minimum grain size fraction and maximum grain size fraction, respectively.

Appendix B: Grain size maps

K-feldspar-I)



K-feldspar-II)



Legend

Quartz

Plagioclase

K-feldspar EAD (mm)

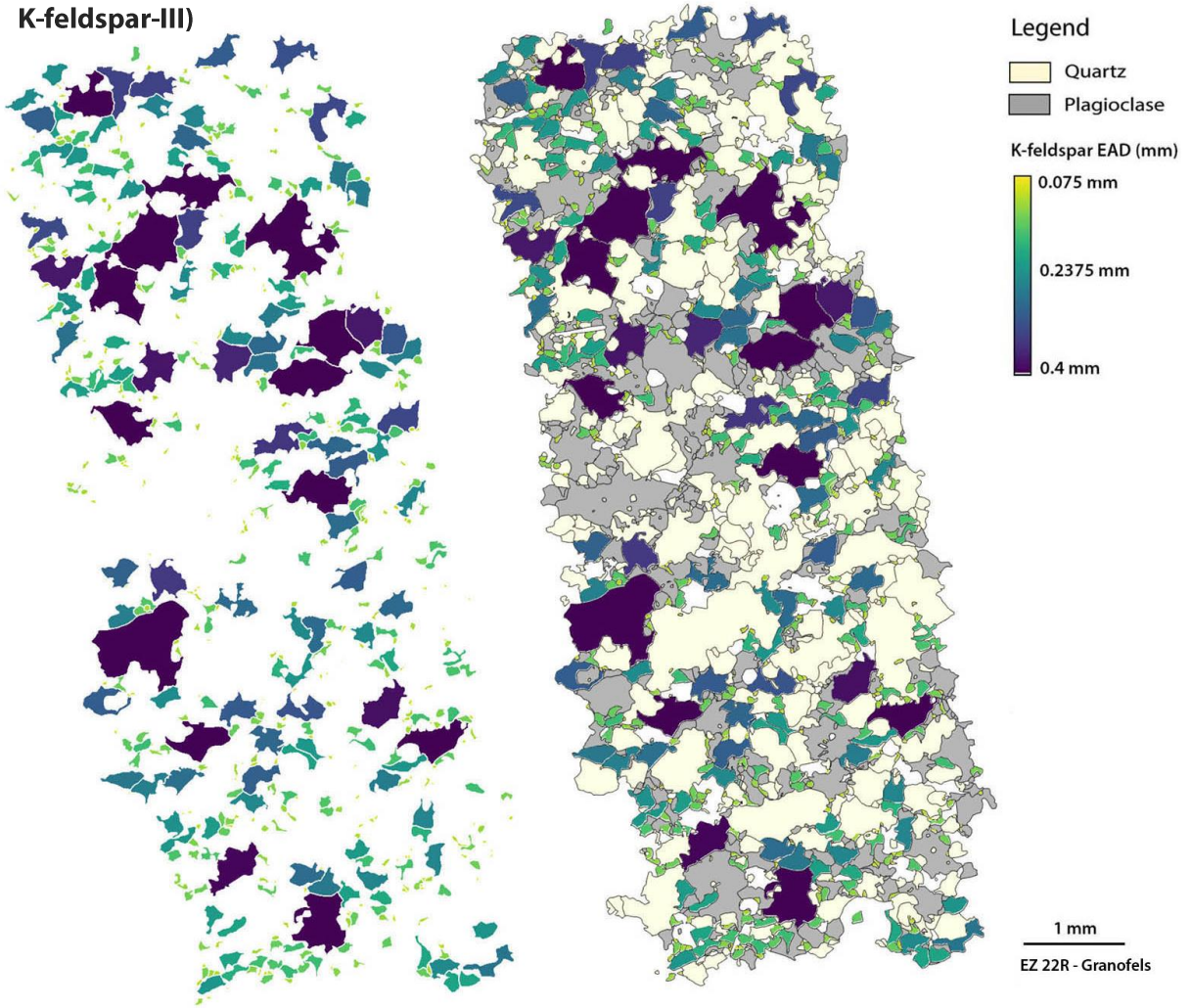
0.075 mm

0.2375 mm

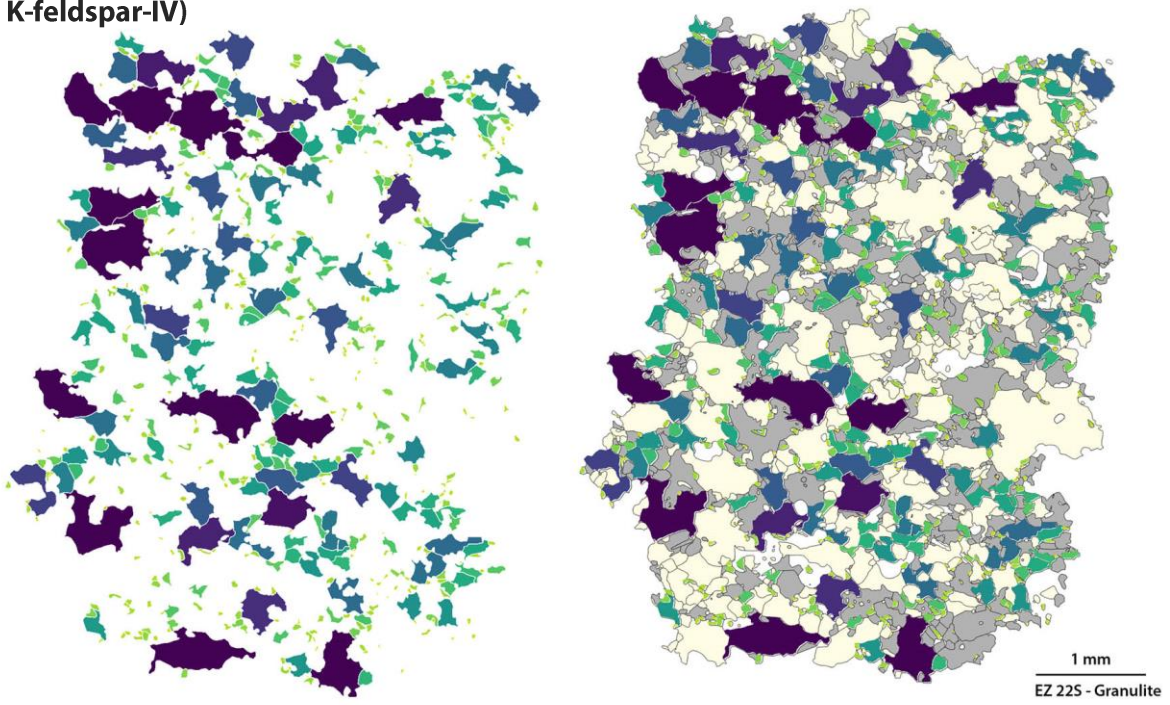
0.4 mm

Appendix B: Grain size maps

K-feldspar-III)

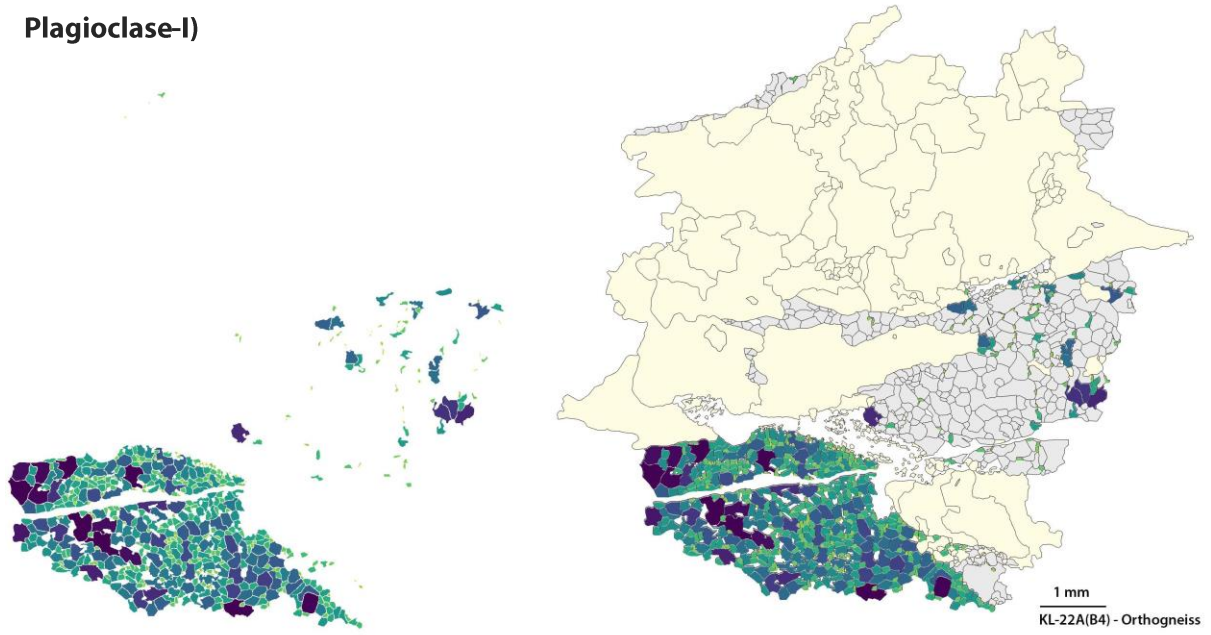


K-feldspar-IV)

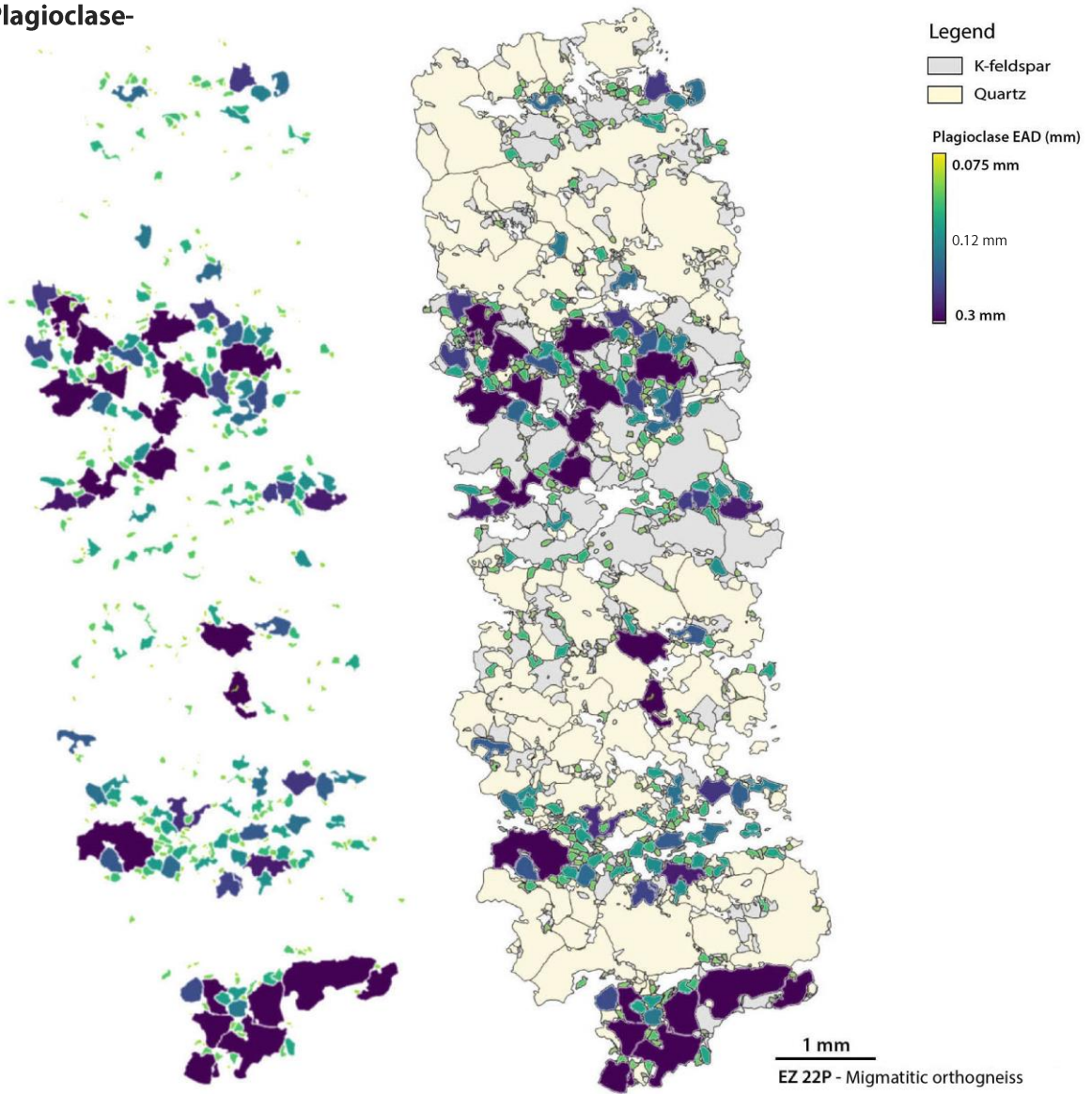


Appendix B: Grain size maps

Plagioclase-I)

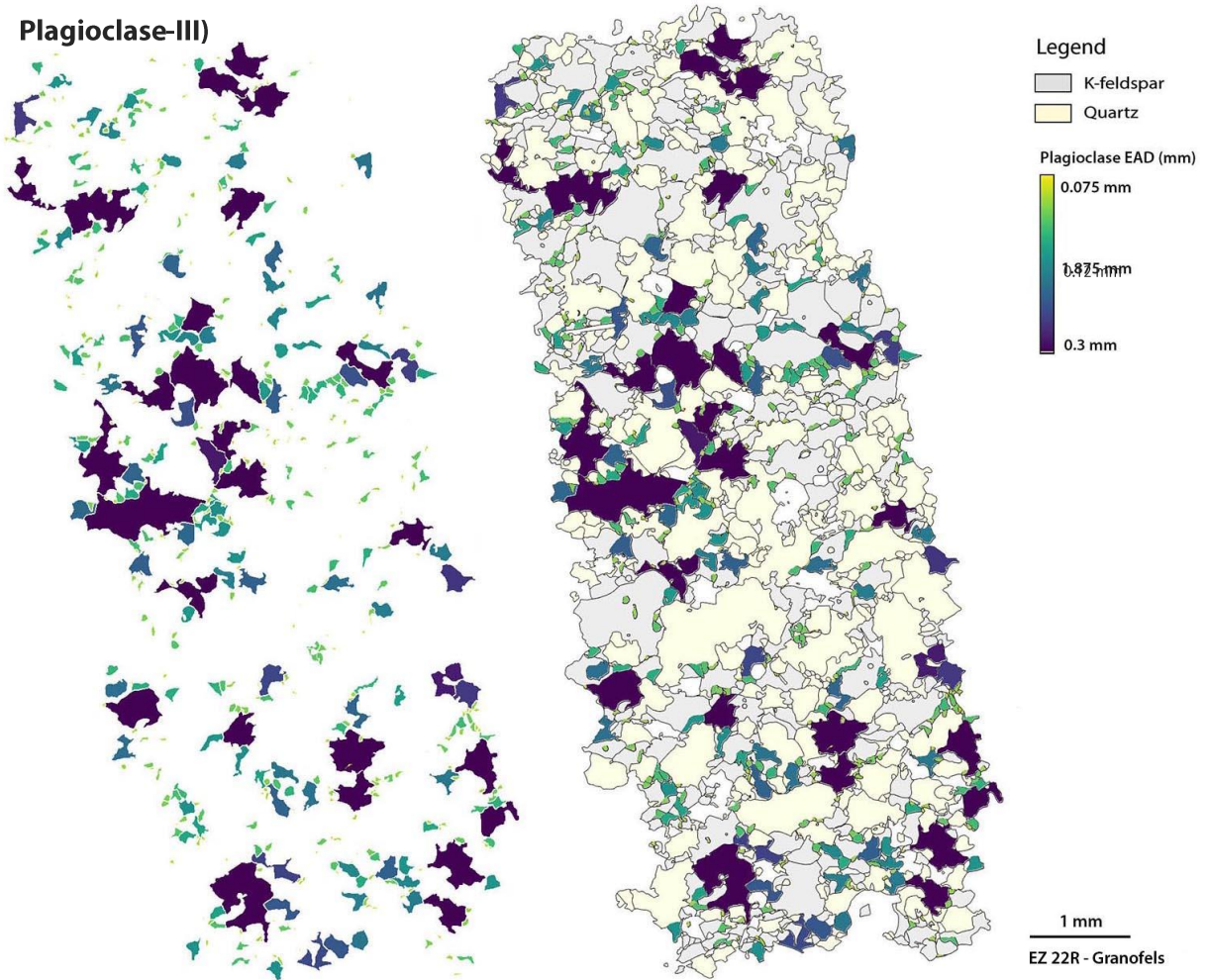


Plagioclase-



Appendix B: Grain size maps

Plagioclase-III)



Plagioclase-IV)

